UNIVERSITÀ
DEGLI STUDI
FIRENZE

International Doctorate in Atomic and Molecular Photonics

CICLO XXX

COORDINATORE Prof. Roberto Righini

High-Q microcavities: characterization and optomechanical applications

Settore Scientifico Disciplinare FIS/03

Dottorando	**Tutore**
Dott. Dmitry Nuzhdin	Prof. Diederik S. Wiersma

Coordinatore	**Cotutore**
Prof. Roberto Righini	Prof. Heinz Kalt

Anni 2014/2017

High-Q microcavities: characterization and optomechanical applications

2017, Dmitry Nuzhdin

International Doctorate in Atomic and Molecular Photonics, October 2017

Coordinator: Prof. Roberto Righini

Supervisors: Prof. Dr. Diederik S. Wiersma and Prof. Dr. Heinz Kalt

Reviewers: Associate Professor Arri Priimägi and Assistant Professor Piotr Wasylczyk

Università degli Studi di Firenze

group of Optics of Complex Systems

Laboratorio Europeo di Spectroscopia non Lineare (LENS)

via Nello Carrara 1, Sesto Fiorentino

50019 - Florence, Italy

High-Q microcavities:

Characterization and optomechanical

applications

Zur Erlangung des akademischen Grades eines

DOKTORS DER NATURWISSENSCHAFTEN

von der Fakultät für Physik

des Karlsruher Instituts für Technologie (KIT)

genehmigte

DISSERTATION

von

MSc. Dmitry Nuzhdin

aus Nizhny Novgorod, Russland

Tag der mündlichen Prüfung: 07.03.2018

Referent: Prof. Dr. D. S. Wiersma

Korreferent: Prof. Dr. H. Kalt

High-Q microcavities: characterization and optomechanical applications

2017, Dmitry Nuzhdin

International Doctorate in Atomic and Molecular Photonics, October 2017

Coordinator: Prof. Roberto Righini

Supervisors: Prof. Dr. Diederik S. Wiersma and Prof. Dr. Heinz Kalt

Reviewers: Associate Professor Arri Priimägi and Assistant Professor Piotr Wasylczyk

Università degli Studi di Firenze

group of Optics of Complex Systems

Laboratorio Europeo di Spectroscopia non Lineare (LENS)

via Nello Carrara 1, Sesto Fiorentino

50019 - Florence, Italy

Contents

2

Preface

Light technologies have been rapidly developing in past years leading to enormous explosion in field of photonics. Various application of light based devices were not only proposed by research groups and institutes, but also conquered a significant part of the market. Two of the most diffuse examples that entered lives of many people are fiber-optic telecommunication systems and medical diagnostic systems based on light scattering. As this work started almost together with International Year of Light we made an attempt to broaden humanity's knowledge about photonic devices and their applications.

In Chapter 1 we present the relevant background information that is necessary for understanding the results further. In this chapter we shortly introduce waveguides and whispering gallery mode resonators – the main building blocks of all the integrated photonics. Then, the second part of the chapter is devoted to the two main fabrication techniques for the polymeric photonics - direct laser writing and electron beam lithography. Both techniques are used in the current work to produce various structures.

In Chapter 2 we present a novel technique for diagnostic of integrated photonic circuits. Based on optical gating principle, the technique combines capabilities of static and time-resolved measurements and allows to image light propagation in photonic structures on sub-picosecond scale. A number of system parameters can be accessed taking advantage of the presented technique. The apparatus has been built in the framework of this research and its application together with a comparison with similar techniques is shown in this chapter.

Chapter 3 shows the basics of liquid crystalline networks – class of smart materials that are responsive to light irradiation. We discuss the composition and the main characteristics of the material that bring us to the main idea behind actuation mechanism and optomechanical applications of the material.

In Chapter 4 we present a new advance in micro robotics – a microscopic hand that is remotely controlled by light. We discuss the designing and fabrication of the robotic structure and show that differences in design have advantages and disadvantages in terms of complexity of fabrication and overall performance of the structures. At last we show that the micro hand is capable of autonomous action and it can distinguish colors.

In the final Chapter 5 we merge two different worlds described in the previous chapters and try to demonstrate the principle of optomechanical control of two micro lasers on liquid crystalline network microfilm.

This work has been conducted within Erasmus Mundus Joint Doctorate program "EUROPHOTONICS" that implies collaboration between the research institutes in Europe. The most part of the research described in Chapters 1-4 carried out at European Laboratory for Non-Linear Spectroscopy (LENS) – University of Florence (Florence, Italy). However, the electron beam lithography was performed at Institute of Microstructure Technology – Karlsruhe Institute of Technology (Eggenstein-Leopoldshafen, Germany). Research about the optomechanical control of micro laser coupling was completely (including the fabrication of the samples) conducted at Institute of Applied Physics - Karlsruhe Institute of Technology (Karlsruhe, Germany).

The research was supervised by:

- Prof. Diederik Sybolt Wiersma, LENS, Università degli Studi di Firenze, Firenze, Italy
- Prof Heinz Kalt, APH, Karlsruher Institut für Technologie, Karlsruhe, Germany

1 Integrated photonic components: description, fabrication techniques

Fundamental equations from which classical description of light can be retrieved in different media are Maxwell equations - a set of equations fully describing system of charges and currents. Here we report them in the most general form:

$$\nabla \times \boldsymbol{E} + \frac{\partial \boldsymbol{B}}{\partial t} = 0, \tag{1}$$

$$\nabla \times \boldsymbol{H} - \frac{\partial \boldsymbol{D}}{\partial t} = \boldsymbol{J}, \tag{2}$$

$$\nabla \cdot \boldsymbol{D} = \rho, \tag{3}$$

$$\nabla \cdot \boldsymbol{B} = 0, \tag{4}$$

where $\boldsymbol{E}$ is electric field vector, $\boldsymbol{H}$ is magnetic field vector, $\boldsymbol{D}$ - electric displacement vector and $\boldsymbol{B}$ - magnetic induction vector; ρ and $\boldsymbol{J}$ are electric charge density and electric current density vector, respectively.

An exhaustive demonstration of field calculation in different media is beyond the scope of this work. However, we will derive solutions of Maxwell equations for waveguides and whispering gallery mode resonators describing the most important steps.

1.1 Basics of optical waveguides

The key components of integrated photonic circuits without a doubt are waveguides. Serving the same purpose as a conductor in electronics, they guide light without significant losses for relatively long distances. However, their functionality

is not restricted only by light guiding – one of the examples is a directional coupler that serves as power divider in integrated circuits.

The theory of light propagation in waveguides is fully described in numerous books and articles [1]–[3]. The complete description starts from the Maxwell equations and wave equation in a dielectric medium and the field confined inside a linear waveguide is described as a propagating mode.

Considering a system of coordinates with the z axis parallel to the waveguide axis, the characteristics of a waveguide are determined by the transverse profile of its dielectric constant $\varepsilon(x, y)$, which is independent of the longitudinal (z) direction (wave propagation axis). The dielectric waveguide permittivity can be therefore described as:

$$\varepsilon(x, y) = \varepsilon_0 n^2(x, y) \tag{5}$$

where ε_0 is vacuum permittivity. The function $n(x, y)$ is the refractive index profile of a waveguide. In case of slab waveguide the function is independent on one of the coordinates, while with rib of rectangular waveguides the function fully describes the material composition of the structure.

A waveguide mode described by electric and magnetic field has a form of the following equations:

$$E(x, y, z, t) = E_m(x, y)\, exp(-i\beta_m z - \omega t), \tag{6}$$

$$H(x, y, z, t) = H_m(x, y)\, exp(-i\beta_m z - \omega t), \tag{7}$$

where β_m is a propagation constant of a mode with number m, ω – angular frequency, $E_m(x, y)$ and $H_m(x, y)$ describe the transverse profile of a mode.

Inserting (6) and (7) into Maxwell equations it is possible to obtain a complete system that can be solved for each vectoral field component, as discussed in detail

6

in [3]. The resulting solutions for dielectric waveguides, are guided modes (bound states), where the energy is confined near the axis, and radiation modes (unbound states) with their energy leaking to the medium surrounding the guide.

The guided modes are characterized by a set of discrete values of propagation constants β_m, while the radiation modes belong to a continuum. The discrete solutions correspond to the fundamental mode ($m=0$) and to the higher modes ($m=1, 2...$). In waveguides a cut-off frequency exists and defines the frequency, but which guided modes cannot exist. The cutoff frequency is defined by the refractive index and geometrical dimensions of a waveguide. Other relevant solutions are represented by the evanescent modes, defined by a complex propagation constant $\beta_m=-i\alpha_m$ that decays as $exp(-\alpha_m z)$.

The exact analytical solution is derived for planar waveguide[4], but no analytic solution is available for ridge or strip waveguides. However, it has been shown that approximated solutions can be retrieved applying specific simplifications [1], [2]. Except for those few exhibiting special geometric structures, such as circular optical fibers, non-planar dielectric waveguides generally do not have analytical solutions for their guided mode characteristics. In these cases numerical methods, such as the beam propagation method[5], are typically used for analyzing and designing such waveguides. In this work, we use a finite element method based software to design the photonic structures, and calculate the electric field distribution inside the dielectric structures.

One more important parameter describing propagation of light in dielectric waveguides is the effective refractive index n_{eff}, which is defined through the propagation constant of the mode and wavenumber in free space k_0.

$$n_{eff} = \frac{\beta_m}{k_0} \tag{8}$$

In current work we will work only with polymeric waveguides, that are fabricated by one of the two most common lithographic methods: direct laser writing or electron beam lithography. Polymeric waveguide's advantages are easiness of fabrication and integration (comparing with optical fibers) together with possibility to modify the physical properties of the materials chemically. However, most of the polymers suffer from low refractive index values that defines low refractive index contrast and therefore a low mode confinement.

1.2 Basics of whispering gallery mode (WGM) resonators

Whispering gallery resonance was first discovered by Lord Rayleigh in 1878 in St. Paul's Cathedral in London. He noticed that acoustic waves can travel near wall of the dome so whisper from one side of the cathedral could be clearly heard near the opposite side [6]. Some years later, it had been discovered that the same phenomenon can occur with light waves. This phenomenon can be described as a light wave travelling and being reflected at grazing incidence along a circular border of two media, and after a roundtrip constructively interferes with itself.

In modern light technology WGM resonators play a key role, serving numerous purposes such as optical filters[7]–[9], biosensors [10], [11], applications in cavity quantum electrodynamics[12], [13], optomechanics[14], [15], topological physics [16]. In case when WGM resonator is doped with an active medium it turns into a WGM laser [17].

Whispering gallery mode resonances occur when a path of propagating wave is equal to several wavelengths in media:

$$2\pi R n_{eff} = \lambda\, m,$$ (9)

where R is radius of curvature of an element (ring, disk, bottle, etc.).

The spatial and temporal confinement of WGM depend on the geometry, the cavity material, surrounding material and roughness of the dielectric structure. The most important value that describes any cavity/resonator is its *quality factor Q* – the value that describes the ability of a cavity to store energy inside.

$$Q = \omega_0 \frac{E_{stored}}{P_{diss}} = \tau\omega_0, \tag{10}$$

where ω_0 -angular frequency of a resonance, E_{stored} – energy stored in a cavity, P_{diss} - power dissipation, τ – a time-constant, describing energy decay rate.

Based on different mechanisms of energy dissipation, several contributions to overall quality factor is differentiated. The three main intrinsic loss mechanisms are absorption (Q_{abs}), radiation (Q_{rad}) and surface scattering (Q_{scatt}). Extrinsic loss (EM energy leaking into a bus waveguide or a fiber) is accounted as Q_{ext}. In this case the overall quality factor is calculated as

$$\frac{1}{Q} = \frac{1}{Q_{abs}} + \frac{1}{Q_{rad}} + \frac{1}{Q_{scatt}} + \frac{1}{Q_{ext}} \tag{11}$$

The polymers used in this work have negligible absorption for near-infrared part of spectrum therefore allowing us to omit Q_{abs} from the consideration. The radiation losses in case of WGM resonator disks and rings are defined by the radius of curvature and, in case of considered wavelengths and structure sizes considered in the present work it can also be safely disregarded. Therefore, two main mechanisms remain. While Q_{ext} is ruled by the coupling (i.e. gap) between the resonator and bus waveguide, the surface roughness depends on the fabrication method, material and can be reduced, for instance, by thermal treatment.

Another important characteristic of the cavity is the *free spectral range* (FSR) being the spectral distance between two resonances. FSR is derived from (9) and is equal:

$$FSR = \frac{{\lambda_0}^2}{2\pi R n_{eff} + \lambda_0} \tag{12}$$

The simplest configuration to exploit and investigate the WGM resonator properties is a unidirectional coupling through a fiber or a waveguide. In both cases, the output is affected by the cavity properties and we can retrieve the spectral dependence starting from (10). From this equation, we can reconstruct the time dependence

$$U(t) = U_0 \, exp\left(-\frac{\omega_0 t}{Q}\right) \tag{13}$$

This equation shows that the cavity Q-factor can be directly determined by measuring the temporal decay of the energy U in so-called cavity-ringdown measurements. An alternative and more practical way to determine the Q-factor is the measurement of the resonance linewidth in the frequency domain. This approach is derived and discussed in the following. Due to the relation $U(t)=E^2(t)$, the time dependency of the electric field E is given by

$$E(t) = e_0 \, exp\left(-\frac{\omega_0 t}{2Q}\right) exp(-i\omega_0 t) \tag{14}$$

Fourier transform of equation (14) results in the Lorentzian-shaped intensity *I* distribution of the resonance

$$I(\omega) \propto \frac{1}{(\omega - \omega_0)^2 + (\frac{\omega}{2Q})^2} \tag{15}$$

10

This Lorentzian lineshape has a full width at half maximum of $\delta\omega = \omega_0/Q$. Considering this, the Q-factor can be calculated trough transmission measurements as follows:

$$Q = \frac{\omega_0}{\delta\omega} \approx \frac{\lambda}{\delta\lambda} \qquad (16)$$

And in this case $\delta\lambda$ is the full width at half maximum of the peak as function and can thus be directly inferred from the linewidth of the resonance.

The interaction of the WGM resonator with bus waveguide is described by coupled mode theory and in details reported in [2], [3], [18]. However, here we will show the most important result of those calculations – the transmission spectrum dependence from the frequency of the signal.

$$T(\omega) = \frac{\left(\dfrac{1}{\tau_{ext}} - \dfrac{1}{\tau_{int}}\right)^2 + (\omega - \omega_0)^2}{\left(\dfrac{1}{\tau_{ext}} + \dfrac{1}{\tau_{int}}\right)^2 + (\omega - \omega_0)^2} \qquad (17)$$

where τ_{ext} is time constant characterizing an energy decay rate through the external mechanisms and τ_{int} is time constant characterizing an energy decay rate through the internal dissipation.

The transmission properties are commonly characterized as over-coupled, critically coupled and under-coupled. Under-coupling refers to the case where the waveguide coupling is weak and the cavity decay rate τ_{int}^{-1} exceeds the cavity coupling rate τ_{ext}^{-1}. In this case the amplitude of the cavity leakage field is much smaller than the amplitude of the transmitted waveguide field. The cavity leakage field exhibits a phase shift of $\pi > \varphi > 0$. In the over-coupled regime, instead, the rate of cavity coupling exceeds the cavity decay rate, $\tau_{ext}^{-1} > \tau_{int}^{-1}$. The amplitude of the cavity field in this case is larger than transmitted pump field, and reaches a value of

11

twice the waveguide amplitude in the case of strong over-coupling. But the most interesting case in optics is the critical coupling. Critical coupling occurs when the external lifetime is matched to the intrinsic cavity decay rate $\tau_{ext}^{-1}=\tau_{int}^{-1}$. In this case the transmission after the resonator ideally vanishes, and a complete power transfer of the optical power, carried by the wave to the cavity mode, occurs. The signal vanishes due to the interference of the cavity leakage field and transmitted pump field, which exhibit equal magnitude but a relative phase shift of π [19].

1.3 Fabrication techniques: Direct Laser Writing (DLW)

1.3.1 Two-photon absorption polymerization

First predicted in the beginning of 20-th century, the first time two-photon absorption was first demonstrated in 1961 in [20]. Two photon (or 2-photon) absorption is a third-order non-linear process when two photons of energy E_1 absorbed simultaneously, leading to a change of energy state of a system with a value $2E_1$. The absorption coefficient in this process depends on the intensity and, therefore, it occurs only at sufficiently high intensities. The two photon absorption is used in many areas of science and technology, from diodes for autocorrelators [20] to fluorescence microscopy [21].

When applied to DLW, two-photon absorption provides sub-diffraction resolution thanks to a small volume where the intensity of the laser exceeds the threshold (Figure 1).
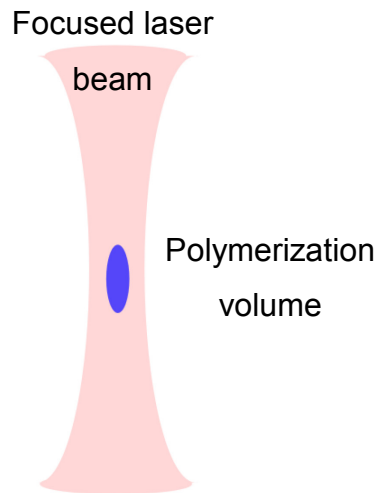
Figure 1. Two photon polymerization voxel appearance.

1.3.2 Direct laser writing

Direct laser writing (DLW) is a unique non-linear lithographic technique based on ultra-localized polymerization.

Considering the variety of employed materials and the three-dimensional fabrication of arbitrary elements by this technique, DLW is widely spread in microphotonics. Being based on local polymerization of a photoresist, it allows to realize complex 3D micro- and nano-structures for diverse applications in microoptics [22], photonics [23]–[25], micro-fluidics [26],biomedicine [27] and microrobotics. Some examples are shown in Figure 2.
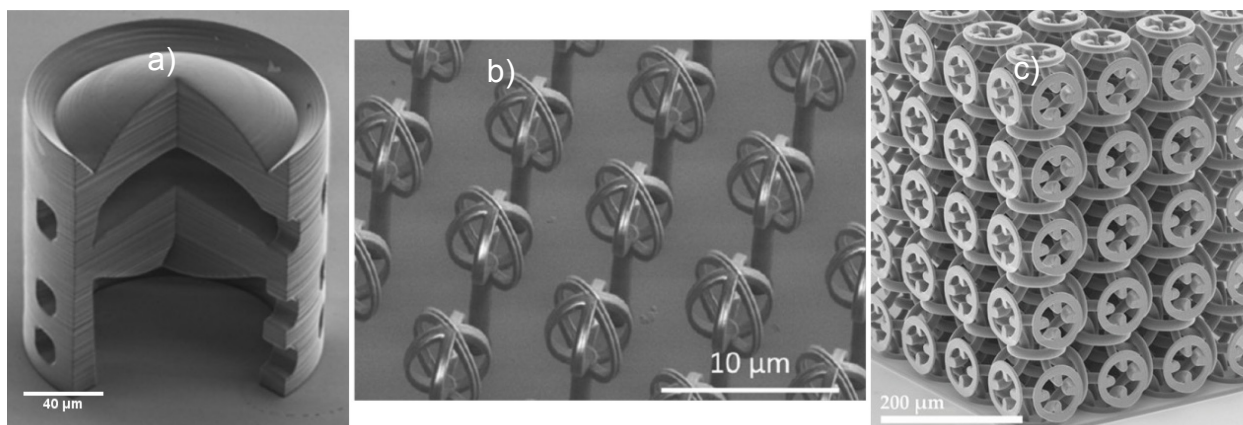
Figure 2. Examples of structures, fabricated with direct laser writing. a)-Microlens, that is used on top of a fiber (adapted from [22]); b)- bioinspired functional surface (adapted from [28]; c)-3D metamaterial mimicking p-type semiconductor can be made of an n-type semiconductor (adapted from [29]).

Furthermore, it allows integration of several components and combination of a few of the above mentioned functions [30]. DLW technique is attractive due to its versatility to materialize differentiated 3D models (also using CAD platform) made of a wide spectrum of materials on the desired substrates [30]–[32]. Moreover, DLW technique allows to pattern many geometries using different polymers opening to applications in many fields.

It is based on a non-linear photo-polymerization process that allows to transform the liquid resist in the desired polymeric structure. Laser induced photo-crosslinking and polymerization can be achieved by tightly focusing ultra-short pulses inside photo-sensitive mixtures [33]. A point-by-point exposure of a resist allows to write connected lines and surfaces. In 3D DLW, a pulsed laser is focused into a diffraction-limited spot inside the volume of a drop photoresist. Pulsed laser excitation provides high intensity inside the focus area that allows to employ non-linear processes within polymerization. A typical layout for direct laser writing system is showed in Figure 3.
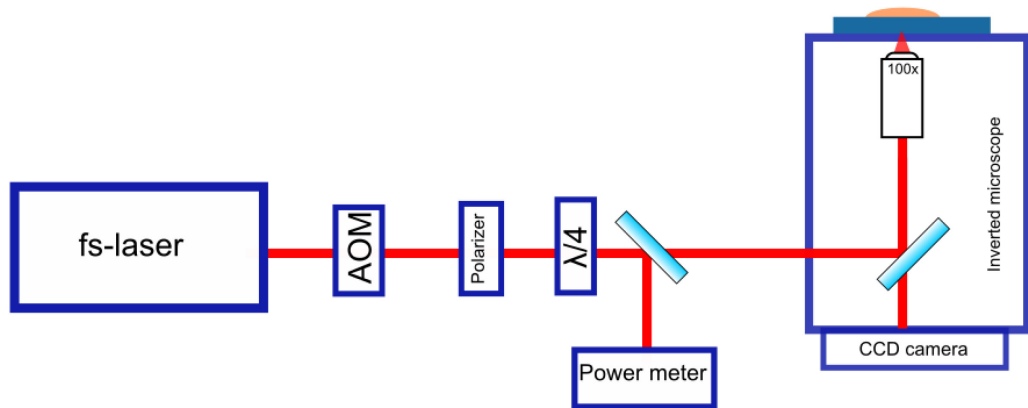
14

Figure 3. A typical layout of DLW system (here AOM stands for acousto-optical modulator, λ/4 stands for quarterwaveplate).

However, a possibility to achieve higher resolution has been demonstrated introducing the concept of stimulated emission depletion exported from fluorescence super-resolution optical microscopy by S. Hell [34]. If this idea is applied to optical lithography, the depletion DLW system (STED-DLW [35]) allows, inhibiting partially the polymerization and then effectively reducing the photoresist sensitivity, to reach a lateral resolution of 65 nm. Additionally, beam shaping techniques employing spatial light modulators (SLM) or diffractive optical elements (DOEs) can be used to obtain parallel processing and dramatically increase fabrication throughput [36].

Nonetheless, high resolution is not the most remarkable feature of this lithographic technique. In comparison with other fabrication techniques, for instance UV photo-lithography or electron beam lithography(EBL), it allows to create truly three-dimensional structures. The unique possibility of fabricating three dimensional structures, even employing different materials and even combing them within one structure (in several step fabrication process [37], [38]), is the key feature that differentiates DLW from e-beam lithography. Moreover, being a mask-less system,

15

with a simpler hardware than EBL, DLW is a low-cost technique not only in terms of purchase, but also servicing and fabrication. However, the disadvantage of the technique is that the fabrication process is time-consuming (the downside of high lateral resolution) and barely applicable for mass-production.

Exploiting two-photon absorption, the effectively exposed volume is restricted to the focal region and only in the central part of the laser spot, the light intensity overcomes the polymerization threshold. This threshold process leads to the polymerization of an ellipsoidal volume element, called a *voxel* (

Figure 1). The size and shape of voxels depend on the iso-intensity surfaces of the microscope objective, and the exposure threshold for multiphoton processes of the photosensitive medium. The lateral resolution of DLW in this case can reach values as low as 120 nm[39].

Despite of a variety of commercial and custom-made systems, in the present work all the DWL patterning was performed with DLW NanoScribe GmbH, that is owned by both institutes where current research has been conducted.

Figure 4. A photograph of DLW NanoScribe.

Two main configurations of DLW might be used for different substrates and resists. In conventional DLW an oil-immersion objective is used as depicted in Figure 5. In this case the maximal height of the structure is limited by a working

distance of the objective (usually not exceeding 40μm). However, so called dip-in laser lithography (DiLL) is also implemented in the used machine. The main difference from the conventional configuration is that in case of DiLL the immersion oil and photoresist is the same substance and, therefore, the fabrication process is reversed in the *z*-direction. Considering this, the limitation of the maximal height of the structure is removed (of course, the development process and the structure stability are yet limiting factors).
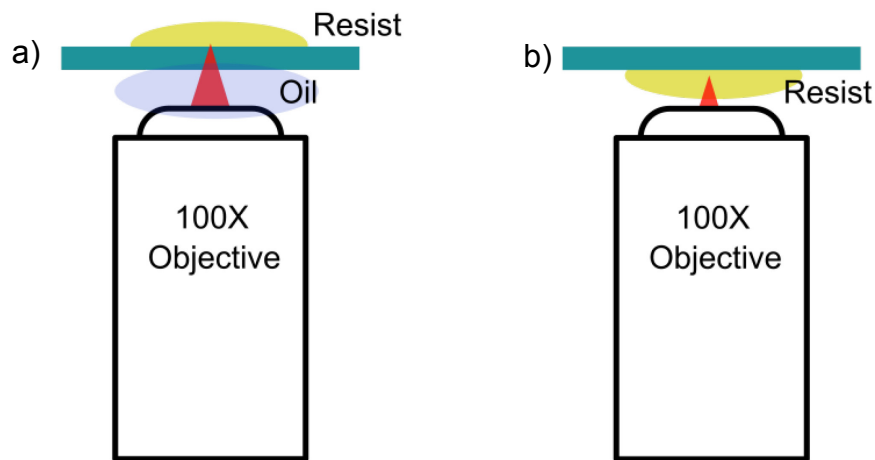

Figure 5. Conventional DLW (a) vs. DiLL (b).

A main concern while performing DiLL DWL is a proper choice of substrate – it must provide a sufficient refractive index contrast with the resist to maintain proper interface correction.

1.3.3 Materials for DLW

Numerous materials are available to be applied with a technique. By company itself several resists are proposed, which are optimized to achieve certain values of different qualities, such as resolution, shrinkage or surface roughness [40]. However, the possible materials are not limited by the company products and many custom-made resists exist. Interesting classes of the materials to be used with DLW should be noted separately are smart materials, for instance hydrogels[41] or liquid crystal

17

networks[42], [43] that have been already demonstrated to be compatible with this lithographic technique.

1.4 Electron beam lithography

One more wide spread fabrication method for photonic applications is electron beam (e-beam) lithography (EBL) [44]. The crux of electron beam lithography is the same as any other lithography - a resist changes its properties under exposure. Very often for photonics application poly(methyl methacrylate) (PMMA) is used. It has good optical properties as transparency in the visible and infrared region and good rigidity (more elastic that Ip-Dip of Nanoscribe with a lower Young modulus of $2-3$GPa). As in our case, it is employed as a common high resolution positive resist for electron beam lithography. Polymeric chains are broken by the electron shower and using a developer, the exposed part is removed. PMMAs use with e-beam lithography is well established and it represents one of the most popular e-beam resists, offering extremely high-resolution, ease of handling, excellent film characteristics, and wide process latitude. The refractive index of PMMA is commonly 1.48 for NIR. However, several modifications of the process are proposed, to increase the refractive index contrast. In one of them PMMA structures are written on a silicon structure and afterwards etching is performed [45] followed by thermal reflow. This process allows to form whispering gallery mode cavities with quality factors up to 10^6.

The fundamental condition, that the EBL substrate should satisfy, is to be conductive to not accumulate the incident electric charges that would then deflect the electron beam. The most widely used substrate is silicon with a thin insulating layer of silicon dioxide on top. Other possible substrates that can be used are glass plates coated with metal (ITO [46], chrome on glass, widely used in mask production).

18

The main parts of apparatus are resembling scanning electron microscope: electron gun (source), magnetic lenses and a stage, where the sample is mounted. However, the fact that all the system must be kept in vacuum makes the e-beam lithography more complex in terms of supply and maintenance.

1.4.1 Photonic components made with combination of poly(methyl methacrylate) and lift-off resist

It is worth discussing separately a technique proposed in [47]. Although the proposed sample fabrication process is used for preparation for UV-lithography, in current work we adapted it to be used with e-beam. The basic idea behind the process is to use a material, that can be chemically etched the same way as silicon in [45] . The sacrificial layer between resonator and substrate has to allow for selective and isotropic etching without damaging the PMMA resonators or polymer substrates.

For this purpose polydimethyl glutarimide-based lift-off resist is used (LOR 30B, Microchem Corp.). The full process is described in Figure 6.

The layer of lift-off resist is spin-coated on a substrate (it can be a silicon wafer or glass or any other substrate) and baked on a hot plate for thermal annealing. On the second layer PMMA (PMMA 950k, MicroChem Corp.) is deposited. Then after the lithographic exposure, the PMMA is subsequently developed in a 1:1 mixture of methyl isobutyl ketone (MIBK) and isopropyl alcohol (IPA), leaving a layer of LOR with structures on top. With this last step a selective wet etching is performed under-etching the PMMA structures.

a) Spin-coating of LOR and PMMA

PMMA

Lift-off resist

Substrate

b) Deep-UV exposure

Mask

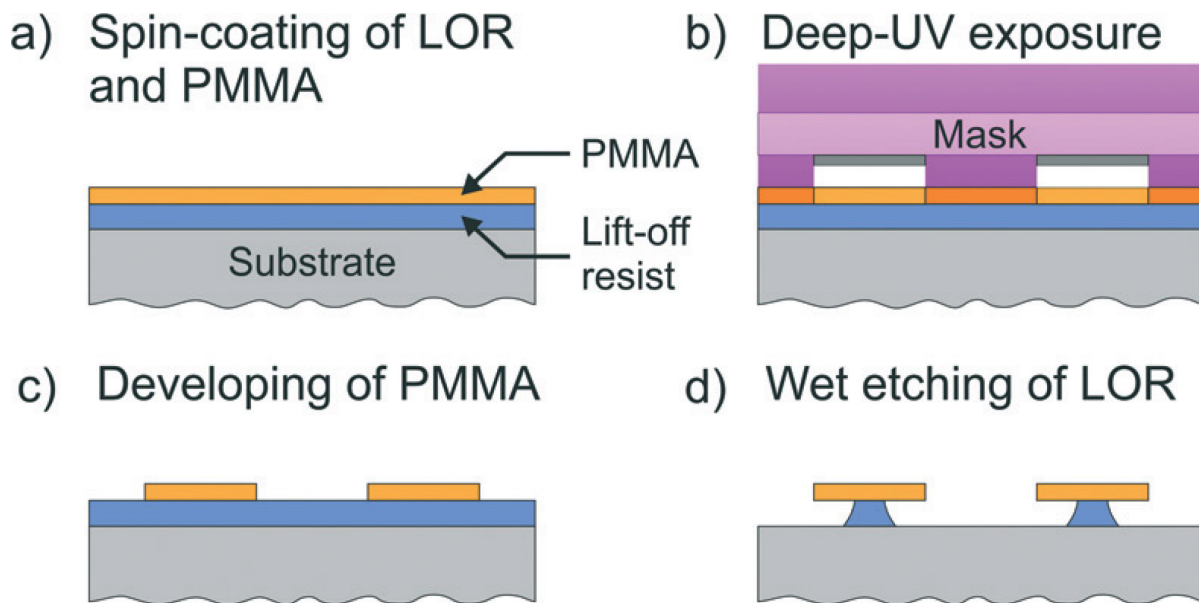**c) Developing of PMMA**

d) Wet etching of LOR

Figure 6. PMMA and lift-off resist processing (adapted from [47]).

For non-conductive substrates, a ≈ 50 nm layer of chromium is sputter-coated on top before the e-beam exposure and removed afterwards.

1.4.2 Advantages and disadvantages of the technique

The main disadvantage of the EBL is that all fabricated structures are restricted in two dimensions (or quasi two dimensions as described in [47]). The other disadvantage is connected with a complexity of the device and its expensive maintenance (vacuum pumps, sources, etc.).

However, the e-beam production of structures is defined by high throughput , extremely high resolution reaching sub-10 nm values [48], and high reproducibility.

2 Diagnostic tool for integrated photonic circuits.

2.1 Existing methods of photonic circuit diagnostic

In modern telecommunication technology for scientific application the variety of tools for complex diagnostics is not as wide as needed. Several techniques have been developed for fiber-based systems, for instance optical-frequency domain reflectometry (OFDR) [49] or optical time domain reflectometry (OTDR) [50], while situation with integrated circuits is slightly more complex. A coherent frequency domain reflectometry was adjusted to study integrated waveguides [51], but still could not overcome the resolution of 10um. Furthermore, the requirements for more complex systems, such as coupled resonator waveguides [52], [53], demand sufficiently different way of inspection.

In order to study integrated photonic components different kinds of approaches like far field scattering microscopy (FScM), [54] or scanning near field optical microscopy (SNOM)[55]–[57] have been proposed in last years.

At last, ultrafast photomodulation spectroscopy (UPMS) technique for complex analysis of various integrated photonic components has been proposed [58]. Using local photomodulation of refractive index of a specimen with UV femtosecond pulse, the technique allows to see the effect in the transmission signal of the system. Two main drawbacks of that approach are perturbation of the sample and scanning nature of signal acquisition.

In current chapter we introduce a new approach to perform a complex diagnostic of integrated photonic circuits. Based on the optical gating principle, the technique allows to access various system parameters while using a single configuration. At first, we introduce the detailed apparatus description and then as fully as possible describe the sample study methods.

2.2 Ultrafast imaging and complex diagnostic of photonic circuits

Here we report a novel apparatus that had been constructed for diagnostic, testing, and complex investigation of various photonic circuits. The idea of using pulsed laser for different kind of non-linear applications is caused by high energy per pulse value.

In many cases the time resolution of the imaging technique is defined by the detectors used in a given apparatus. While commercially available single photodetectors can reach time resolution up to several nanoseconds, array detectors are barely able to overcome a limit of tens of microseconds. However, if one has a desire to track a phenomenon connected with light propagation inside diverse media - either highly scattering disordered photonic structures or photonic crystals or even inside the integrated photonic circuits, much high temporal resolution is becomes mandatory. A task of building a device that is capable of femtosecond time resolution in the imaging process confronts some physical restrictions. Nonetheless, a completely different way exists to address this problem.

After invention of stroboscope (or, how the inventor called it "Phenakistoscope") in 1832 by Joseph Plateau it became a very popular tool for image projection of moving images. Within almost two centuries the principle of operation of the stroboscope remains relevant for various applications. The main idea of a stroboscope is to make cyclically moving object appear to be slowly and smoothly moving by briefly and repeatedly illuminating the object at different time during its periodic motion. Thus, if one turns on the illumination only in one particular moment of the cyclic process, then the object will appear static, "frozen" in that particular moment of the cycle. One of the well spread examples is when rotational frequency of a wheel or helicopter blades coincides with an acquisition frequency of a camera or matches with the physical "refresh rate" of the retina, producing the so-called wagon-wheel effect.

It turns out that the same trick can be performed with laser pulses and various photonic structures. Repeatedly exciting a structure with a laser pulse, with period equal to pulse repetition rate of the laser, one creates a cyclic process. Then a triggering mechanism, which is an equivalent of the flashes in stroboscope, should be turned on. All those requirements bring us to the idea of optical gating [59], that uses two pulses and non-linear media as a triggered acquisition mechanism.

Using pulsed laser to achieve temporally resolved information has been realized several times by different groups to explore ultrafast dynamics of light in different systems. Several sorts of systems, starting from fluorescence measurements [60] and, so-called, light bullets [61] and covering the vast range of applications up to biological[62] and disordered photonic samples[63].

2.3 Cross-correlation optical gating principle

In a typical optical gating apparatus, two synchronous, collinear *probe* and *gate* pulses are made to impinge on a nonlinear crystal. The *probe* pulse at frequency ω_1 (interpreted as the central frequency of the pulse bandwidth) interacts with device under study (DUT), acquiring a time-delay or experiencing any other time-dependent transformation, thus leading to the time profile $I_{\omega 1}(t)$. Conversely, the gate pulse propagates unaltered in free space preserving its original temporal profile $I_{\omega 2}(t)$. When the two pulses eventually reach the crystal, an upconverted signal at frequency $\omega_1 + \omega_2$ is generated and intensity depends on the degree of spatial and temporal overlap. This frequency mixing process is known as sum-frequency generation (SFG) or upconversion and occurs in nonlinear media with finite second-order susceptibility $\chi^{(2)}$. The intensity profile of the sum-frequency signal is given by the convolution integral of the intensities

$$I_{\omega 3} = \int_0^\infty I_{\omega 1}(t) I_{\omega 2}(t - \tau) dt, \tag{18}$$

where τ represents time-delay of one pulse with respect to the other. For a fixed delay τ, the resulting train of signal pulses $I_{\omega3}(\Delta\tau)$ has now a stationary intensity that can be detected and integrated with a slow detector. By scanning over the delay τ it is possible step by step to record the temporal evolution of $I_{\omega1}(t)$ using the unperturbed $I_{\omega2}(t)$ pulse as a temporal gate (hence the name of the technique), by performing a deconvolution operation.

In our particular case, we have built an apparatus that is capable of probing photonic structures with femtosecond pulses produced by Ti:Sapphire laser (Tsunami, Spectra-Physics) and femtosecond optical parametric oscillator (OPAL, Spectra-Physics).

The pulses produced by Ti:Sapphire are characterized by length of $\Delta t \approx 120\ fs$, wavelength $\lambda=819\ nm$ with spectral width of $\Delta\lambda=5\ nm$ as a full width at half maximum (FWHM). The output power can go up to $P=2.1\ W$ with repetition rate $\nu=80.5263\ MHz$. Each pulse passing through an optical parametric oscillator (OPO) is converted into two pulses with different frequencies (19), which are called *signal* and *idler*. In this case, a single photon is split into two, following energy conservation law.

$$h\nu_{pump} = h\nu_{signal} + h\nu_{idler} \tag{19}$$

However, due to limited efficiency of non-linear processes not every photon experiences a conversion process, thus leading to the existence of the residual pump beam in the output of the OPO.

In our setup, we do not use the idler beam, working only with signal beam (called *probe*, due do its application) and residual pump beam (called *gate*), serving as a trigger for the detection part of the apparatus). The signal wavelength can be tuned across a relatively wide range (1.2-1.6 μm), thus allowing for tunability of the probe pulse. The wide wavelength range broadens the application of the apparatus.

24

However, if the wavelength tunability of the *signal* beam does not cover one's need, there is a possibility to use *idler* beam instead, which is tunable in the range of λ=1.6-2.25μm. Most of the photonic components are designed to be used in C-band of telecom communications that is λ=1.55 μm.

The repetition rate of the OPO is equal to Ti:Sapphire laser therefore the produced pulses are synchronous and coherent. The average power output of *signal* beam is P=130mW.

The typical spectrum of the *probe* pulse (i.e. the one interacting with the specimen) is shown in Figure 7.
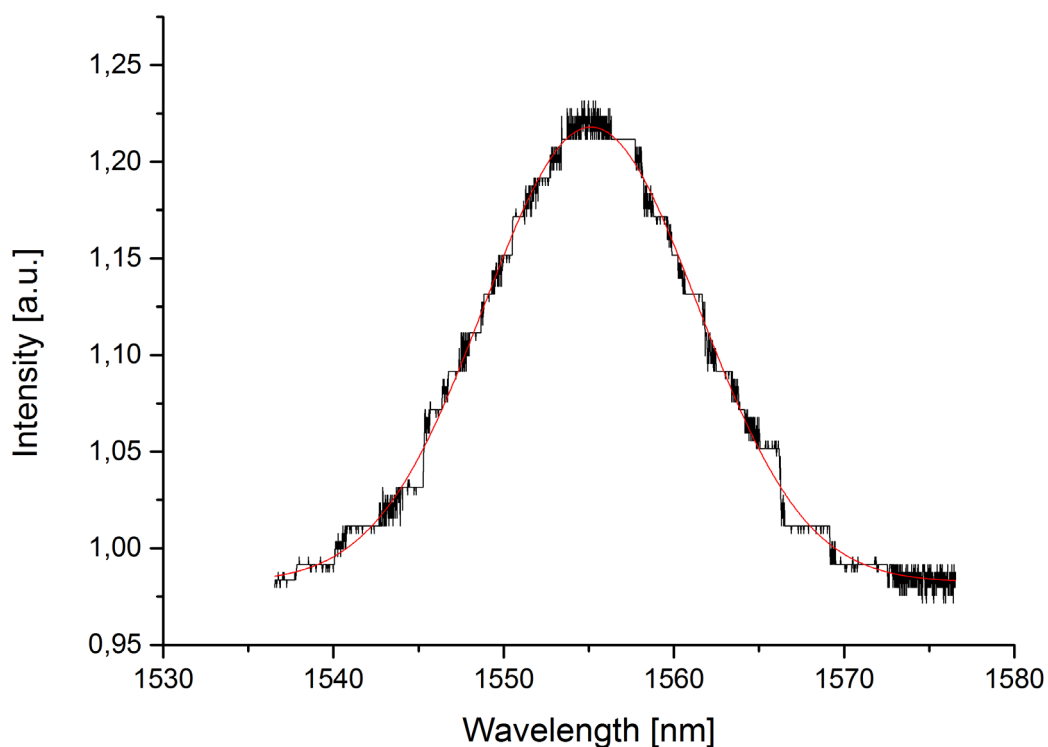
Figure 7. The spectrum of the probe pulse.

Precisely tuning the optical path of the two pulses it is possible to achieve their coincidence in time and space. Optical gating technique requires a nonlinear medium to be used. In the most cases crystals designated for frequency conversion

are used [61], but in some cases Kerr effect is employed [60]. In our case BIBO (BiB_3O_6) nonlinear crystal was used. The conversion efficiency of BIBO crystals has been reported to significantly exceed the LBO (LiB_3O_5) and BBO (BaB_2O_4) for sum-frequency generation for the same conditions [64]. The crystal thickness should be chosen accurately to have an optimal value within the interplay between imaging distortion and sum-frequency power generation. However, following the experimental process we discovered that at the initial stage of research the low upconverted signal intensity can be simply compensated by increasing the exposure time. Therefore, the crystal thickness has been chosen to be 0.5mm to decrease spatial and temporal walk-off effects.

In order to study not only temporal delay of the light in various samples, but also its spatial distribution, it is necessary to implement an optical imaging scheme. However, since the frequency conversion of the signal is involved a standard imaging design is not suitable. We implement two-stage imaging as follows: the image of the sample with use of an objective and a tube lens is constructed between front and back facets of the crystal, thus leading to a reduction of image distortion during the frequency upconversion process. After the crystal, a dichroic mirror cuts out all the wavelengths except for the sum-frequency generated signal. Using a lens, a pattern, which was constructed between the facets of the crystal and upconverted, is imaged on a CCD detector (Andor iKon M912) of an ultra-sensitive camera or focused in one spot inside a photo-multiplier tube (PMT). PMT allows to collect overall transmission through the sample resolved in time. Meanwhile the camera is able to register also the spatial distribution.

A chopper installed in the optical path of the *gate* beam is used for automatic background subtraction in the case when the PMT is used.

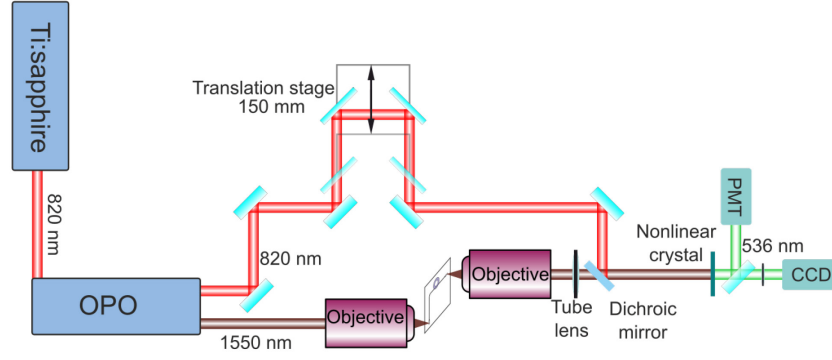The schematic representation of the apparatus is presented in Figure 8.

Figure 8. The schematic representation of the apparatus (here OPO is optical parametric oscillator, PMT – photo-multiplier tube)

2.4 Phase-matching and angular acceptance

The up conversion that lies in the base of the optical gating idea critically depends on the phase-matching of the two interacting pulses, as a momentum conservation law requires.

$$\boldsymbol{k}_{\omega_1} + \boldsymbol{k}_{\omega_2} = \boldsymbol{k}_{\omega_3}, \tag{20}$$

where $\boldsymbol{k}$ is a wavevector of a wave with angular frequency ω, indices 1,2,3 correspond to waves participating in the upconversion process.

In the collinear case, when all the waves propagate in the same direction, Eq. (20) turns into scalar equivalent:

$$\omega_1 n(\omega_1) + \omega_2 n(\omega_2) = (\omega_1 + \omega_2) n(\omega_3), \tag{21}$$

where $n(\omega)$ – refractive index of a media at angular frequency ω.

Considering a birefringent crystal medium, one can exploit the variation of refraction index depending on the direction of propagation. Choosing the direction and polarization of incoming waves carefully it is possible to satisfy Eq. (21). In a uniaxial birefringent crystal with optic axis, both ordinary and extraordinary (polarization perpendicular to the plane) rays are defined, seeing refractive indices

27

of n_o and n_e respectively. Each intermediate combination will yield a correspondingly weighted value of the effective refractive index along that direction, which allows to satisfy (21) by tuning the angle of incidence.

Uniaxial crystals are classified as "negative" if $n_e < n_o$ and "positive" otherwise. In the former case the possible polarization combinations are o+o→e or o+e→e with the sum-frequency necessarily polarized along the extraordinary direction, while for positive crystals it must be ordinarily polarized, i.e., e+o→o or e+e→o. Irrespective of the sign of the birefringence, the interaction is termed of type I if the incident beams have parallel polarization, and type II otherwise.

The angular acceptance on the crystal is an important parameter for the upconversion process and in details is discussed in [63], [65]. However, since in our case we use an objective with infinity corrected tube lens leading, in principle, to parallel rays, and therefore, in our case we exclude this issue from consideration.

2.5 Spatial and temporal resolution

In order to describe the apparatus, we perform spatial and temporal resolution characterization of the technique. Temporal resolution of the system is defined, mainly, by duration of both pulses participating in sum-frequency generation process, and, more precisely, by cross-convolution of the two pulses and precision of the translation stage position.

The translation stage allows to position the set of mirrors with a precision of 1 µm. Using (22) we easily get a value of ≈3.3 fs. However, as it will be shown later, this contribution is not significant for our case.

$$\Delta t = \frac{\Delta x}{c}, \tag{22}$$

28

where *Δx* -positioning precision of the translation stage expressed in units of length, *Δt*- precision of positioning of the translation stage, expressed in units of time, *c*-speed of light.

We still can fully describe temporal resolution simply performing the scanning of time-delay in absence of any sample. This measurement reveals a main peak full width at half maximum being of roughly 290fs (this value slightly changing from one experiment to another, being dependent on lasing conditions and, therefore, being affected by external parameters like, for instance, temperature variation in the laboratory) - Figure 9.
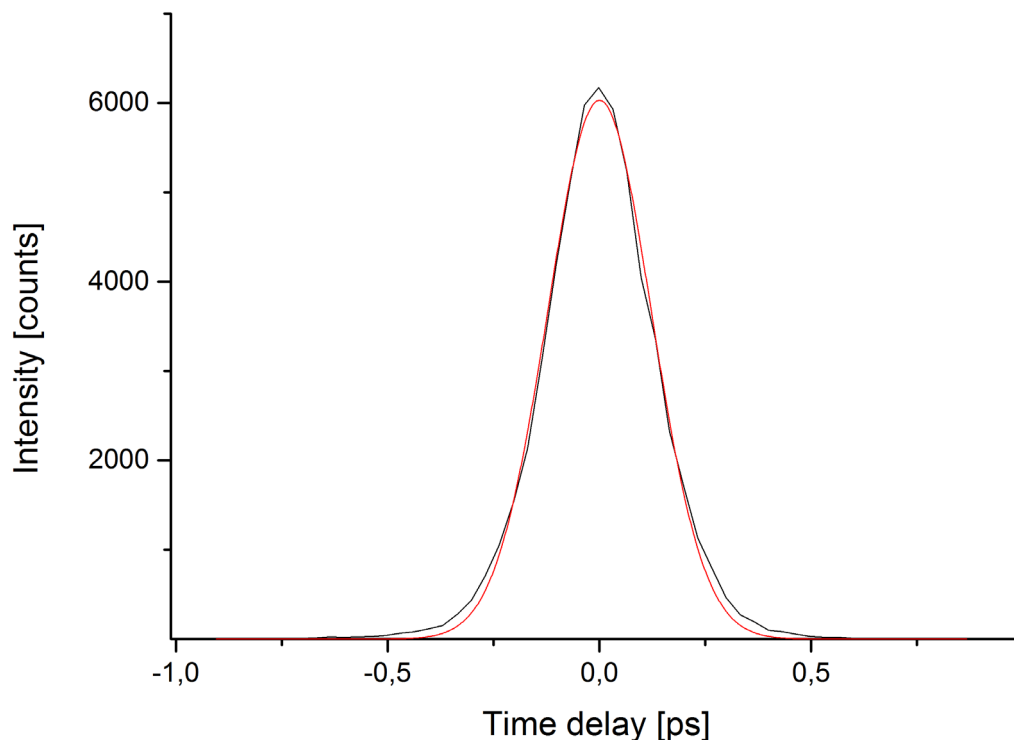
Figure 9. Time-resolution characterization: cross-correlation measurements.

Nevertheless, there is one more factor affecting signal acquisition: as well known, the pulsed lasers produce no single pulses, but rather trains of pulses. In this case the main pulse, like the one in Figure 9, are orders of magnitude more intense comparing to secondary and other satellite peaks following the main one. However,

those peaks play significant role in case of weak signals. As it will be shown later, the free range of time delay (in other words, time delay between main pulse and first secondary pulse) is around six picoseconds, that is enough for current application. If, however, one might need to measure effects that occur on longer time-scale, the effect of secondary pulses can be removed during data processing.

The spatial resolution depends on several factors: set of the objectives, non-linear crystal thickness and properties, detection camera. We must note, that the desired signal is carried by infrared (1.55 µm beam) and then is upconverted into green beam that facilitates the detection and, therefore, improves the quality of the final detected image. However, since the imaging is performed with use of non-linear media, the images suffer from aberration, caused by image doubling due to birefringence.

We used standard resolution test targets for resolution calibration (USAF 1951 negative, *ThorLabs, Inc.*) and varied collection objective from 10x magnification (Figure 10-a) to 50x magnification (Figure 10-b).
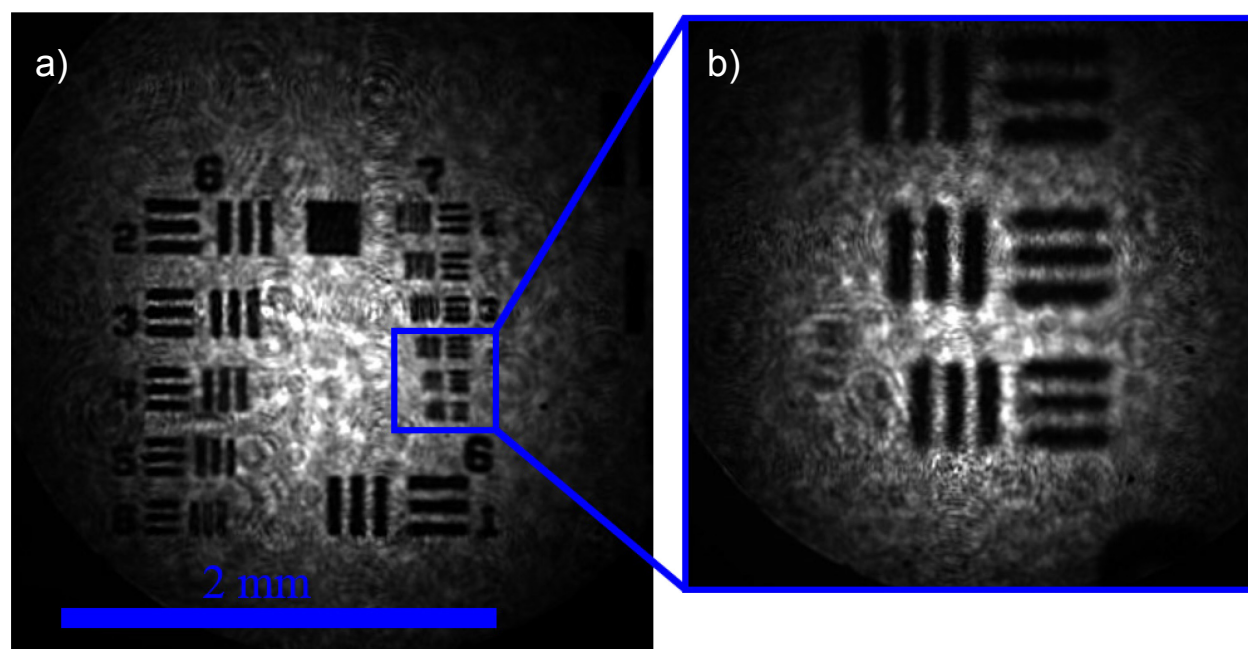
Figure 10. Spatial resolution test.

Obviously, the smallest feature of the resolution target is the bigger than maximal resolution achievable using a 50x magnification objective, therefore, we have to estimate the resolution using structures that we use in our research. As it will be shown later, the smallest feature size that can be imaged with use of 100x objective is approximately 1 µm.

2.6 Objects under study.

The complex tool for characterization and study of integrated photonic circuits should be capable of various types of analysis of different samples. To demonstrate versatility of the designed technique we perform investigation of the properties of linear and non-linear elements.

In the present work, we demonstrate the analysis of the following types of devices:

- Optical waveguides
- Polymeric single whispering gallery mode resonators

1.1.1. Optical waveguides.

The waveguides to be studied are designed using finite element method with help of commercially available software (COMSOL).

A waveguide for our application is designed to support only fundamental TE mode. The refractive index of the polymer is known to be $n_{IP-dip}=1.54$ while fused silica glass substrate has refractive index $n_{substrate}=1.46$. Including those parameters into the model and optimizing parameters, we calculate the effective refractive index to be $n_{eff}=1.4831$ for a rectangular waveguide with the size of 2.2µm ×2.2 µm for TE mode at the wavelength $\lambda=1.555$ µm.
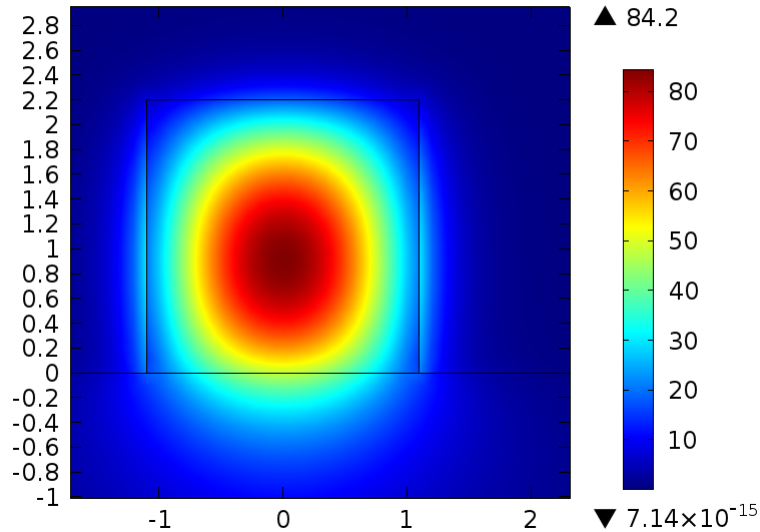
Figure 11. Mode analysis of polymeric waveguide: Electic field norm.

In order to be able to excite the mode from free space with an objective (trying to avoid micromanipulation and with a fiber) a grating coupler, based on the Bragg's law is designed using 2D geometry and effective refractive index approximation. Although achieved coupling efficiency is below 5% and relatively low comparing to analogous devices, it satisfies the needs of current research (Figure 12).
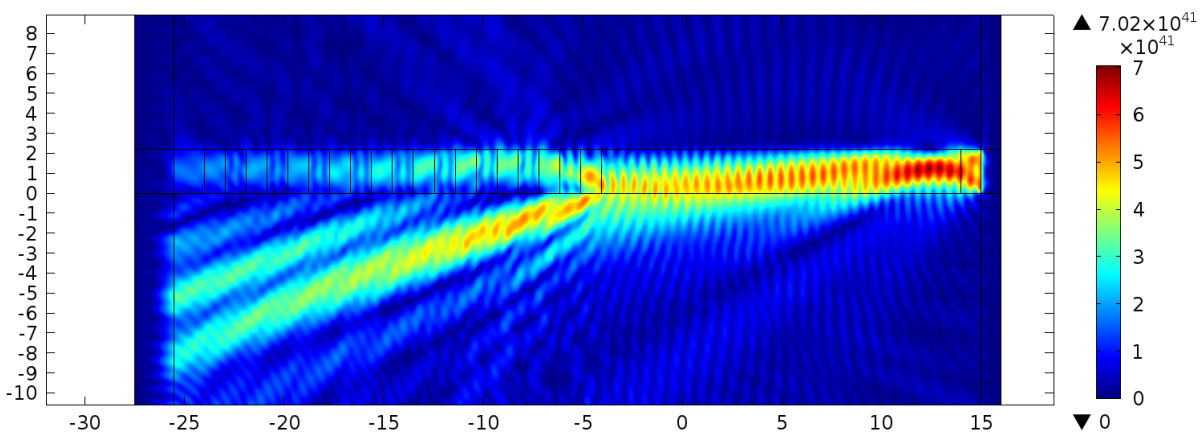
Figure 12. Grating output coupler model output showing non-zero power flux in y direction.

The shape of the waveguide is designed to have 90-degrees change of the direction along its overall path, in order to facilitate the background subtraction while the measurement using polarization selective detection. The curvature of the

32

bent region is set to 30µm to keep the losses small. The very basic information to be extracted from a single-mode waveguide is an effective refractive index of the structure.

Let us describe a typical experimental procedure that is applied to any further measurements. The probe beam is focused by an objective (usually 10x magnification) into an input coupler of the device under test (DUT). At the first step, the collection objective is focused on the same input coupler to collect direct transmission. This measurement defines the exact moment when the probe pulse enters the structure, therefore, it is chosen as origin of coordinate axis of time delay. In a second step, depending on the region of interest, the light is collected from it. To distinguish effects introduced by different parts of DUT from effects of a substrate and other components of the setup, it is necessary to perform the same kind of transmission measurements, but using only a substrate.
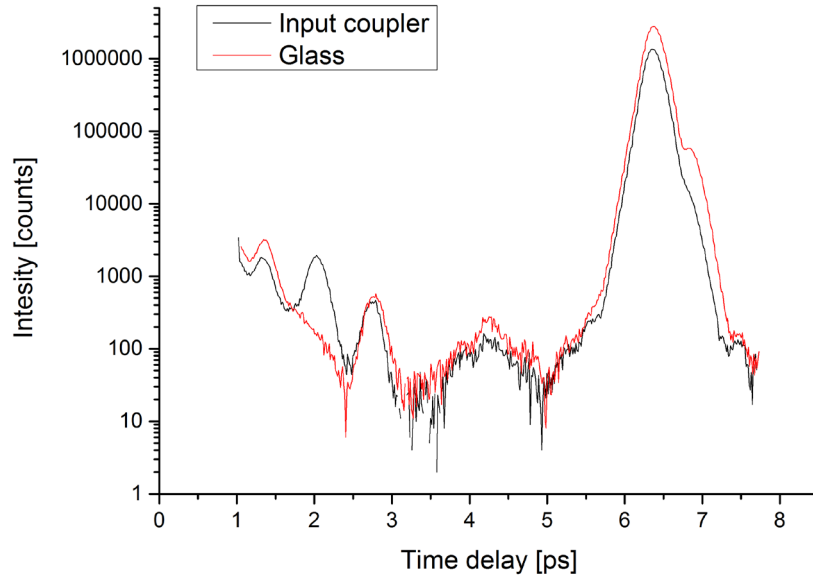
Figure 13. Time trace of transmission through the input coupler of a waveguide.

On the Figure 13 we show the time resolved transmission through the input coupler of a waveguide(*black*) and through a substrate alone(*red*). A clear difference

33

between the curves occurs at the time delay of $\Delta t = 2.03$ps corresponding to a backscattering from the far end of the waveguide under study. The mismatch of intensity of the remaining signal can be explained by the power variation during long term laser operation.

The conclusion about the backscattering nature of the peak discussed above is done combining time-resolved transmission measurements together with ultrafast imaging, showing the bring region at the position corresponding to input coupler.

The next stage in the investigation of the properties of a waveguide is a measurement of time resolved transmission through the sample. In this case the collection objective is set in the position to collect transmitted light. Time resolved trace shows several peaks with small time delay difference. However, it was verified that the first peak corresponding to the time delay $\Delta t \approx 0.5$ ps is simply a parasite reflection propagating through the substrate. The second peak, which has a time delay $\Delta t \approx 1.3$ps is of interest. The position of the peak, meaning the time-delay, carries the information about effective refractive index of a particular mode of the waveguide and the calculated value is $n_{eff} = 1.48$ that is in agreement with the model.
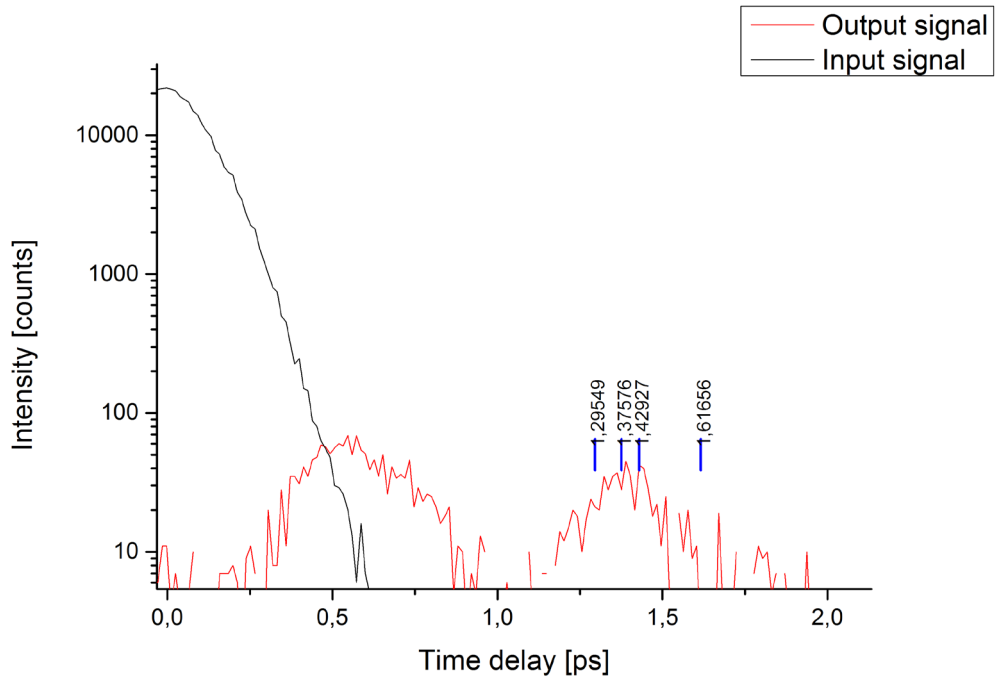
Figure 14. Time-resolved transmission trough a waveguide. Black line indicates signal collected from the *input* coupler, red line indicates the signal from *output* coupler.

More information can be extracted using the CCD camera for collecting information about spatial distribution of the signal. Time frames are recorded in correspondence to four different time delays that are indicated by four blue vertical notches in Figure 14. All four time-frames are taken acquired at time-delays *Δt* (shown in Figure 14) laying in the limits of the peak discussed above. In Figure 15 a)-d) is clearly visible the time evolution of the pulse that due to low efficiency of the grating coupler propagates for the length of about 20µm (length of the grating). All the time-frames are normalized in the same way in order to compare the intensity change. Every frame contains only time-resolved upconverted signal. A simulation, showing a steady state scattering pattern was performed using FEM (COMSOL) and the result together with an optical image of the grating is depicted in Figure 15 e)-f).

Measuring precisely the time delay, that the *probe* pulse acquires while propagating in the waveguide and precise length of the waveguide it is possible to calculate phase velocity and, therefore effective refractive index of the mode (23).

35

$$n_{eff} = \frac{\Delta t \cdot c}{l} \qquad (23)$$

where n_{eff}-effective refractive index of the mode, Δt – time delay of the pulse, l – length of the waveguide (or other object under study), c – speed of light.
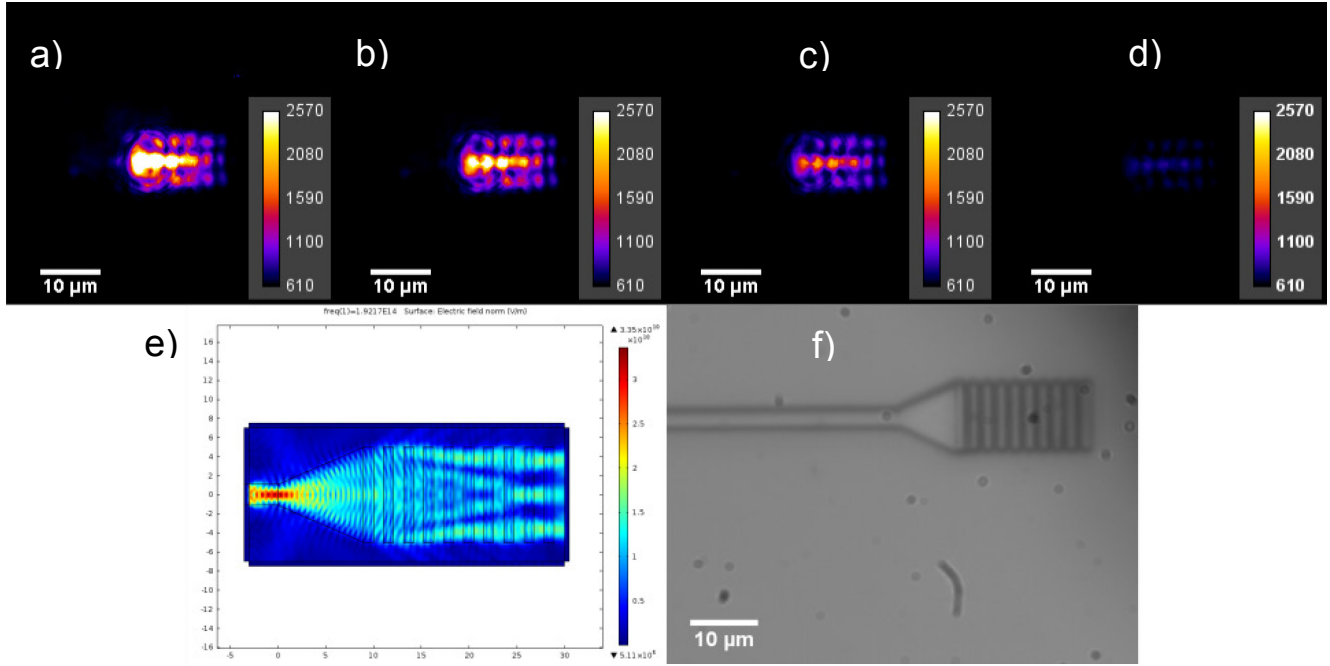

Figure 15. a)-d) Sequence of time-frames that describes a pulse being coupled out of the waveguide, e) FEM simulation of intensity distribution for an output coupler, f)- optical image of an output coupler.

The important application of the current technique is imaging of the defects of the structures. We have designed and fabricated defects in the waveguides of varying the length and the depth. Since the fabrication process of DLW produces some number of defects, on one of the waveguide there is an area with polymer burned, that is also being considered. Introduced defects do not significantly deteriorate the characteristics of the structures.

In the current experiments, we used low magnification collective objective (20X) to be able to image the complete structure within field of view. However, the disadvantage of this approach is that there is no spatial filtering of the input signal that, in this case, introduces some non-flat background.

36
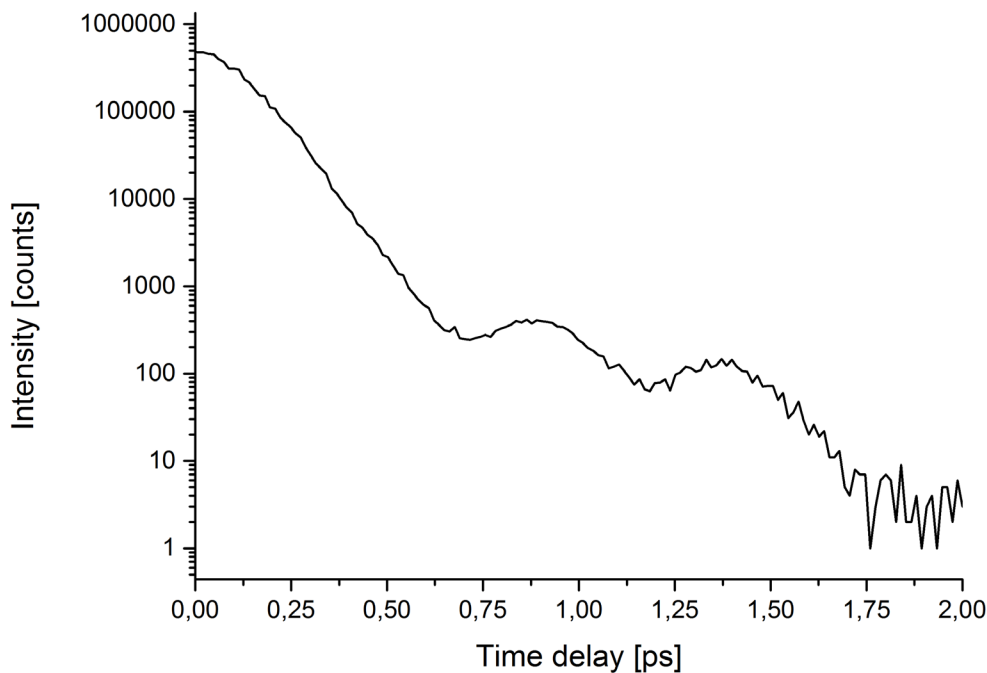
Figure 16. Time-resolved trace from the waveguide with two scattering defects.

The two defects discussed above are situated close to each other comparing to pulse length –at the distance of around 48µm. In this case the overall transmission is not able to resolve in time events, when pulse reaches the first defect and then the other. Both those events are merged together into a broad peak from time delay $\Delta t \approx 1.25$ ps up to $\Delta t \approx 1.75$ ps. However, in this case the imaging helps to sort out events and even identify both time coordinates. Apart from detecting and distinguishing defects by the means of imaging, they can be also used to increase the precision of the effective refractive index calculation. Here and after (if not stated otherwise) every image is a combination of two frames: the first, is time-resolved investigated signal (outcoupled through a grating coupler or another way); the second – an image of the sample that is illuminated by unfocused collimated beam in order to get information about sample alignment and positioning (however, acquired with the same mechanism – upconverted image). Then a background image is adjusted in brightness and contrast and is combined with the useful signal.
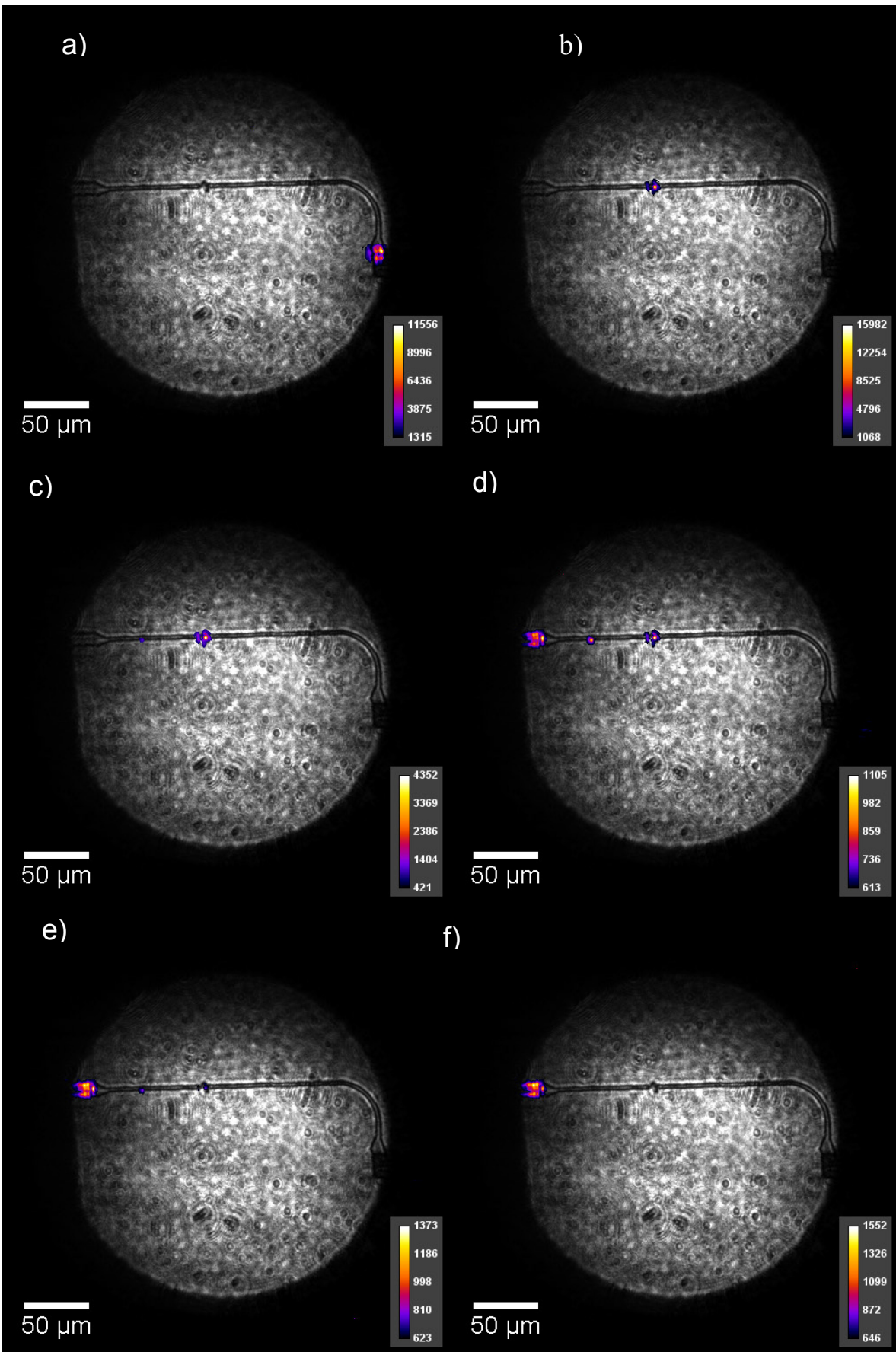
Figure 17. Time frames, showing scattering defects reacting on pulse propagation.

1.1.2. Polymeric single whispering gallery mode resonators.

Whispering gallery single mode resonators are fabricated by the DLW with IP-DIP polymer. To couple the laser radiation into the WGM ring the waveguides from the previous chapter are used. Each resonator is placed in close proximity to a waveguide in a way that evanescent fields of the modes of the waveguide and resonator will overlap, thus leading to energy leak form the waveguide into the resonator. The light inside the ring, trapped by total internal reflection circulates and couples out through the same bus waveguide. While usually a waveguide and a ring remain in the same plane, in our case we study more complicated system when WGM resonator and waveguide are stacked vertically.
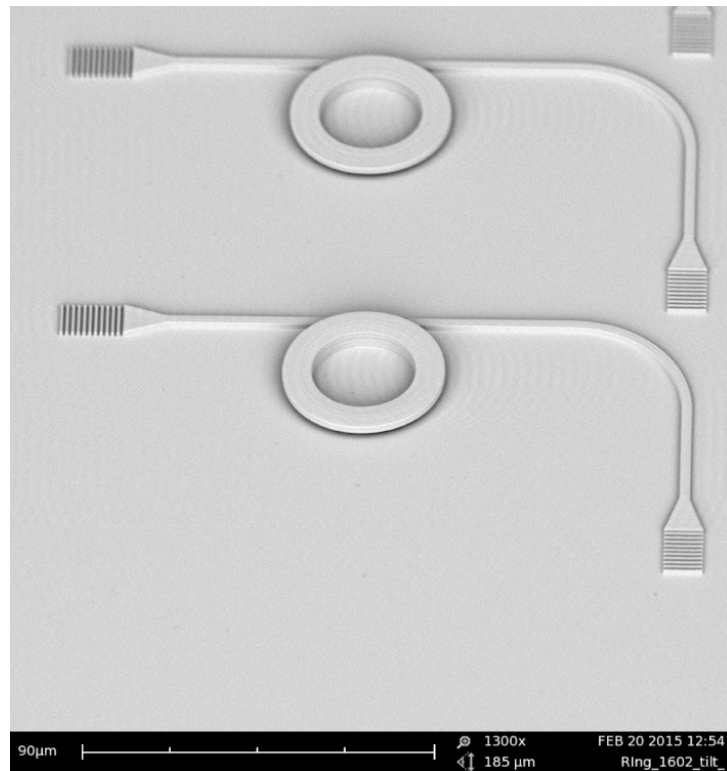
Figure 18. SEM image of a whispering gallery mode resonator together with a waveguide and grating couplers.

2.6.1 Resonance linewidth measurements

For the WGMR integrated circuits resonance linewidth measurement we use a simple transmission setup reported in Figure 19.

The circuit has been realized to work in the telecommunication band. The source is a continuous tunable NIR laser (Photonetics TUNICS-plus SC) with a tunable range from 1460 nm up to 1570 nm and a minimum step of 1 pm. The laser light is not polarized so in order to have an impinging TE mode on the input coupler, a polarizer and a half wave plate (for the NIR range) are placed in front of the sample. The light is then focused on the input grating through a 20X objective (Mitutoyo Plan NIR). A 4X objective is used instead to collect the light coming out from the output grating at the end of the waveguide. To selectively detect only the guided light from the 90∘ bent waveguide, a second polarizer, is placed after the sample in a cross-polarization configuration, is placed after the sample. In the sample image plane, a pinhole is positioned to spatially filter the output grating. This image is then reconstructed through a doublet or on the NIR camera (Phoenix Camera System INDIGO) or on the NIR photodiode, using a flipping mirror.
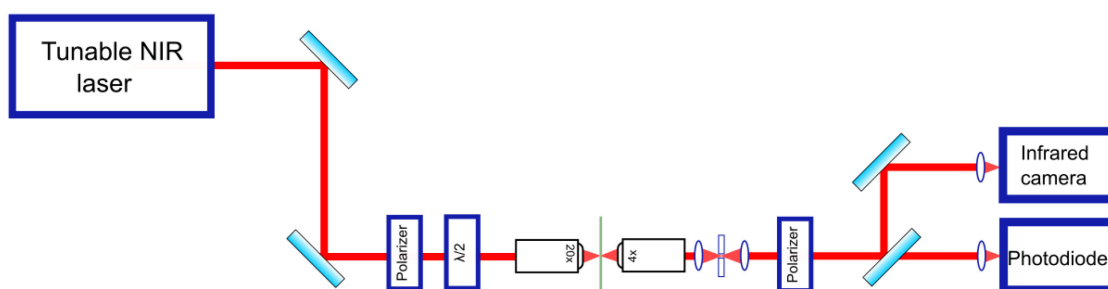
Figure 19. A layout of apparatus for cavity characterization.

The optical image allows to see when the incoming beam is well focused on the input coupler. Once the light is coupled into the waveguide, a bright spot appears at the waveguide output grating, representing the guided and transmitted light. The spectral measurement is then realized flipping the mirror that switch the light from the camera to the photo-diode. A wavelength sweep of the tunable laser is set to record the waveguide spectrum. Because of low efficiency of the grating and a

40

resulting low waveguide output, a modulated signal is employed which is later deconvolved using a lock-in amplifier. The waveguide transmission is then normalized to the glass substrate transmitted signal. Due to the fabrication parameter sweep and the not perfectly reproducible lithographic results, cavities with quality factor from hundreds up to tens of thousands have been fabricated.

A typical spectrum of WGM resonator is shown in Figure 20. Two sets of dips are clearly visible. They correspond to two modes with quality factors $Q_1=1225$ $Q_2=3100$ with *FSR=12nm*.
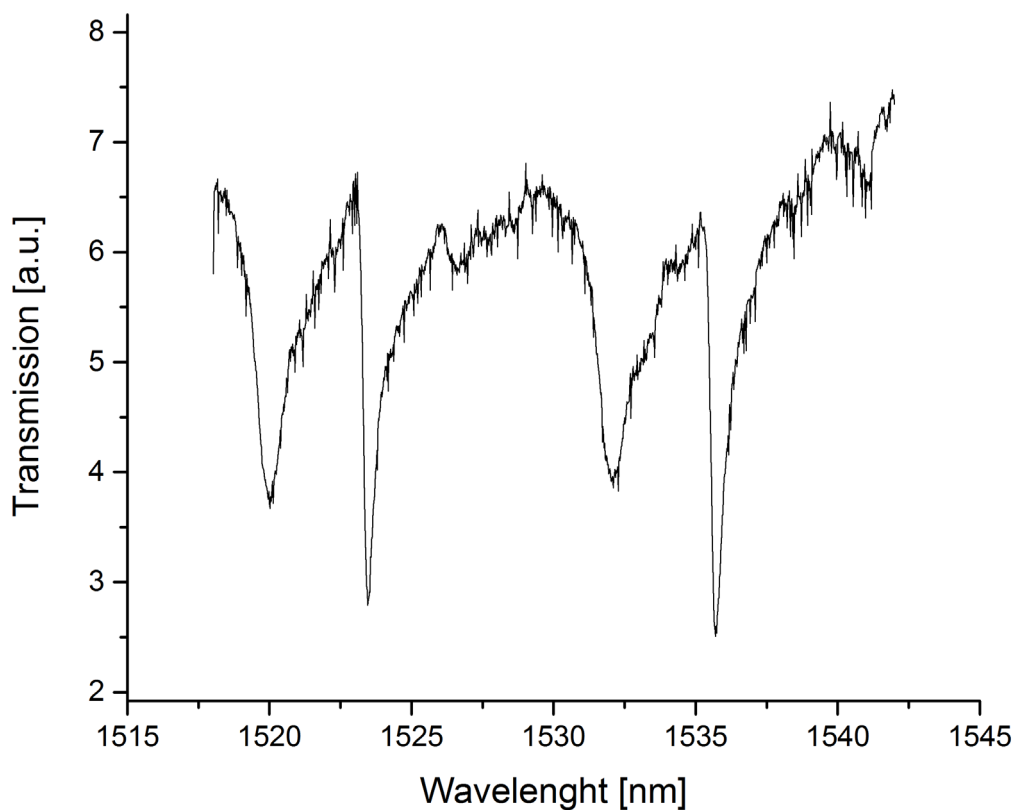
Figure 20. Two resonant mode in the spectrum of WGM laser.

2.6.2 Cavity characterization with time-resolved measurements

The rings obviously have resonances at slightly different wavelengths. Yet, the probe pulse, being as wide as *Δλ=19 nm* (Full Width at Half Maximum) covers at least two resonances in the transmission spectrum of the ring.

41

Quality factors of the resonators can be estimated by a variety of methods. In our case, time-resolved transmission through the waveguide-resonators assembly allows to resolve in time each roundtrip of a pulse inside the resonator and thus calculate Q-factors in a manner that is similar to cavity-ringdown spectroscopy. If compared to linewidth measurements, this strategy that is much closer to the real definition of quality factors and more even more intuitive.

The investigation of the coupled cavity-waveguide system is performed in the same way as for the single waveguides. A time-resolved transmission through the waveguide without a ring coupled is used as a reference to facilitate peak identification procedure. As clearly seen from the Figure 13 the input signal has non-flat nature and can be described as a train of pulses. Nevertheless, due to limited efficiency of the couplers only significantly intensive pulses affect the output signal. The typical transmission profile for a waveguide without a coupled resonator shown in Figure 21. The time delay zone up to 6 ps is left undisturbed in the case of our samples and (as will be shown later) is sufficient for current purpose.
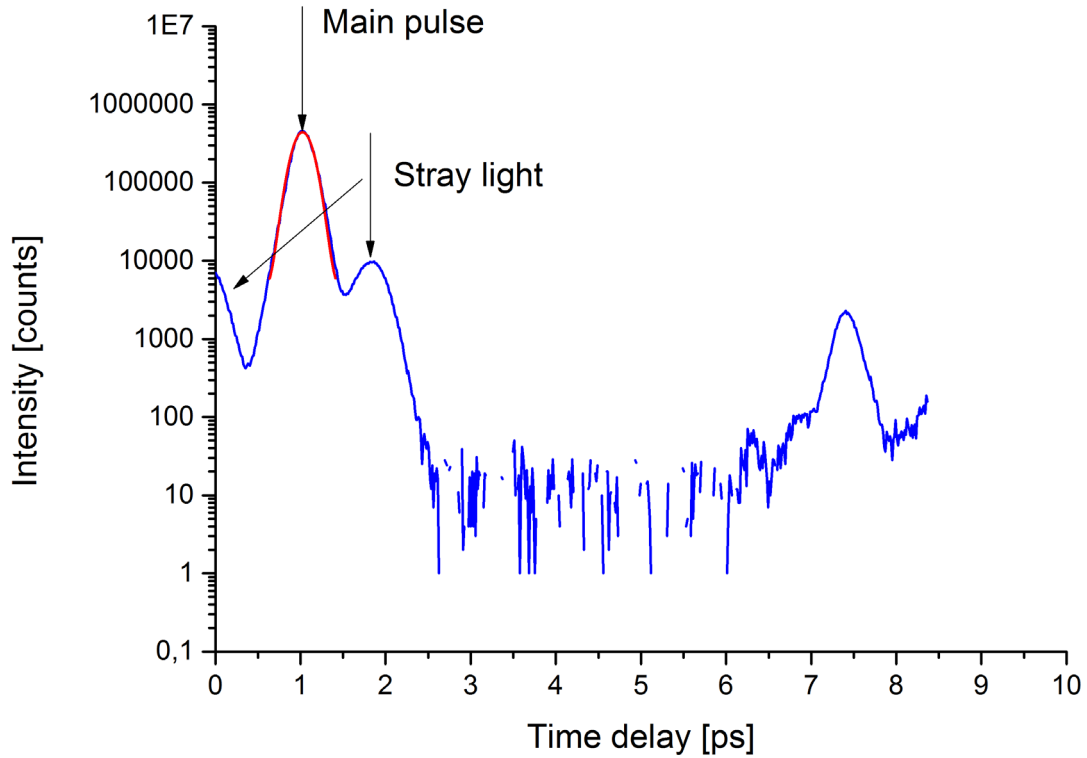
Figure 21. Time delay range for a study of waveguide-resonator assembly that is free of any side peaks.

Figure 22 depicts the time trace with clear time effect of a resonator. Each single roundtrip of the pulse is recorded. The dependency shows the exponential decay of the power stored in the resonator that is in accordance with theoretical prediction. Considering that information about the time that a pulse needs to make a roundtrip in the resonator is present the effective refractive index of the mode can be calculated as in the case of a waveguide.

Each single peak that corresponds to the effect of the WGM resonator is approximated with a Gaussian fit to calculate the area below it. Then using this information together with the coordinates of the centers of mass of the peaks the decaying exponential fit is performed.

$$I = C + I_0 e^{-\frac{x}{\tau}} \tag{24}$$

43

Since the energy stored in the resonator is decaying to approach zero therefore the C parameter is set to zero. Using exponential approximation, the decay time and quality factor are calculated.

$$Q = \frac{2\pi c\tau}{\lambda} \tag{25}$$
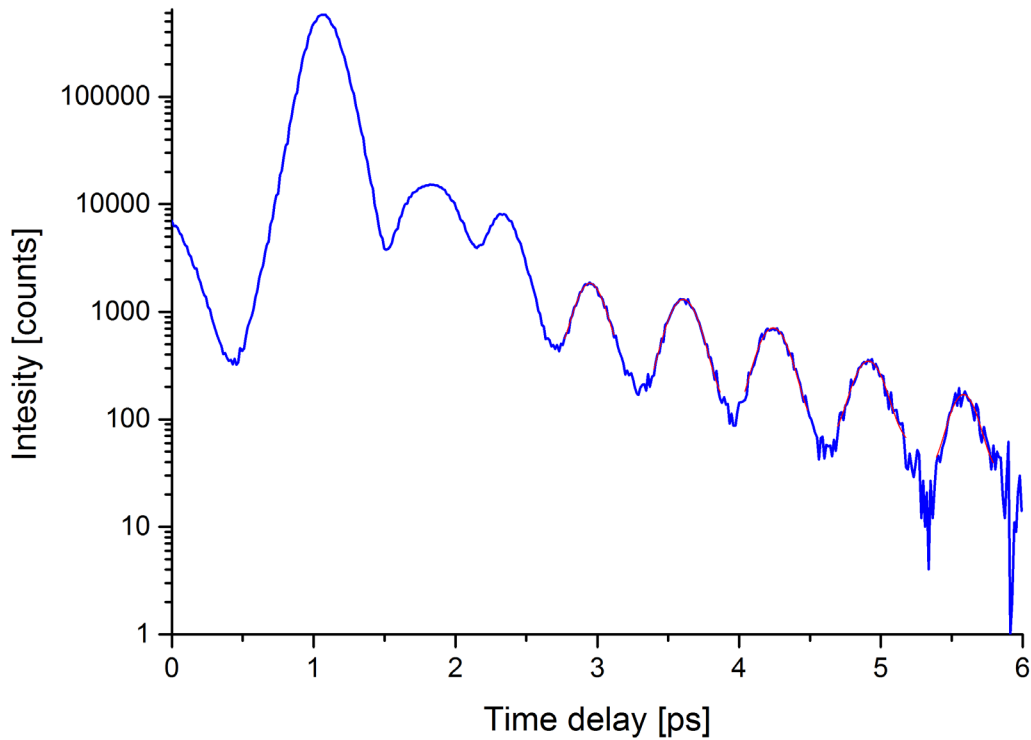
Figure 22. Time-resolved transmission trough the waveguide-ring assembly, showing fringes that imply energy leaking from a resonator into the bus waveguide with exponential decay.

The exponential decay becomes evident if one plots in a graph only positions and intensities of the different (Figure 23). Although the peak at $\Delta t \approx 2.3$ *ps* results from the resonator effect, we excluded it from our analysis, because its intensity is affected by the stray light at $\Delta t \approx 1.9$ *ps*.

44
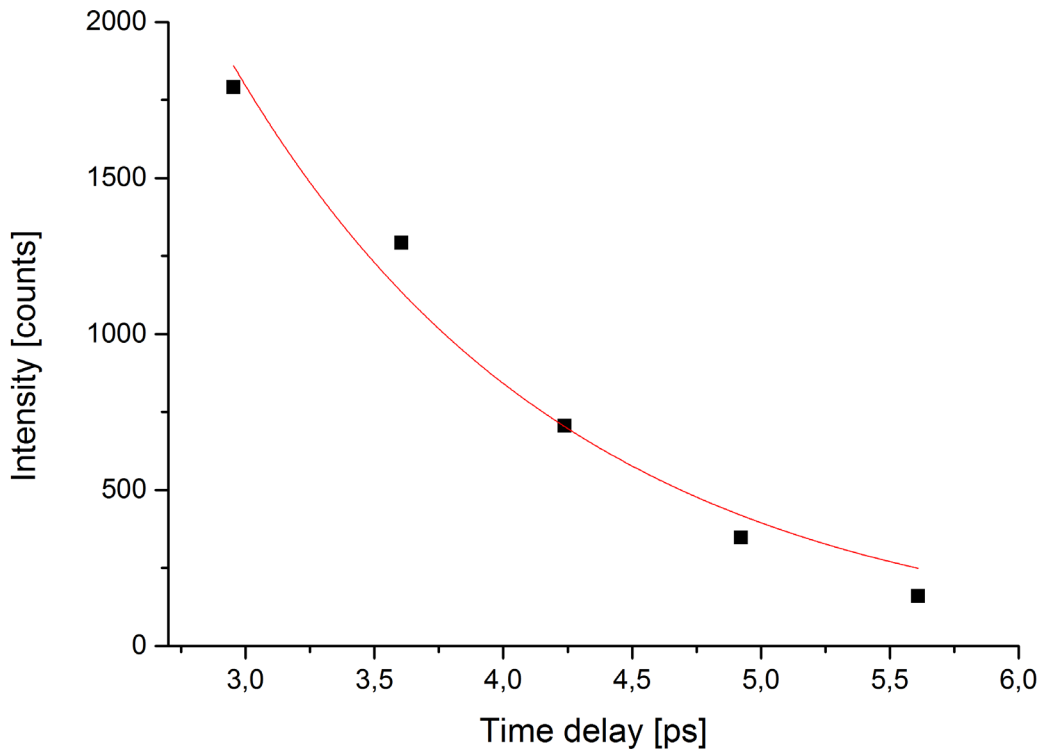
Figure 23. Exponential behavior of energy dissipation rate.

The time decay parameter extracted from the approximation is τ=1.32 ps and quality factor is *Q=1600*.

2.7 Direct imaging with the use of scattering particles.

The big disadvantage of the technique described above is that only losses from photonic circuits allow imaging to be performed. However, in many devices imaging a mode can be of interest. Near-field techniques can provide this kind of information both in steady state and resolved in time. In our work within the frame of the complex diagnostics we make an attempt to acquire the information about light propagation *inside* a device under study.

To perform an imaging of the light pulse propagation inside the structure it is necessary to introduce a mechanism that will extract small amount of energy that can be detected by the apparatus. For this purpose, we have investigated the

reversible addition of TiO_2 nanoparticles in a proximity to the polymeric structure that we investigate.

We performed a finite element method (FEM) simulation, trying to discover if presence of titanium dioxide nanoparticles disturbs the propagation mode of a waveguide. We consider the refractive index $n_{TiO2} \approx 2.46$ at the wavelength of interest $\lambda = 1.5$ μm and an approximate size of a single particle of 200-300 nm. Although in the current model the considered geometry implies a presence of infinitely long TiO_2 rods along the waveguide it is still clear that the mode is not disturbed significantly and variation of effective refractive index Δn_{eff} is smaller than 0.01.
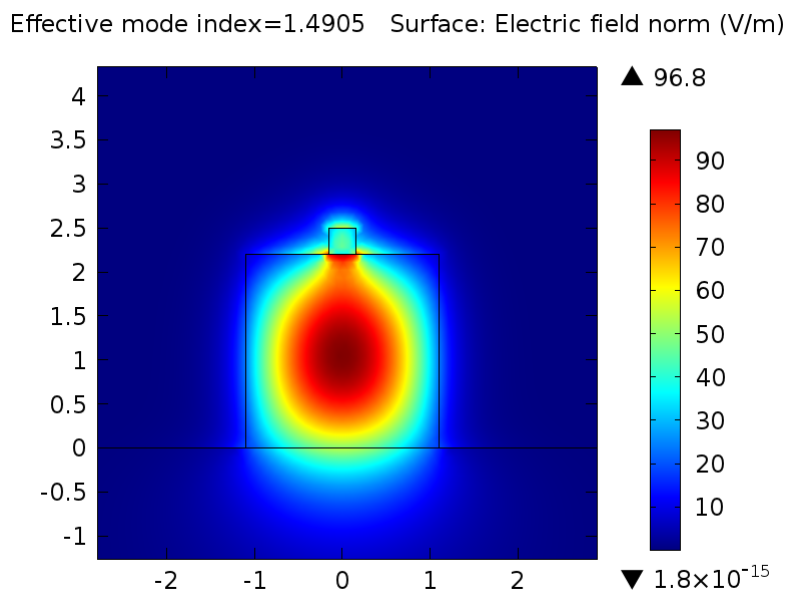
Figure 24. Mode distribution inside a polymeric waveguide in presence of TiO2 "particles".

In order to achieve a homogeneous distribution of the particles on the substrate and the DUT we prepared a suspension of TiO_2 nanoparticles in isopropyl alcohol (IPA). The desired amount of nanoparticles (depending on the density and therefore the area to be covered) is put inside a glass container together with IPA and sonicated for 15 min in order to break TiO_2 clusters. IPA is chosen, because this is one of the solvents that is used during development process after DLW, therefore it does not damage the structure.

46

A pulse propagating in the waveguide loses some fraction of its energy per unit length. This amount depends on the density of the scattering particles on the surface of the structure. Firstly, we perform a test on the single mode waveguide studied in the beginning of this chapter. The substrate with the device is prepared to study using drop-casting of the suspension.

Despite the fact that distribution of the particles turned out to be significantly dense and cause serious power attenuation inside the waveguide, the change of the effective refractive index is below sensitivity of the apparatus thus leading to nearly the same time-resolved transmission trace. Figure 25 depicts time-resolved traces of the same waveguide with presence and absence of scattering particles. Although the peak of transmission is suppressed by several orders of magnitude, it is still clear that its position is not changed (or the sensitivity of the technique is not sufficient to detect this kind of a change). However, continuous line without any well pronounced peaks tells that emission is rather evenly distributed along the waveguide.

Recording the time-frames with CCD camera we can track the evolution of the pulse inside the structure (Figure 27). Due to polarization depending nature of the detection mechanism (up-conversion through the non-linear crystal requires two linear polarized beams), the pulse is not visible at the first part of the waveguide (Figure 27-a), which is, however, not a limitation of the technique, since detection of the pulse can be easily performed rotating the sample at 90 degrees. It should be noted, that a big $\approx150\mu$m-sized reflection near the curve of the waveguide is nothing more than a parasitic specular reflection caused by not perfect perpendicularity of the incident beam with respect to the substrate and by clustering of nanoparticles that is rather difficult to avoid.
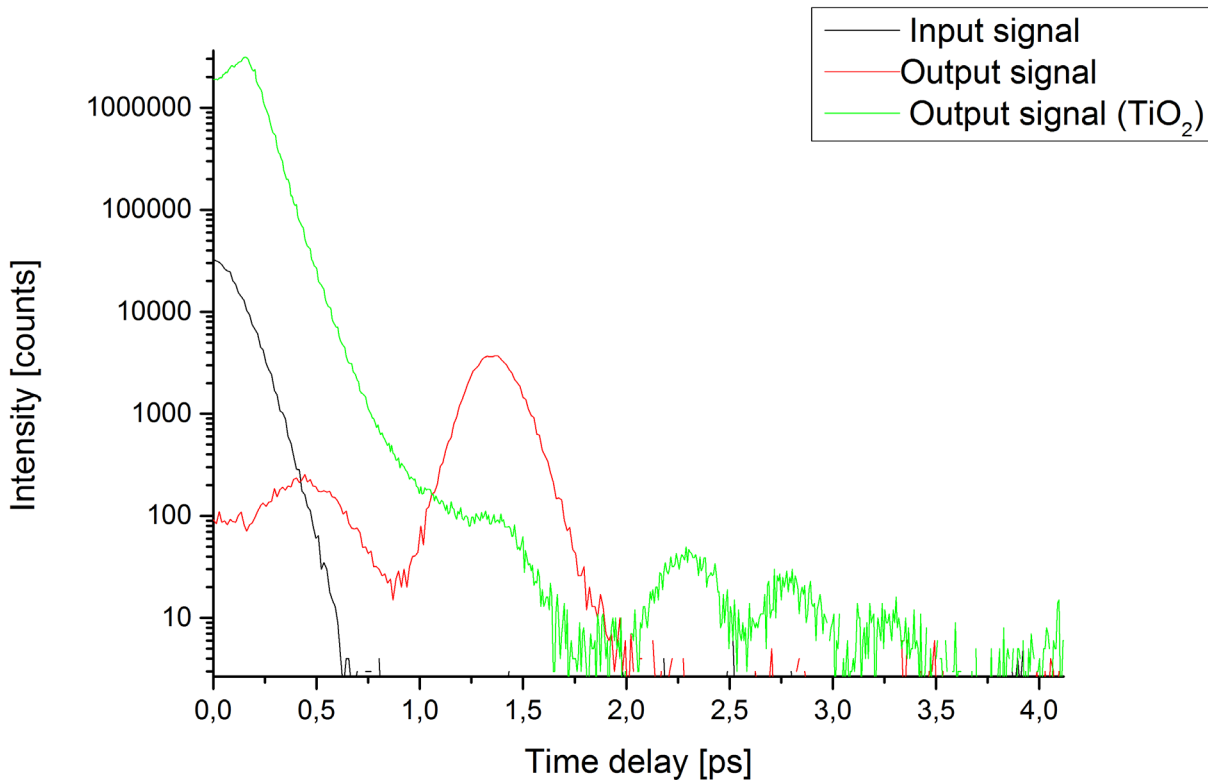
Figure 25. Comparison of time-resolved transmission profiles for a waveguide (*red*) and the same waveguide covered with TiO₂ nanoparticles (*green*).

It should be noted, that since intensity decays rapidly with presence of scattering particles, for the sake of clearness, we had to gradually increase the exposure time of signal acquisition.

As we are proposing a protocol that, in principle, might be used as a tool for non-invasive control for mass-production facilities, the protocol must preserve the sample and should leave all the important characteristics as they were before the analysis. For this purpose, we developed and tested also the way to remove scattering particles. The whole substrate with sample covered with particles is put into an IPA and sonicated for 1 min. This procedure allows to completely remove all the particles and their clusters even from the narrow and hard-accessed regions like dips in the grating coupler.

48
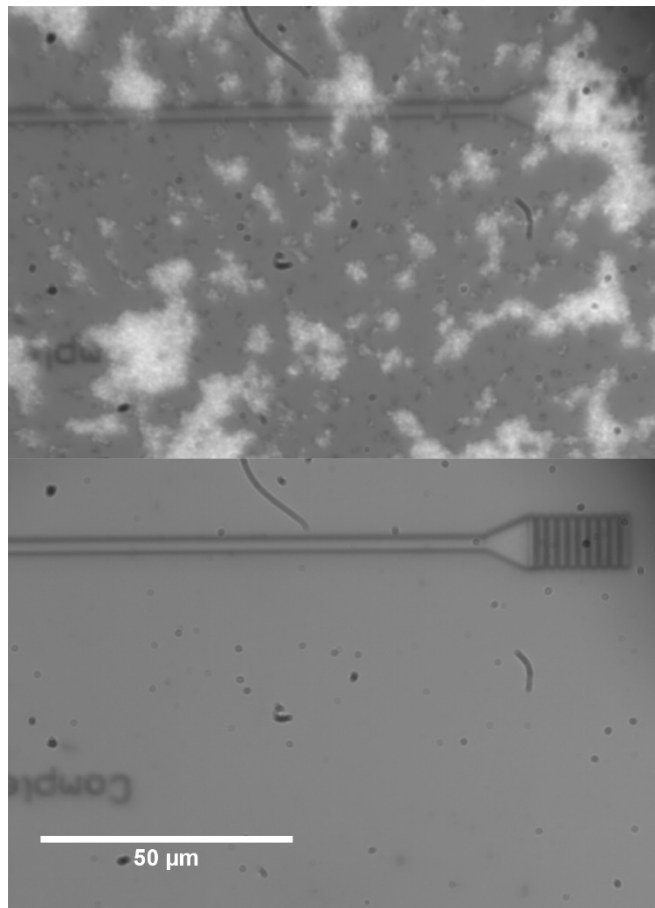
Figure 26. Waveguide and grating output coupler before and after sonication in IPA. The figure shows that nanoparticles can be easily removed form the strucutre.

Figure 27 proves the concept of the imaging for a waveguide, but much more attractive object to study is a ring resonator from the previous subsection. Using Figure 22 as an evidence of the coupling we prepared a sample for a time-resolved imaging measurement using the same suspension described above and acquiring time frames showing pulse propagation in the structure. Looking at the time frames one can easily track the dynamic of the pulse inside the structure – in the beginning pulse reaches the resonator and leave part of the energy inside the ring and then couples out through the grating coupler. Part of the pulse remaining inside the ring starts to circulating and the injecting part of its energy into the bus waveguide at each roundtrip. One can see the light inside the ring, however, due to exponential nature of energy decay the detected intensity is orders of magnitude smaller at each roundtrip that leads to exponential increase of acquisition time while measurements.
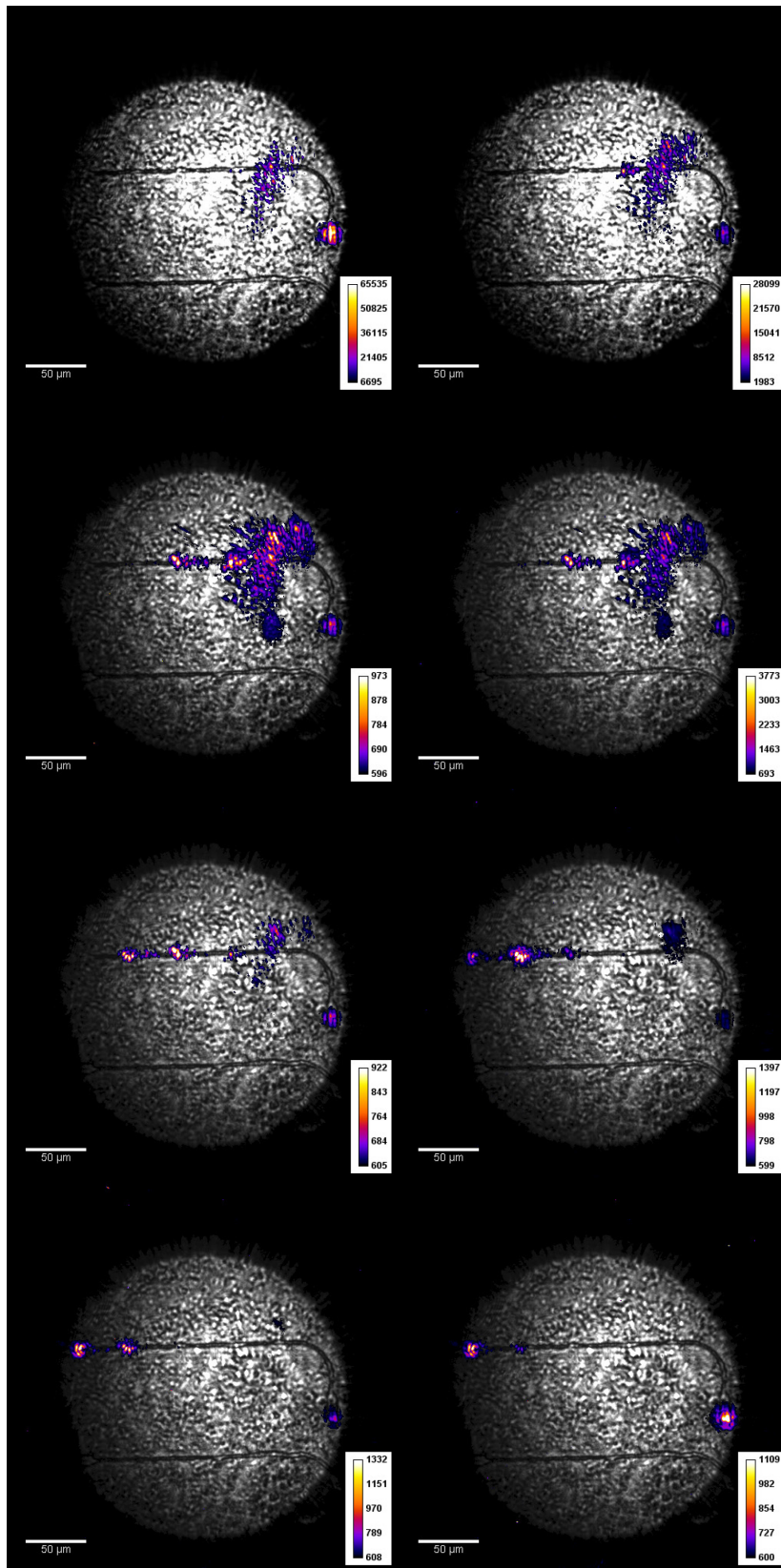
Figure 27. Pulse propagation inside polymeric waveguide. The pulse impinges in the grating coupler on the right, then a parasitic scattering takes place. After that pulse reaches first, then second defect and couples out through the grating coupler. Time difference between the frames Δt=0.275 ps.
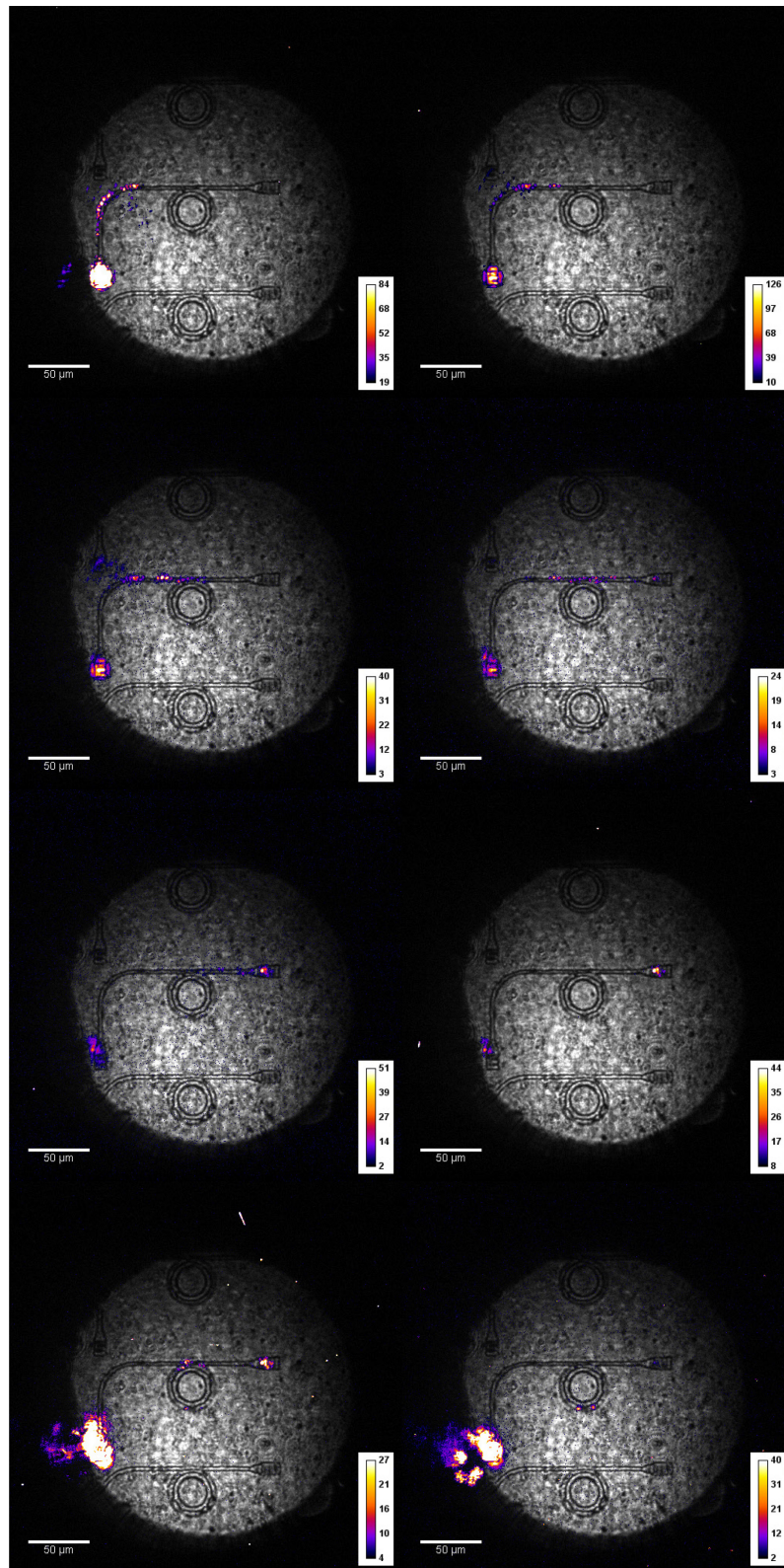
Figure 28. Time-resolved imaging of laser pulse propagating inside whispering gallery mode resonator and a waveguide. Pulse enters the assembly trough the gratin coupler at lower left (in last images overexposure of the tail of the pulse in grating coupler takes place leading to big bright region). Then light propagates and couples into the ring – this is evident due to several scattering point inside on the image of the ring (Δt=0.275 ps).

51

To underline the most important part of this experiment and for the sake of clarity and visibility we plot the detected signal from the ring (one time-frame) on a separate image using different look-up table and not overlapping it with background image (Figure 29).
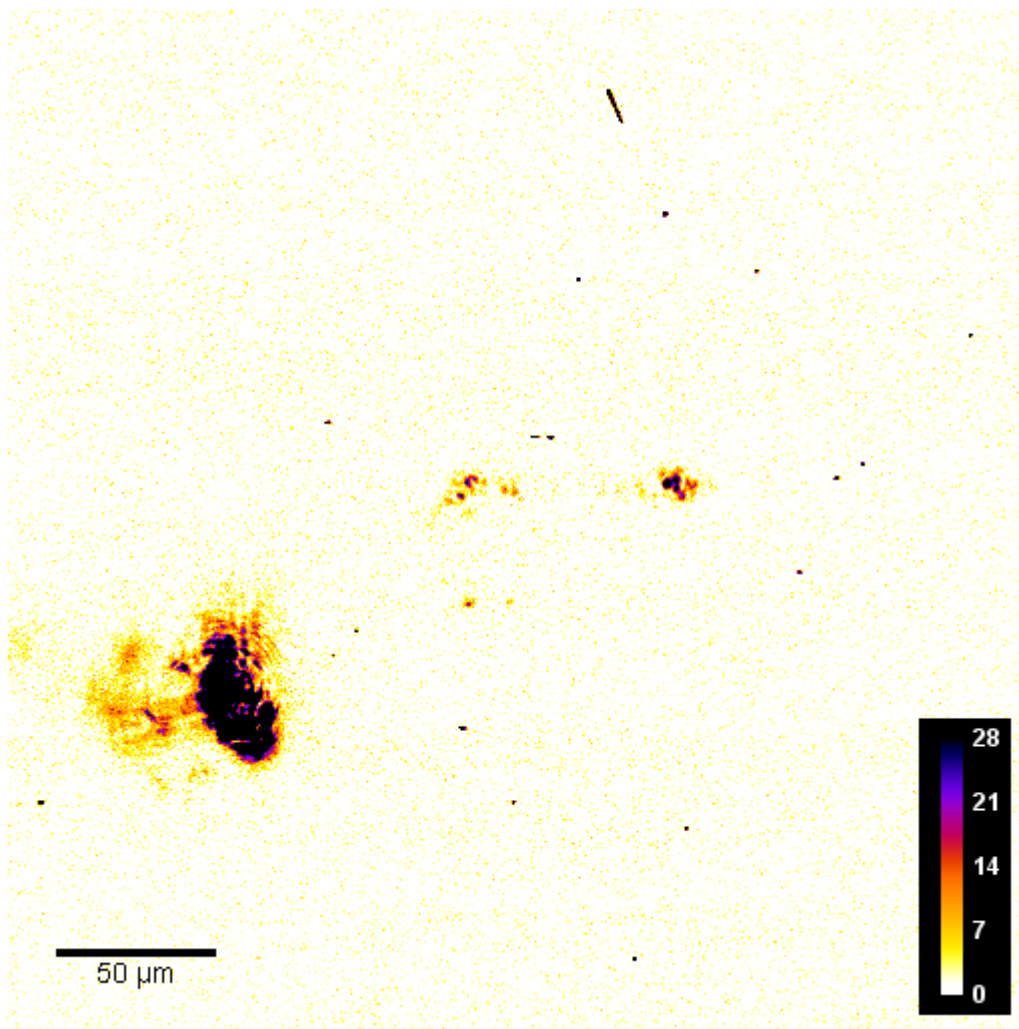
Figure 29. Inverted color table for the signal from signal from WGM resonator. Overexposed region corresponds to the input coupler, while light from the ring is shown in the center of the image (dots on the lower and upper part of the ring). The ring is coupled vertically to the waveguide.

In Figure 29 we see how part of the pulse couples out of the ring into the waveguide while the remaining part continues circulating inside the ring. The discontinuity of the pulse appearing on the left side of the ring is caused by an uneven distribution of the particles and polarization sensitive detection mechanism.

52

At last we should note that in order to increase the quality of the images, we propose to repeat the cycle of particle deposition and imaging several times, combining the output images into one. This will let decrease the effect of uneven particle distribution and lead to better quality of images.

2.8 Complex photonic circuits fabricated with EBL

In order to extend the demonstration of capabilities of the technique described, we designed several structures (arrays of WGM resonators, mutually coupled WGM disks coupled to a branching waveguide) to be studied with time-resolved imaging apparatus. Since DLW in the modification that we can use is not suitable for big structure fabrication, the EBL approach is chosen.

A combination of lift-off resist (LOR) layer (4µm) and PMMA layer (2.2 µm) is fabricated on silica glass to build the structures shown in Figure 30. Design of the complex strucutures for EBL

a)

40 µm

b)

40 µm
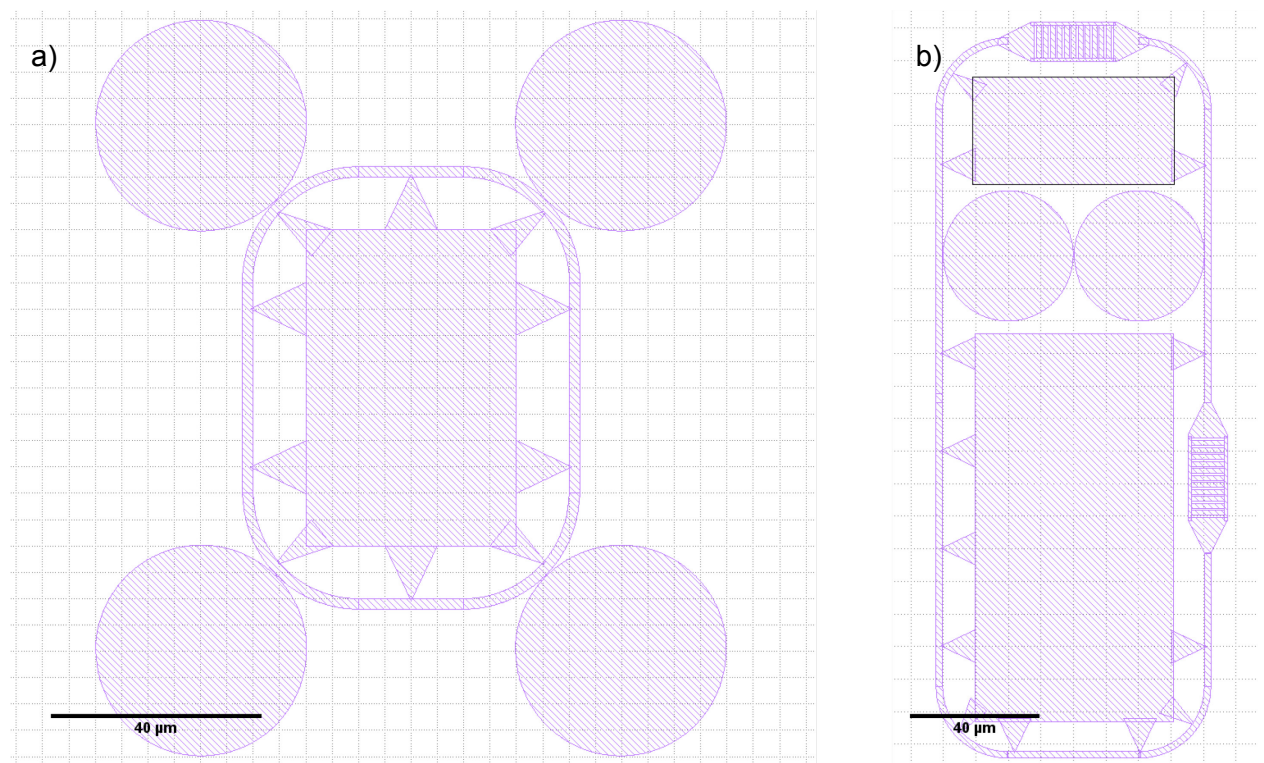
Figure 30. Design of the complex strucutures for EBL.

Those exemplary complex structures allow to demonstrate the capabilities of the technique, because with static-only or time-only measurements the dynamics of the pulse propagation is not easy to reveal, while using imaging resolved in time the ambiguity is removed. All the structures are based on the coupled WGM microdisks. The bulky structures in the middle of the circular waveguides serve as waveguide holding scaffolds. The necessity for that kind of structures consequence of the sample fabrication procedure. When exposed PMMA is already developed, the under-etching of LOR is performed. The under-etching starts with the same velocity at all the edges of the structures. In this case to obtain 2-3 μm of the rim of the disk (so the mode will not be affected significantly by a pedestal to be suspended in the air not being in contact with LOR, since LOR has higher refractive index than PMMA) the under-etching will completely remove LOR layer below the waveguide, making it suspended structure. In this case the waveguide holder is a crucial part of the structure. In our structures the inner bulky part is under-etched, but this, however, doesn't affect the stability of the structure. On the other hand, the second holding point is a taper of the waveguide, where the pedestal is not removed completely.

Unfortunately, fabrication of polymeric structures on transparent non-conductive glass encounters several problems, for instance the charge accumulation and interface correction.

The proximity effect [48] requires a calibration of the dose, gap sizes for a particular thickness of layers, turning the fabrication into an iterative time-consuming process. While the conductivity problem is well known and can be removed by coating with ITO, it yet does not lead to good structures. Figure 31 depicts the typical example of EBL fabricated PMMA on LOR microdisks for photonic applications.
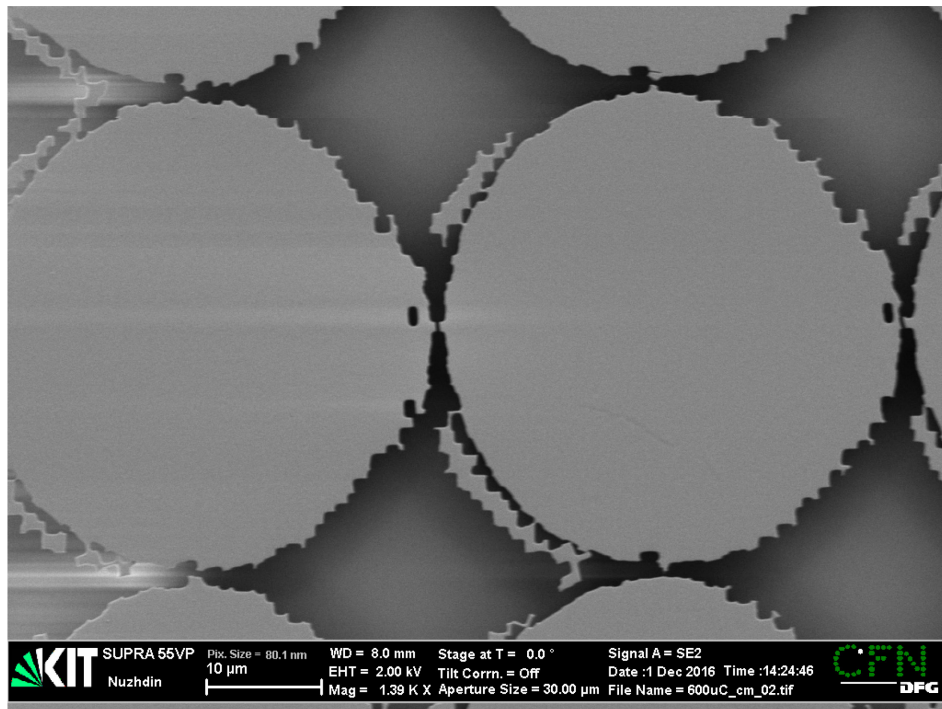
Figure 31. SEM image of PMMA microdisks on LOR pedestals, fabricated with e-beam lithography.

During optimization process it has been discovered that the defects shown in Figure 31 are caused by inability of a system to perform an automatic interface correction process due to a complete transparency of the substrates with polymer layers. The only possible option to overcome this technological limitation is to deposit a thin (≈30 nm) layer of non-transparent metal (in our case chromium), perform an exposure and eventually remove the metal by etching agent. Figure 32 depicts some of the elements belonging to described structures. Despite of the imperfections such as breaking of PMMA (Figure 32-a), collapse of the gratings (Figure 32-c), under-development of LOR (Figure 32-d) and collapse of the waveguide (Figure 32-f), the optimization steps reduce the amount of imperfections at each interaction of the fabrication cycle (to the moment of publication of the current work all the mentioned problems have been corrected on the level of the design, but, however, the actual realization of the structures was not complete – the EBL is performed in Eggenstein-Leopoldshafen (Germany), while the rest is done at LENS (Italy)).
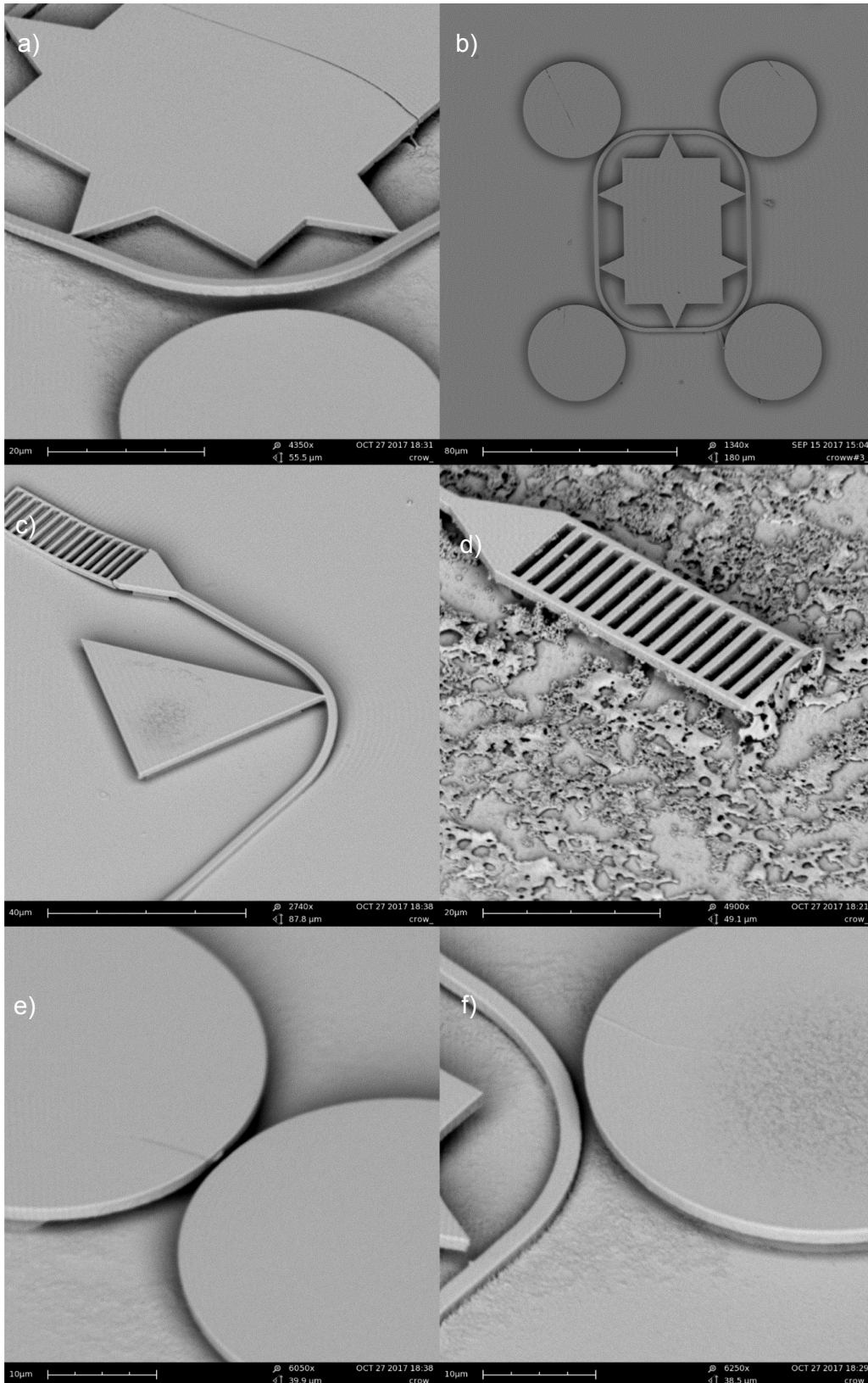
Figure 32. The details of EBL fabricated double layer polymeric structures. The experienced issues:breaking of PMMA (a), collapse of the gratings (c), under-development of LOR (d) and collapse of the waveguide (f).

2.9   Conclusion

In the present chapter we introduced a new way to test integrated photonic circuits. Based on this idea an apparatus was built and characterized. Several examples of application of the technique was described in detail using linear and non-linear elements. At last a protocol for imaging of pulse propagation inside complex photonic circuits is proposed.

To our knowledge, the presented technique overcomes most of the approaches used to extract the same parameters of photonic systems. The most important advantages of our technique are:

- High temporal resolution
- Spatial resolution close to that of optical imaging in visible regime
- The technique relies on far-field detection (unlike SNOM[57] or PSTM [66])
- Wide field imaging – does not require scanning process (unlike [57], [58], [67], [68])
- No special requirements for a substrate and material of photonic circuits (unlike [58])
- Visualization of the signal is preformed directly by optical imaging, not reconstructing signal from transmission suppression
- Apart from TiO_2 -assisted imaging, the technique is non-perturbing
- The spectral information can be accessed a by tuning the probe wavelength which, however, is a sequential procedure

Concluding the list above we claim that the proposed method combines advantages of the other available characterization overcoming several of the previously reported limitation.

However, applications of the technique are not limited to the described systems. A recent work of *Shen et al.* [69] describes how photonic circuits can be employed in the building all-optical neural networks. Although the system is based on finely adjusted interconnected Mach-Zehnder interferometers (Figure 33), the non-linear components could be included in the network in order to introduce some other functionality making it interesting to study time evolution of the light in the network.
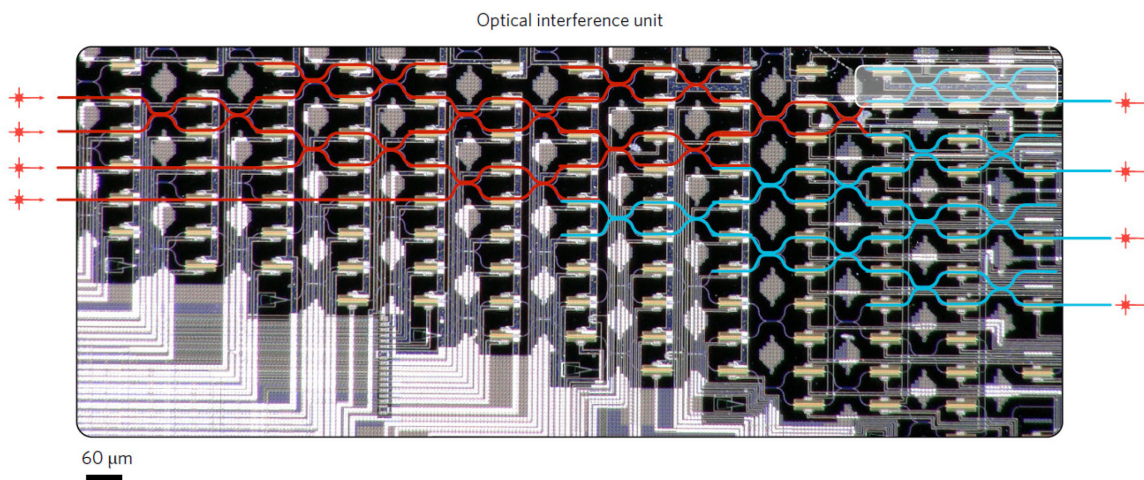

Figure 33. All optical neural network, based on Mach-Zehnder interferometers (adapted from [69]).

Another interesting system to scrutinize are ring resonator based photonic insulator structures. Arrays of coupled ring resonators with carefully engineered gaps and properly designed shapes and lengths might exhibit some peculiar properties not common for photonic structures[16], [70]–[75].

58
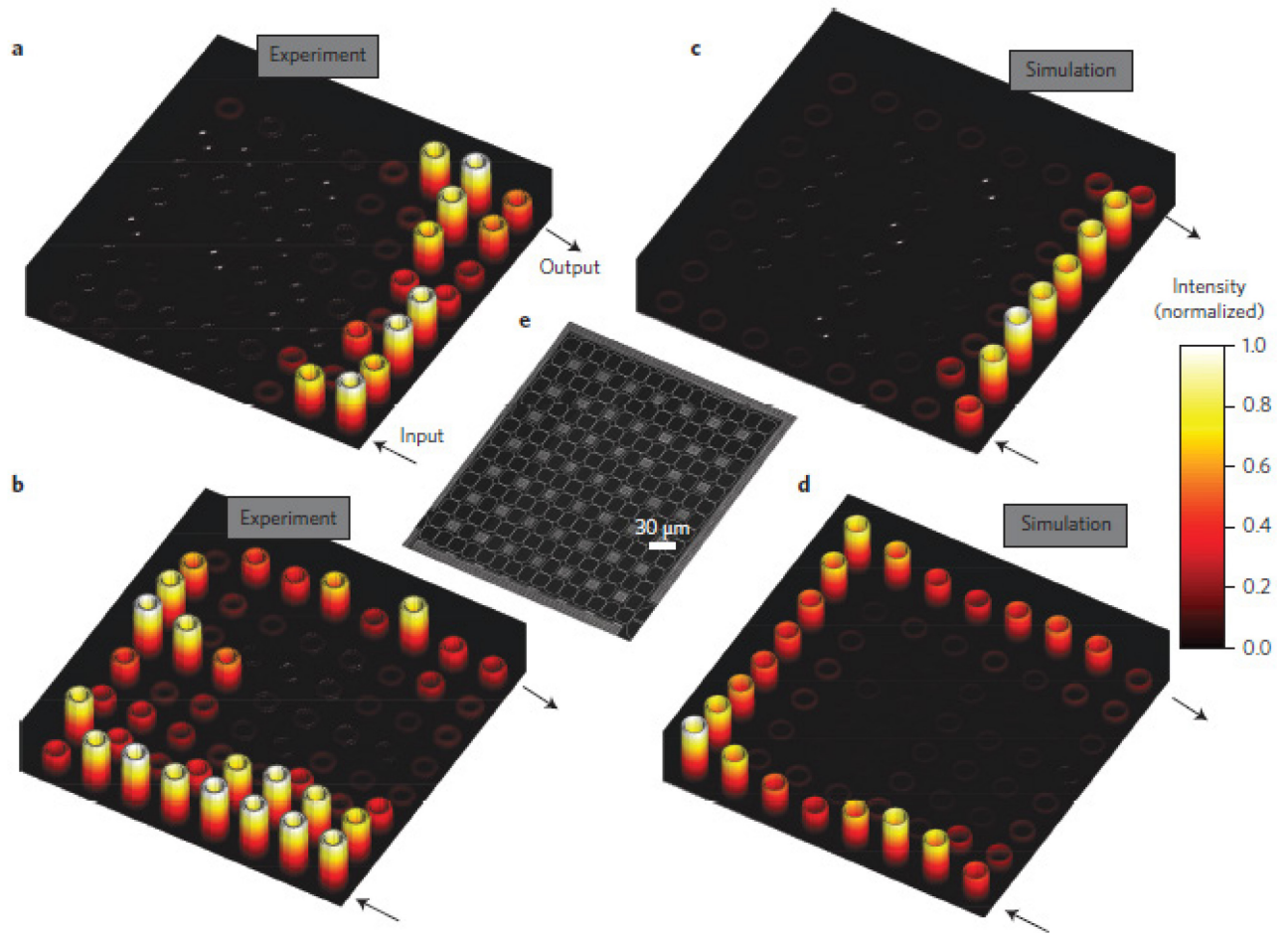
Figure 34. Edge state propagation in a homogeneous magnetic field (8x8array). a–d, Light enters from one corner and exits from the other. The experiment shows that, depending on input frequency, the light takes the short edge (a) or the long edge (b). The experimental results (a,b) are in good agreement with the simulation results (c,d). e, SEM image of the system (Adapted from [16]).

In this case each ring resonator with photons circulating in it mimics a cyclotron orbit of electrons for the case of quantum Hall effect[76], [77]. Therefore, the ring resonators play the role of magnetic field for the case of chargeless photons. Time-resolved transmission combined with the time-resolved imaging can reveal interesting features of light propagation in edge mode.

Paper related to this chapter: D. Nuzhdin, S. Nocentini, L. Pattelli and D. Wiersma "Complex spatio-temporal characterization of integrated photonic components", 2018 In preparation

3 Basics of Liquid Crystalline Networks (LCNs)

3.1 What is LCN?

Liquid Crystalline Networks (LCNs) are one of many smart materials, that are able to perform shape change under external stimuli, such as light [78], electricity [79], ph-value [80], humidity [81], etc. In fact, this name covers a huge class of substances composed of various molecules. These materials combine properties both of polymer matrix, such its as solid and elastic nature, and that of liquid crystals(LC), implying molecular ordering. The Young's modulus of LCN commonly lies in a range of some hundred kilopascal (kPa) or below (in the temperature above glass transition T_g and below the isotropic temperature T_c). Such softness leads to huge shape changing abilities (40-400%) [82], [83]. Large deformability gives exceptional benefit to external stimulated actuation, and also the realization of remotely controlled micro robotic systems [84].

The main component of LCN is a liquid crystal monomer that bring to the systems properties of LC and the presence of a second monomer with two functional groups that allows to cross-link the systems within polymerization process. Several alignment techniques, e.g. electric/magnetic field [85], [86], stretching [87], surface treatment [88], allow to achieve different LC alignments. After the alignment control inside LC glass cell, a polymerization process is applied to solidify the structure and build up the entire LCN polymeric network.

Doping LCN with photo sensitive dyes gives access to light controllable deformation, due to the light induced disordering in the orientated network. Isomerization and light induced heat are the two main pathways to approach light controlled deformation in LCN[89]. Depending on the diverse shape and alignment distribution, various properties of material can be obtained. A lot of approaches have been proposed for light controlled robotic application based on LCN light driven

60

components. Of particular interest is work by *K.Kumar et al.* [90], where they demonstrate the ability of LCN film to oscillate under direct sunlight.

3.1.1 Application of LCNs to robotic systems

Within past years a field of LCN applications to robotic systems has been growing, reaching a number of milestones. Starting from simple actuators, various structures like micro-walker [37], micro-swimmer [91], caterpillar [92], [93] robots and even an artificial eye [94] have been demonstrated.

As a result of variety of fabrication techniques, a diversity of actuation mechanisms, the application of such devices grows quickly. Recently, the biocompatibility of LCN materials has been proven opening to bio applications up to regenerative medicine [95].

3.2 LC Monomer Mixture

Despite of the existence of numerous molecules to be used in LCN, all the experiments in the present work exploited a single monomeric mixture composition, varying only a dye (see 3.2). The mixture based on *nematic* LC mesogens (Figure 35), purchased from SYNTHON Chemicals GmbH & Co. (M2). Nematic liquid crystals are characterized by a uniaxial alignment along one preferential direction defined by their director. It has a liquid crystal to isotropic phase transition temperature T_g at 54 °C. Crosslinker CL5 (SYNTHON Chemicals) has a nematic phase between 63 °C to 130 °C [84]. Photo initiator (IN1) is responsible for starting radical polymerization when absorbing a UV photon. At last an azo-dye (D6) is added to the mixture for light responsive activation of final polymeric structures. This dye was developed by chemists of the group to be compatible with direct laser writing, based on 2-photon absorption process (transparency window above 700 nm and around 390 nm in correspondence of the two photon absorption window) [96]. All the monomers are engineered with acrylate moiety for the purpose of crosslinking under polymerization.

The exact proportion of the mixture components might vary, consequently changing the polymer properties. For instance, an increase of amount of cross-linker leads to decrease of maximal deformation and to rise of values of generated forces.
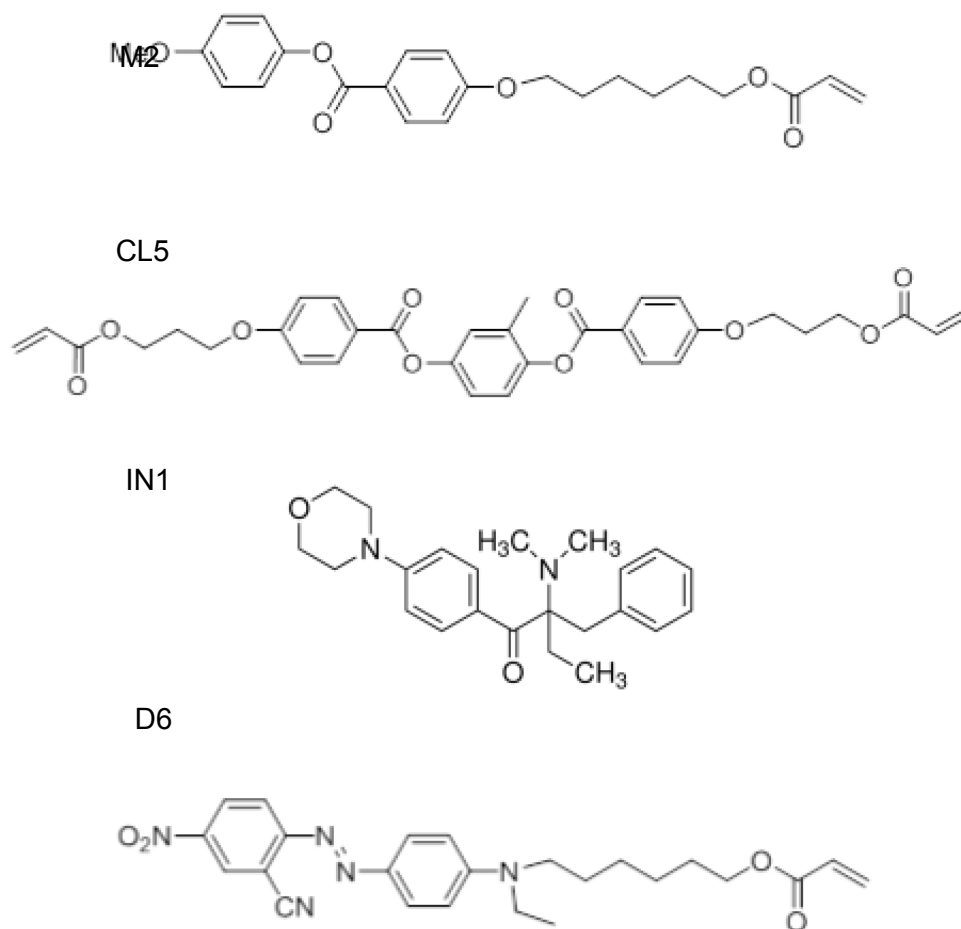

Figure 35. Molecules used for LCNs.

However, only one composition of the mixture, which has proven its applicability in number of works[37], [42], is used in current work: 78% $_{mol}$ of M2, 20%$_{mol}$ of CL5, 1%$_{mol}$ of IN1 and 1%$_{mol}$ of a dye (usually D6).

The polymerization and crosslinking process start from the photoinitiator: after absorbing a UV photon (or by two-photon absorption), one initiator splits into two parts where each part carries an activated electron. Such electron triggers the acrylate group to start the chain polymerization process. Mesogens, crosslinkers start to chemically link to each other forming an entire complex rigid network. Thus, we

62

fabricate a solidified structure, in which the original alignment has been conserved in the elastomer network.

3.3   LCN sample preparation

Sample preparation procedure is the same for direct laser writing of the LCN structures or for preparation of macroscopic films.All the samples prepared with use of glass cell – two glass microscope coverslips are covered with one of the polymers used for alignment of liquid crystals: PVA (Sigma-Aldrich) or polyamide (PI 130, PI 1211) (Nissan Chemical Industries, Ltd.). Different spacers, usually glass spheres with diameter ranging from 2µm to 200 µm, are put between the glass substrates to precisely control the thickness of the structure. The next step is an infiltration of a monomer mixture inside the cell that is done on a hotplate with a temperature set above nematic-isotropic phase transition temperature. And finally, the sample is slowly (in order to achieve single domain alignment) cooled down to nematic state and LC molecules align according to coating of the glass. Alignment of LC is a crucial point for achieving various types of movement of LCN structures.

3.3.1   Uniaxial alignment

Two glass substrates are spin-coated with PI 130 or PVA and rubbed by a satin in a unique direction. Then the cell is assembled using spacers. As a result of the surface anchoring effect, LC molecules with long rod shapes are trapped into the nanoscale grooves on a surface of the rubbed layer, and, therefore, orient along the rubbing direction. The molecular interaction induces uniaxial alignment within some thickness of monomer mixture. In some cases, we choose PVA coating for one glass slide and PI 130 for the other glass. Though rubbed PI 130 and PVA layers have the same aligning properties, the hydrophobic nature of PVA makes it less sticky to LCN structure compared to PI 130. Thus, all the fabricated LCN structures are attached on the PI 130 substrate, this provides convenience for sample transfer.

3.3.2 Twisted alignment

Two rubbed glass substrates with PVA/PI 130 may not be aligned in the same direction, but rotated with respect to each other by some angle. Surface anchoring induces LC alignment only within the region close to the surface. Between two rubbing layers, LC monomers automatically twist, trying to find minimum energy state being aligned in different directions close to two glass surfaces.

3.3.3 Splayed alignment

Hydrophobic PI 1211 coating is applied to orientate LC molecule perpendicularly to the substrate surface. With two PI 1211 coating, the cell induces homeotropic alignment, as shown in Figure 2.3.1 (b). Commonly, PI 1211 layer is combined with another type of coating layer (PI 130 or PVA), to induce a 90° homeotropically rotating alignment throughout the sample.
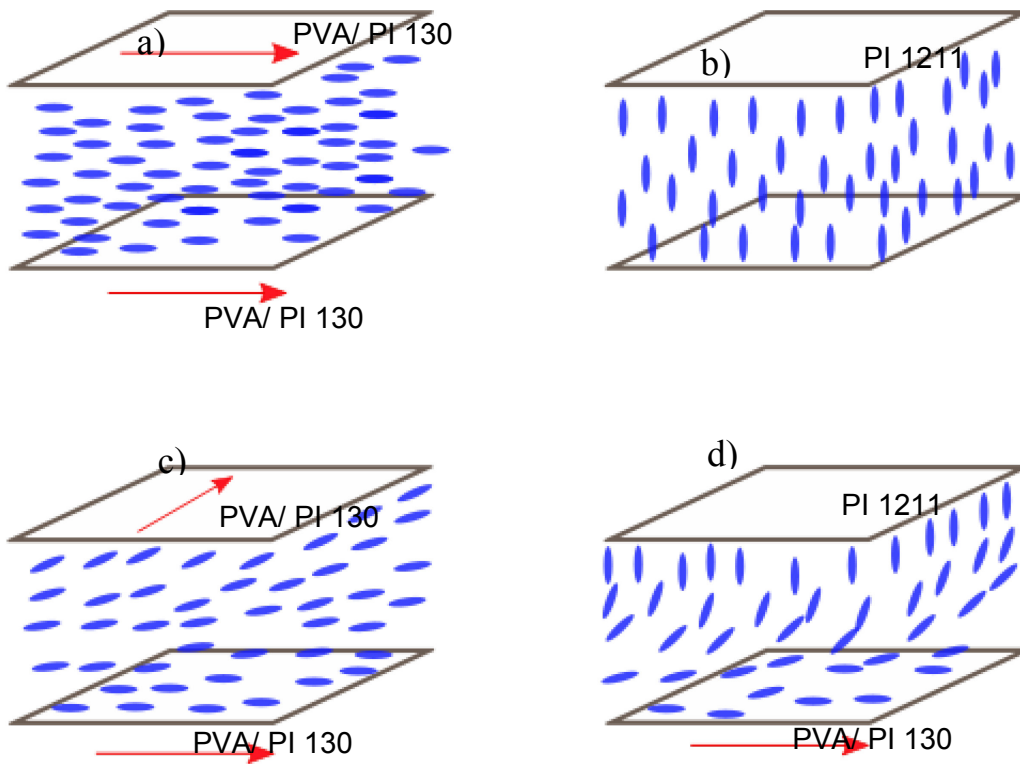
Figure 36. Alignment of LC in a cell.

When a glass cell is ready, the last step of structure preparation is polymerization that is done either by UV lamp (case of macroscopic films) or by 2-photon absorption (case of DLW).

3.4 Actuation of LCN structure

Regardless the type of fabrication procedure, e.g. micro structural fabrication with use of DLW or macroscopic film polymerization, the actuation mechanism for reported LCN remains the same.

The root of the shape-change of LCN lies in the destruction of orientational order of LC inside polymer matrix. When a stimulus applied, it leads to the molecular reorientation and contraction along the alignment direction and expansion in the perpendicular direction. In most of the cases the volume is considered to be constant while deformation. The azo-dyes are famous for their ability to exist in two forms (stable and metastable form [97]), that could be switched by absorbing a photon of a particular wavelength (*photo-isomerization*). However, in our case, the molecular reorientation is considered to be an effect of thermally induced phase-transition.

Depending on the initial alignment of LC mesogens in the polymer matrix various movements can be achieved. Uniaxial alignment leads to a homogeneous contraction along the alignment direction[98].

a)   b)

Laser off   Laser on
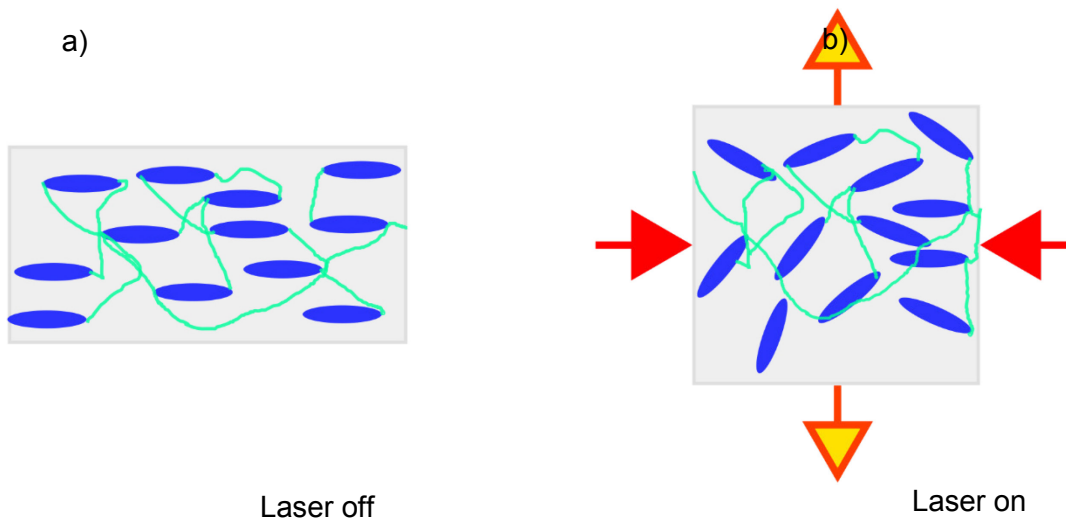
Figure 37. A mechanism behind contractionof LCNs.

For the case of splayed alignment, the resulting structure is capable of bending[99]. The maximal bending angle depends on length and thickness of structure, while a force generated is, of course, depends on the mass of the structure or, in other words, on amount of matter experiencing phase transition.

Laser off   Laser on
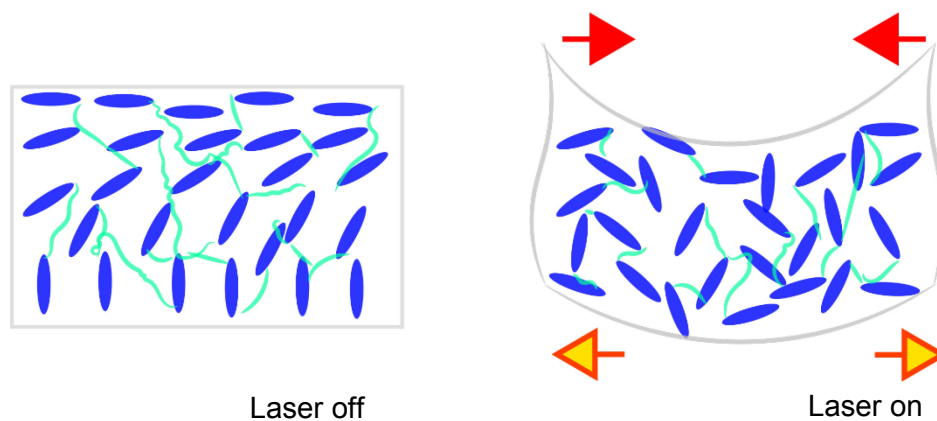
Figure 38. A mechanism behind bending of LCNs.

In the next two chapters we exploit some of the opportunities that described mechanisms give us.

4   Light activated micro gripper

The ability to grab and manipulate objects is one of the basic functions of human hands whereas object handling becomes rarer in microscopic living creatures. Mimicking such functionality is a fundamental task in robotics, and it represents a great challenge especially at the microscale [100]. Additionally, very appealing feature is the remote control of micro-actuators that could be used to enlarge the functionalities of lab-on-chip microfluidic devices, and even for non-invasive surgery and diagnostics[101].

The same materials would also consent to add more functionalities to the structures, such as the self-activation in specific conditions. In this chapter, we exploit nature Liquid Crystalline Networks to prepare the smallest light-fueled microgripper sensitive to the local environment and able to capture microscopic objects. The peculiar novelties, together with its dimensions, are the possibility to remotely control it and its ability to self-activate in response to the presence of an absorptive medium in the gripper proximity. We herein demonstrate grabbing of small objects at the microscale thanks to a soft elastic robotic hand powered and controlled by light.

4.1   System concept

The easiest design for a microgripper is constituted of two different fingers able to bend towards the same point allowing to catch an object between them[102]. To achieve a more stable grip of an object, we design more complex structure that is able to perform an out-of-plane movement that is composed by four opposite arms[103] (Figure 39). To obtain bending elements we use a procedure described in previous chapter (page 65).

Despite other smart materials (e.g. hydrogel), the shape-change behavior is an intrinsic property of the used polymer and does not require a specific environment leading to the applicability of LCN actuators in air or in a liquid. Exploiting the LCN properties we implemented the basic operations enabled by the human hand, such as grabbing and moving an object, functionalizing a light-remotely-driven robotic gripper at the microscale.
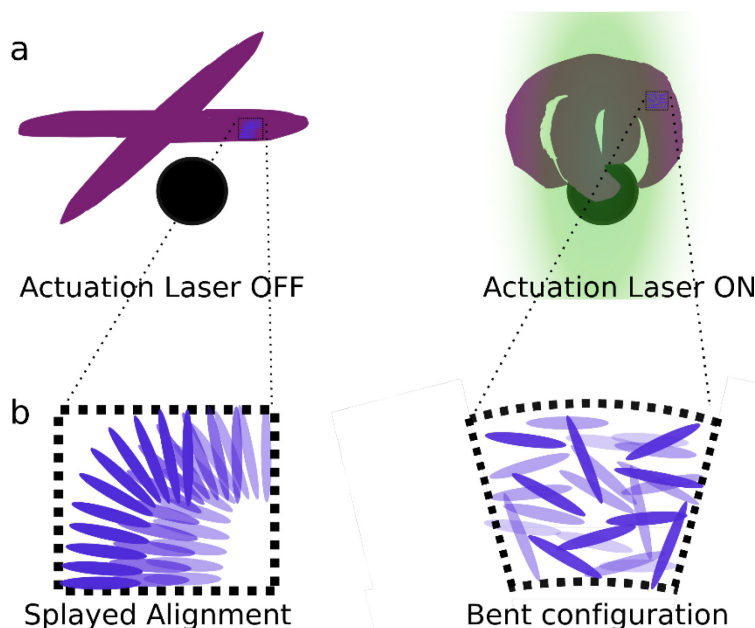
Figure 39. Design concept of micro gripper.

4.2   Fabrication

To design a first gripper geometry, inspiration was taken from the hand structure. To achieve a complete bending of each gripper arm, rigid elements were used to connect LCN blocks as phalanges in between knuckles (Figure 40-a). In a second attempt, we simplified the fabrication procedure by the introduction of simple arms composed only of a monolithic LCN stripes (Figure 40-b). In both cases, we succeeded to assemble the prototype structures at the truly micrometric scale using DLW. The splayed molecule orientation was obtained using glass as described in before (3.3).
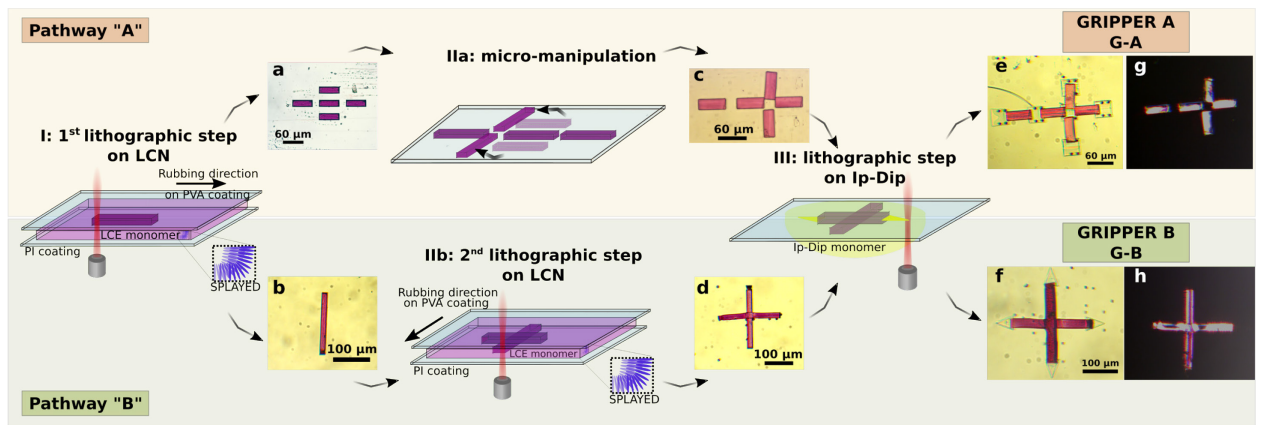
68

Figure 40. Description of a fabrication process. Optical images (a-f) of the developed structures. For the final structures, POM images of the two grippers are shown (g-h).

4.2.1 Gripper A

A commercial negative photoresist (Ip-Dip, NanoScribe GmbH) was used as rigid polymer to create the stiff body elements. Within the first fabrication approach (Figure 40. Description of a fabrication process. Optical images (a-f) of the developed structures. For the final structures, POM images of the two grippers are shown (g-h).Figure 40 - **a**), the structure, named here as "*Gripper A (G-A)*", was composed by robotic arms consisting in LCN blocks (20 x 60 x 20 μm^3) connected by Ip-Dip structures (40 x 40 x 2 μm^3). G-A was designed to have three short *fingers* (with passive-active-passive blocks) and one long *finger* in order to facilitate the possible holding of an external object. To prepare this structure, only two lithographic steps were needed. Simultaneous fabrication of all the LCN structures was performed, followed by block positioning, which was achieved by mechanical reorientation of two blocks on the glass substrate. This micro-manipulation (4.3) step allowed to achieve the desired position of the light-responsive parts of the structure and, consequently the requested functional deformation of the final gripper. At the last lithographic step, Ip-Dip squares were fabricated between, as connectors, and at the ends of the LCN parts. This rigid terminal parts limit the stickiness of the LCN body when they get in contact during bending and allow the correct recovery

of the initial configuration and a release of trapped object when stimulation is interrupted.

4.2.2 Gripper B

However, picking up the blocks from the glass substrate and exactly positioning them in the right configuration is not a trivial operation. Moreover, the detachment of the structure from the glass might result in deterioration of the grippers, especially in the point where to different materials are connected. For these reasons, we developed the second fabrication strategy, so-called "*Gripper B (G-B)*" (Figure 40-b) through three lithographic steps. First, a stripe ($20 \times 200 \times 20 \ \mu m^3$) of LCN is written in a cell with splayed LC orientation. After development in toluene, the first LCN blocks remain attached to the PI coated glass that was subsequently used to build up a second splayed cell where the rubbed PVA coated glass mounted with a perpendicular orientation in respect to the previous cell. The following writing step is performed after infiltration of that second cell with the same LCN mixture. A polymeric structure, having a cross shape in which the four-orthogonal arms bend towards the same point, is obtained. Ultimately, with a third writing step, triangular Ip-Dip structures ($30 \ base \times 40 \times 2 \ \mu m^3$) are added at the arm ends.

Despite one more lithographic step is required, pathway B allows more rapid preparation, avoiding the intermediate time-consuming mechanical manipulation of the LCN blocks, and results in the best fabrication methods for the easy scaling up of the process. Moreover, the presence of less components in the structures in favor of a LCN monolithic cross results in an easier manipulation of the final structures, which can be quickly detached from the substrate without any damage. However, pathway A, considering the possibility to mechanically move single blocks, presents a great potential for the development of more complex folding structures as demonstrated in the next paragraph. We therefore considered both geometries interesting for gripper fabrication, and a complete dynamic characterization of the two designs was performed.

70

4.3 Micromanipulation apparatus

The micromanipulation system is based on a custom made reflective microscope. A 10× objective is mounted on a lens tube placed on a vertically standing optical breadboard. A 730 nm IR LED light source is used for illumination through a non-polarized beam splitter. Reflected image is collected by the same objective and projected on the CCD camera. A diaphragm before the LED source is used to tune the contrast of the image. A continuous solid state 532 nm laser is coupled into the objective by a long pass dichroic mirror (50% transmission and reflection at 567 nm) at the incidence angle of 45°. This dichroic mirror can provide efficient reflection of >98% for the green laser, at the same time gives high transparency for the IR light. A loosely focused laser spot of ~150 μm diameter generates maximum illumination intensity of ~10 W/mm2. A band pass filter at 710 ± 20 nm has been set in front of the camera to further block the laser beam. Laser intensity is controlled by a variable neutral density filter placed in front of the laser aperture, while an optical chopper is used to modulate the laser beam with frequency from 1 Hz up to 5 kHz.

Below the objective, a 3D manual translation stage is used for sample translation. A heating stage installed on the translation stage is used for precise control of temperature in a range from -20 to 120 °C with 0.5 ° C accuracy. Two tapered fiber tips mounted on two manual translation stages have been placed on the left and right side, respectively, near the sample position. Structure micro manipulation can be realized by precisely moving the tips with use of the translation stages. A 3D translation stage with 5 μm precision is sufficient to transfer the micro robot on one substrate, but a three-axis water hydraulic micromanipulator (Narishige Group) with 200 nm precision is necessary for more accurate manipulations.

The described system allows to perform diverse manipulations with microscopic structures that include detachment from a substrate (the most dangerous

operation in terms of possibility to destroy a structure) and positioning of structures in three dimensions (in particular moving the structure in and out the laser spot).

At last, an image collected by the objective can be projected not only on a simple CCD monochrome camera, but also redirected to an ultrafast camera (Photron FASTCAM SA4) that is able to record video sequences with sampling rate up to 10 000 frames per second. This camera allows to record ultrafast processes happening on a scale of milliseconds, for instance, the dynamics of LCN under the laser light.

4.4 Light-induced gripper folding

Irradiation of the grippers with a green laser causes the reversible folding of the structures into a closed shape due to the different alignment directions of each arm (Figure 41 a-b). The LCN blocks present a progressive bending as the temperature increases (as a result of the dye absorption). The movement is generated by different thermal expansion coefficients in the direction parallel and perpendicular to the alignment and, therefore, by the different behavior of the two sides of the splayed LCN[104]. Bending angle, being a function of temperature, directly depends on the intensity of the external stimulus (laser power) and can be controlled in order to manage partial or complete closure of the grippers. The two proposed structures were, therefore, studied under different powers of the green laser to point out the light intensity dependence of the response. A laser modulation (chopped green laser at 10 Hz) has been used to evaluate their time dynamics.

The stimulus intensity is not the only parameter that introduces the possibility to control over the gripper movement, in reality, LCN block dimensions (thickness and length) influence the material deformation and the maximal bending angle. The increasing bending as function of power and the different time responses (both in the contraction and relaxation processes) are not two independent effects. In fact, as the power increases, the bending angle of each single stripe enlarges while

contraction process rapidly speeds up[105]. These two effects contribute to the actuation time (Figure 41 - c) that the structure requires to move to a higher bending angle.

On the contrary, the relaxation time is independent from the power and it is influenced only by the initial position of the contracted block and by the temperature of the local environment. From the collected data, represented in Figure 41 c, the contraction and relaxation times are reported as function of the excitation power. The actuation threshold for G-B (21 mW) results smaller of a factor of two than for G-A (37 mW), and the same behavior is highlighted for the complete gripper closure (90 mW for G-A and 51 mW for G-B). This trend is probably due to the bigger dimensions of G-A and the introduced structure strain by the rigid polymeric phalanges of this design. In both cases, the gripper dynamics is confirmed to happen at the millisecond scale[37] appearing very appealing in robotic application for real time response devices.

The bending time decreases as the light intensity increases while the relaxation time follows the expected trend only for G-A. The faster dynamics (20 ms, time for the complete structure closure) is highlighted for G-A. We supposed this result to depend from the dimensions of the single blocks that compose such gripper, that are smaller than G-B arms. Smaller dimensions reasonably lead to a faster heat diffusion and dissipation for the entire system thus causing a quicker response.
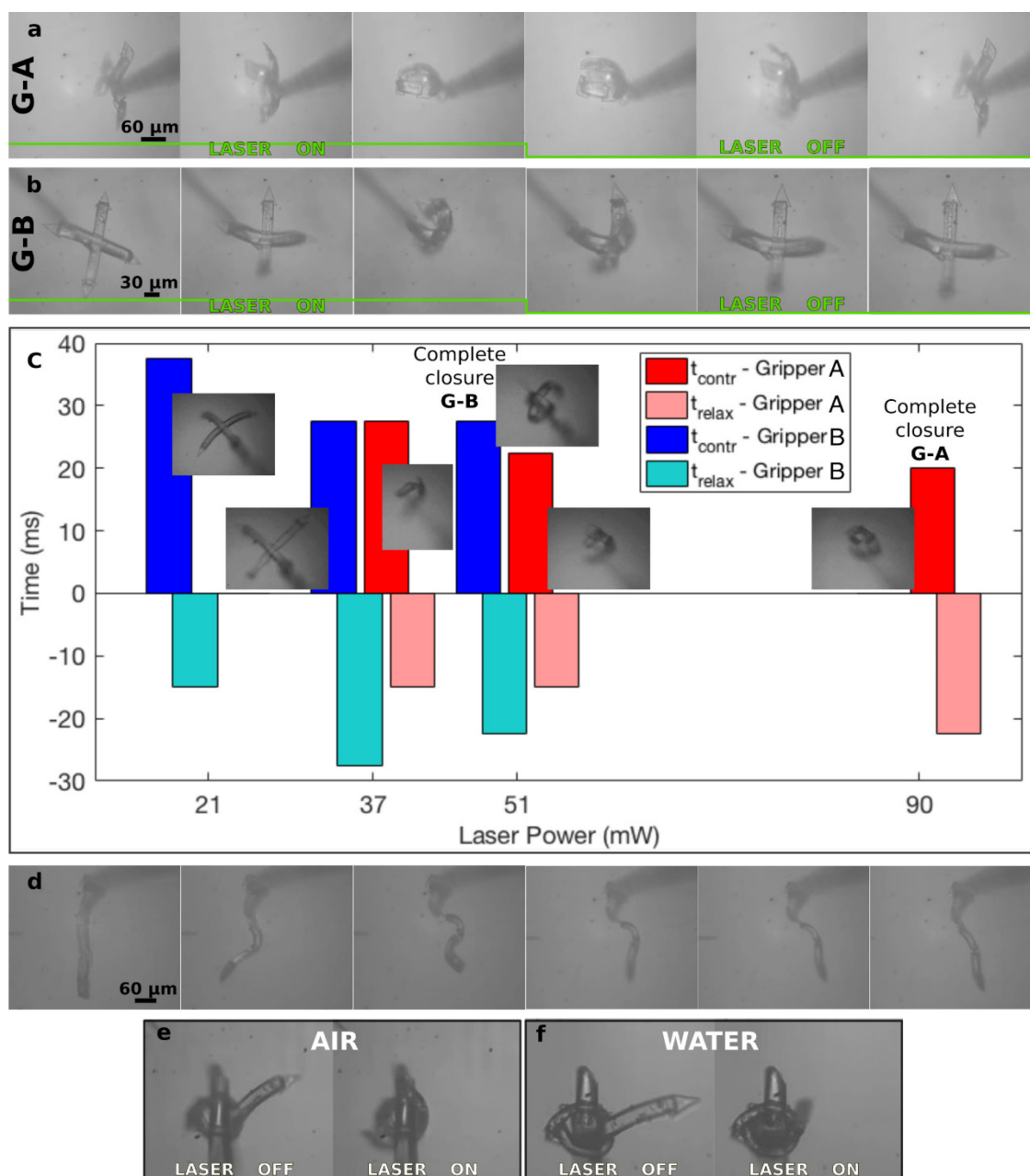
Figure 41. Shape-changing behavior of the two micro-grippers under laser irradiation. a) Movement sequence of G-A and b) of G-B. Once the laser beam is shined on the structure, the gripper started to bend its fingers up to the complete closure. Turning off the excitation, both grippers relaxed towards the starting rest position leading to a perfectly reversible action. c) Times of contraction and relaxation of the two grippers under the power excitation value of 21 mW, 37 mW, 51 mW and 90 mW. The time values have been measured with a fast d) Combination of LCN blocks with different splayed alignments allowed to create a robotic arm showing a diverse movement. The gripper movement was demonstrated in two diverse environments: e) air and f) water.

Taking advantage of a fabrication strategy A versatility, we demonstrated how the mechanical micromanipulation can be exploited to arrange LCN blocks on the

74

glass into a more complex assembly (before the lithographic step involving Ip-Dip). An oscillatory movement can be reproduced by arranging on a line three LCN blocks with alternated splayed alignment, obtained by turning the central block upside down (Figure 41-d) and connecting them with IP-Dip junctions. The resulting structure showed a complex and asymmetric deformation to be further exploited for swimming and crawling at the microscopic scale.

As a proof of concept, we also demonstrated that our microgripper movement is independent from the environment and is capable of operation even in water. The reported G-B structure was firmly attached to the glass fiber thanks to the two opposite arms connected around it, guaranteeing a tight fiber hug during the immersion into water. Evaluation and comparison of the bending is thus possible analyzing the other two arms behaviors in air and in water (Figure 41 e-f). Locally inside the structure, the LC order-disorder transition takes place and the structure deforms in both environments. The higher water thermal conductivity does not prevent the LCN transition although the bending activation power is five times higher than in air, and it is not possible to achieve a complete closure of the gripper arms (Figure 41-f) using similar power values.

Although both prototypes showed an efficient structure closure with comparable millisecond dynamics, but, considering the more complex and time-consuming fabrication and manipulation of G-A, we pursued on the experiment only investigating G-B.

4.5   Catching a microstructure with a gripper

The remote actuation of micro-robots through a light stimulus results in an interesting possibility to drive and control LCN based micro-grippers. By the use of the micromanipulator it is possible to hold the microscopic hand on a tip of a glass fiber in a desired position and, using a flat laser irradiation, to control the gripper closure detaching different micro objects from a support (in our examples another

tip of glass fiber). The laser light, shined over a round area of hundreds of squared microns, modulates the gripper deformation from the bent state (laser on) to the rest state (laser off). In Figure 42, some examples are shown.
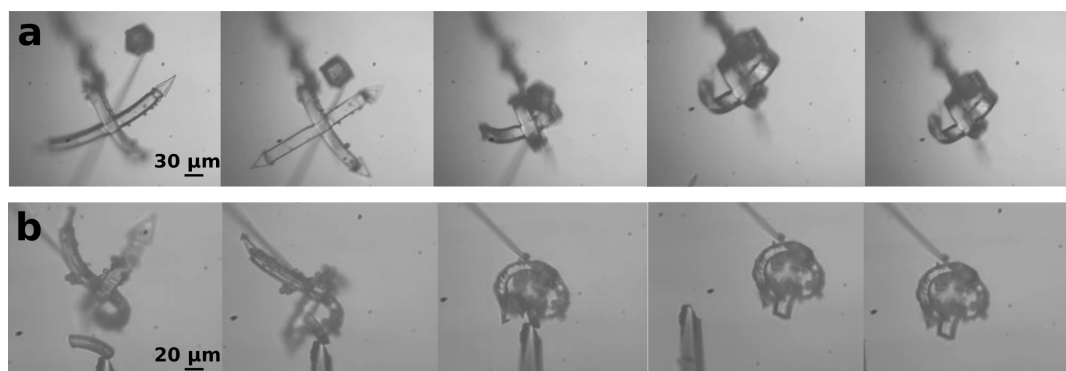
Figure 42. The micro-gripper approaches and catches polymeric block. a) G-B is activated with the green laser and is able to catch and detach the polymeric micro-cube from the fiber tip increasing the activation light up to the complete closure (51 mW). b) The same effect is demonstrated for a LCN block.

The gripper was demonstrated able to detach such blocks (40 x 40 x 20 μm^3 and 20 x 60 x 20 μm^3) from a glass tip (Figure 42 a-b). The gripper was brought into the proximity of the target, and when the laser power was increased to 50 mW the arms closed one toward the other. The cube is thus detached from the fiber and the gripping and holding was performed.

4.6 Autonomous operation of micro gripper

An appealing feature to be exploited is to induce a self-actuation of the gripper, depending on the selected particles to be caught by keeping the activation laser close to the threshold bending power value (25 mW). The different interaction of the target particles with light determines the gripper folding process.

We exploited absorbing and scattering properties of black and white particles to investigate which mechanism can induce a self-activation of the gripper. Considering that particles are able to absorb the working wavelength could increase their temperature under light irradiation and, consequently, release heat in the surrounding environment resulting in an enhanced warming of the gripper.

76

On the contrary, scattering particles deflect light that can enhance the irradiation power on the robot. To verify these effects, we studied the gripper behavior during the approach with carbon nanopowder (Figure 43 a-f), a black material able to absorb a broad wavelength range, and titanium dioxide microparticles (Figure 43 g-h), a well-scattering material.

At first, we verify that there is no interaction between the particles and the gripper (like, for example, electrostatic forces) present when the irradiation was absent.

After proving the absence any possible contribution of attractive interactions, the laser light, able to induce a partial small bending of the gripper arms, was applied (25 mW, Figure 43-b) and kept constant. Approaching the carbon nanoparticles, the gripper is grabbing to the closed form (Figure 43-d).

The closer the particles approach to the gripper, the higher the local temperature becomes allowing the LCN phase transition to occur and therefore the gripper complete closure. On the other hand, the approach of titanium dioxide cluster resulted in a very little change of the gripper shape (Figure 43 g-i) demonstrating as white scattering particles are not effective to modify the gripper state.
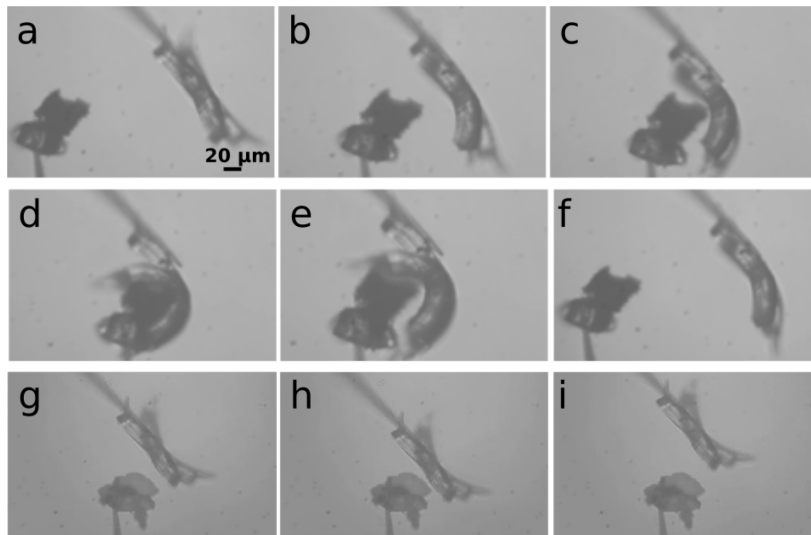
Figure 43. Micro-grippers folding while approaching nanoparticle aggregates. a-f) Sequence of images showing how micro gripper interacts with carbon clusters g-i) Sequence of images during the approaching titanium dioxide particles.

4.7 Conclusions

In this chapter we reported a possible application of LCNs to the field of micro-robotics. Fabricated with state-of-the-art DLW system, light activated micro gripper is not only remotely controlled, but also is capable of autonomous action. The integration of such micro-gripper with other micro robotic devices, such as micro-swimmer, can be envisioned by the currently available fabrication technique and would results in efficient ways for transport objects up to real microsurgery devices.

Papers related to this chapter:

*[1] D. S. Wiersma, sara nocentini, C. Parmeggiani, D. Martella, and **D. Nuzhdin**, "Photonic arms, legs, and skin," in Optical Trapping and Optical Micromanipulation XIV, 2017, vol. 10347, p. 99.*

*[2] D. Martella, S. Nocentini, **D. Nuzhdin**, C. Parmeggiani, and D. S. Wiersma, "Photonic Microhand with Autonomous Action," Adv. Mater., vol. 29, no. 42, p. 1704047, 2017.*

5 LCN as tuning element for photonic devices

5.1 Tunability of photonic components

Photonic integrated circuits that bend, split, couple, and filter light have been demonstrated on different platforms. In most cases, the optical properties of the structures are predetermined by the structure design and, therefore, cannot be modified once fabricated. Switches and modulators have been demonstrated by employing III–V compound materials based on photoexcited free-carrier concentrations resulting from one- or two-photon absorption [94]. In silicon, switching has been shown only by use of extremely high powers [106] in large or nonplanar structures that are inappropriate for effective on-chip integration[107].

Tuning of various parameters of photonic component is of a high demand in modern technology. Having tunable components on chip-scale photonic devices allows to diminish effects of fabrication uncertainties and defects, together with broadening the applicability of the devices. This is a key-feature that is requested both in fundamental physical experiments and in commercial devices. Among the optical elements that have been introduced, tunability is a particularly interesting feature for whispering gallery mode (WGM) resonators and WGM lasers. The other structure that requires intrinsically a dynamic control in its working mechanism is the Mach-Zehnder interferometer [108] that are predominantly driven by an electro-optic effect. Mach-Zehnder interferometers and a delay ring resonator in one of its arms can also be combined in a configuration, the so-called ring loaded Mach-Zender interferometer [109]. This arrangement might serve as an interleaver filter or as an optical filter with a flat response, depending on the length of the ring and the path difference between the upper and lower branches.

Peculiar and attractive features of WGM resonators are the small resonant mode volume and the high quality factors, that hence give rise to sharp spectral

resonances[19]. Numerous attempts have been made to develop an reconfigurable components allowing features as optical modulation [110] and optical bistability [111]. The most common tuning methods are based on electro-optic effect [112], thermo-optic effect [113], [114], free carrier injection (in semiconductors) [110], mechanical deformation [115] and liquid crystal layer deposition[116]–[118], etc. The mentioned strategies suffer from several limitations such as high power-consumption, low integrability due to on chip invasive structures, small tuning range and low operational speed. In case of WGM resonators and lasers usually two parameters are used to control the properties of the circuits, i.e. radius of the structure and refractive index of the material. However, in case of coupled ring resonators [52], [53] the gap between the cavities can also be tuned [119], [120].

In the current chapter we exploit the presence of photoresponsive elements to tune the properties of photonic components. In particular, LCN is used in various ways to tune optical properties of whispering gallery mode micro goblet lasers [121], woodpiles [96], [107], photonic crystals[122], etc.

In our case, we explored the possibility of using liquid crystalline network (LCN) film to tune a gap between two active whispering gallery mode micro lasers.

5.2   System concept

LCN films are capable of controllable movement on macroscopic level. Engineering the alignment of liquid crystal mesogens in the polymer matrix (Section 3.3) allows to control the direction of the macroscopic movement. The proposed scheme comprises several materials, playing different roles in the final chip. In scheme the we designed, two polymeric micro disks are fabricated with direct laser writing on a surface of liquid crystalline film. When the film is activated, by either laser light or heat, the LCN phase transition leads to mechanical movement of the film that changes the intracavity gap (Figure 44). Considering the properties of the materials that are described in Chapter 3 and Chapter 4, stimulus removal

80

should lead to restoring of the initial gap, thus leading to reversible coupling-decoupling process.
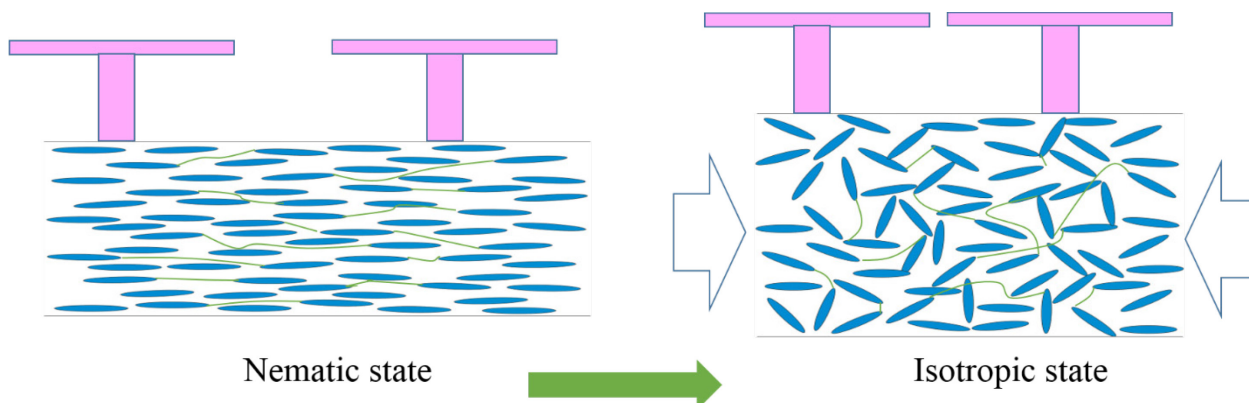
Figure 44. Coupling mechanism employing.

Let us consider the preparation of the structure in more details. The two possible options of implementation of the optical tuning of the structures are:

- to use the same laser for pumping the micro lasers and activating the substrate
- to use two different lasers in order to decouple these mechanisms.

Those two options differ, in terms of realization, by the chemical composition of the LCN mixtures (Figure 45). Considering that custom made azo-dye D6 has a peak in the absorption spectrum around λ=530 nm (Figure 46) and the Pyrromethene 597 laser-dye that is incorporated into polymeric micro-disks is usually pumped at wavelength λ=532 nm, it appears feasible to combine processes of excitation of micro-lasers and activation of polymer. However, one of the limiting factors of the current scheme is that although both mechanisms are activated by the same stimulus, the required stimulus intensity might be different.

Using another azo-dye DO3 (Disperse Orange 3, Sigma-Aldrich) it is possible to decouple two effects and use different excitation sources. DO3 has absorption

peak around λ=440 nm and, therefore, it's possible to use He-Cd cw-laser (Kimmon Koha, Ltd.) with emission at λ=442 nm.
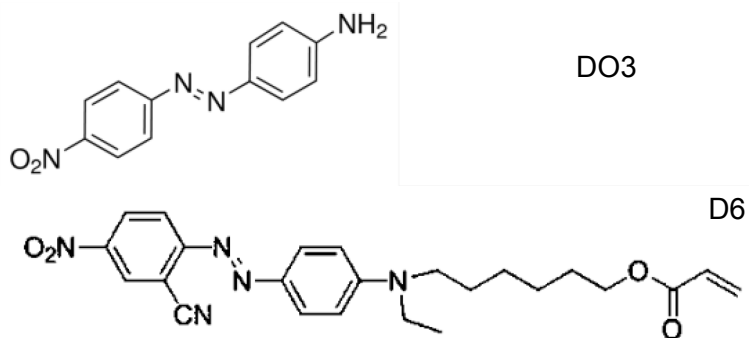
Figure 45. Structure of azo-dyes used in for LCN films.
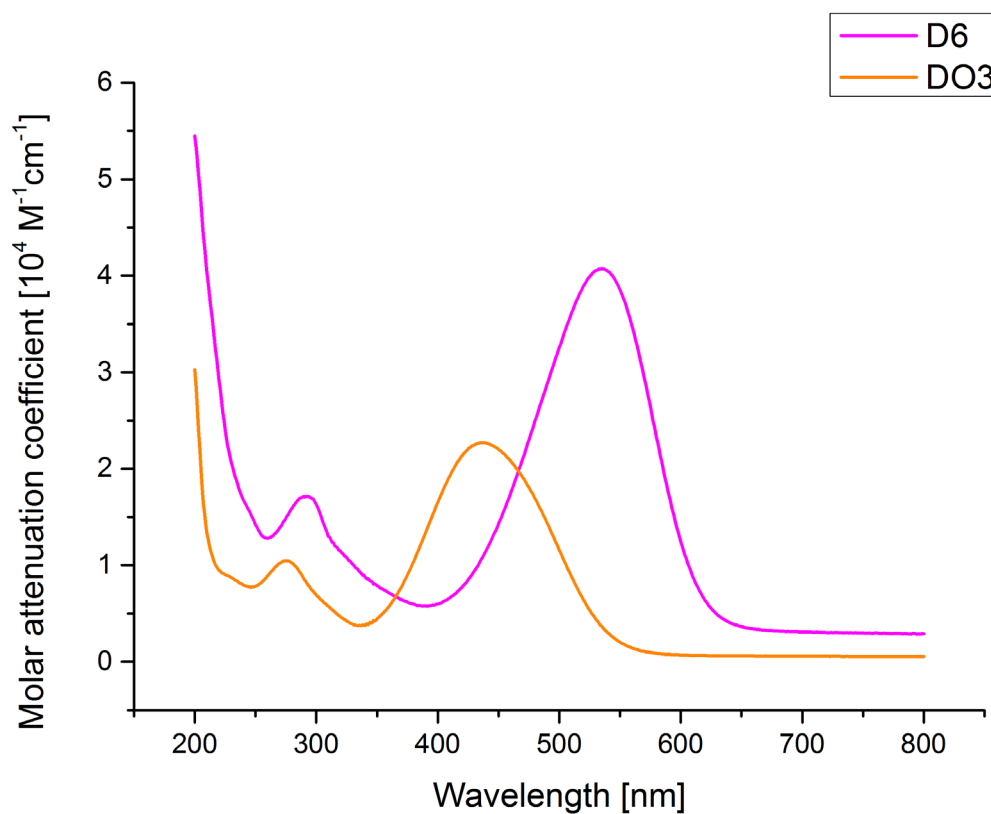
Figure 46. Absorption spectra of two dyes used for LCN preparation.

While the threshold for lasing of the those particular micro-lasers is known and reported in [119], the activation laser power of LCN film is rather difficult to estimate. Several values have been reported for cases of different molecular composition [78], [123]–[125], scale and size [37], [42], [96], [126]. In all the cases the structures are considered in free-standing or partly attached configurations.

5.3 Notes on using LCN film for changing intra-cavity gap

In our case we consider a polymer film with one side attached to a glass substrate. This configuration introduces several constraints to the possible movements of the other surface of the film.

At first, when the film is actuated, and phase transition occurs, the free surface, where WGM lasers are positioned, is contracting in one direction, and expanding in the perpendicular direction, while the other surface attached to the glass substrate remains intact, decreasing the movement of the first surface (Figure 47). This effect decreases with increasing thickness of the polymer film. However, it is not possible to fabricate a film thick enough to completely diminish the effect with our film preparation technique. In fact, it was experimentally proven, that with increasing the film thickness, the alignment of liquid crystal mesogens degrades rapidly. Polarized optical microscopy shows, that using the current mixture films up to 30 μm thick preserve good alignment within the whole volume of the film. Therefore, the optimal thickness of the film for our purpose is a subject of optimization.
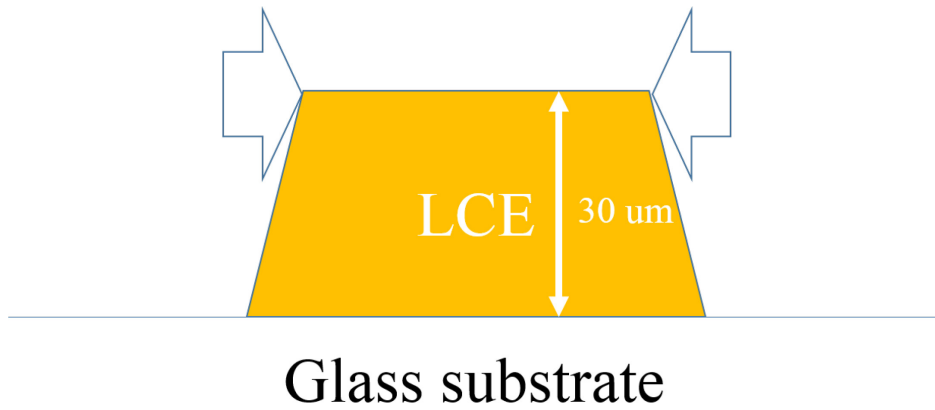
Glass substrate

Secondly, in consideration of the nature of phase transition that arises from heat which, in turn, is created by absorbed laser light, the heat dissipation rate could be an issue. While in [78], [123]–[125] the films response is tested when a film is not firmly attached to any surface like in our case, the heat dissipation rate is significantly different. When a film is attached to the surface of a glass without any air layer between them, heat accumulated in the film easily flows to the substrate and, increasing the power flow and, thus, laser power activation threshold.

Thirdly, in the configuration that we study, a film is much larger than a laser spot. Consequently, the phase transition happens only in a region approximately to the size of the laser spot. The remaining part of the film remains immobile, creating additional stress to the region of interest.

At last, although previous paragraphs described effects that imply an increase of activation laser power, we must note that real distance at which whispering gallery mode coupling occurs is around several hundreds of nanometers (300-400 nm for λ=1.55 μm and 100-200 nm for λ=610 nm). Therefore, the desired effect of the gap change does not have to be particularly large, and this might compensate for restrictions mentioned above.

Several films with uniaxial alignment were prepared for to be integrated with WGM micro-lasers. Both possibilities to use same and different excitation sources for pumping WGM micro disks and LCN film activation are explored by using different dyes -polymer film(PF) #1 contains azo-dye D6 and PF#2 contains DO3. In Figure 48 shown two films (PF#1 and PF#2), containing different dyes, which can be understood by the color. On each film fabricated several pairs of WGM lasers with intracavity gaps varying from 1 to 5 microns (white dots on the films).

5.4 Optical characterization of micro lasers

Optical characterization of micro lasers is performed by micro-photoluminescence spectroscopy. The micro lasers are pumped with 10 ns pulses of a frequency-doubled neodymium-doped yttrium orthovanadate (Nd:YVO4) laser at a wavelength λ=532 nm with varying repetition rate. Pulsed excitation with pump pulses shorter than the typical intersystem crossing rate of the dyes, is required to investigate lasing in micro cavities because it can prevent fluorescence quenching of the dyes owing to triplet formation[127], [128]. The pump beam is focused at an incident angle of ~45° to a spot size of ~100 μm, which allows the homogenous illumination of both cavities involved in the coupling process. The resonators can simultaneously be imaged on a camera and on the entrance slit of a spectrometer using optics that include a long-working distance microscope objective (magnification of 50x and numerical aperture of 0.4). By doing so, the photoluminescence emission can be analyzed with a spectrometer (focal length=0.5 m, 1200 or 2400 lines mm^{-1} grating) equipped with a charge-coupled device camera. Illustration schemes of the setup can be found in [121]. By orienting the sample so that the major axis of the PM is aligned parallel to the entrance slit, the setup allows the emitted light from the resonators to be not only spectrally resolved but also spatially resolved: WGM lasing emission from the distant rims of the cavities as well as from the coupling region can be simultaneously recorded and

can enable the distinction of non- coupled lasing modes of the individual cavities and lasing super- modes of the coupled photonic molecule [119].

5.5 Direct laser writing of WGM lasers

Direct laser writing of the WGM lasers is performed with the negative-tone resist OrmoComp (Micro Resist Technology GmbH, Berlin, Germany) that is doped with 20 μmol of the laser dye Pyrromethene 597 (Radiant Dyes Laser & Accessories GmbH, Wermelskirchen, Germany) per gram of photoresist[31]. The dye-doped resist is drop casted onto the LCN substrates and covered with a coverslip, using microscope cover slips as spacers with thickness of 100 μm, preventing the photoresist from falling off the substrate.
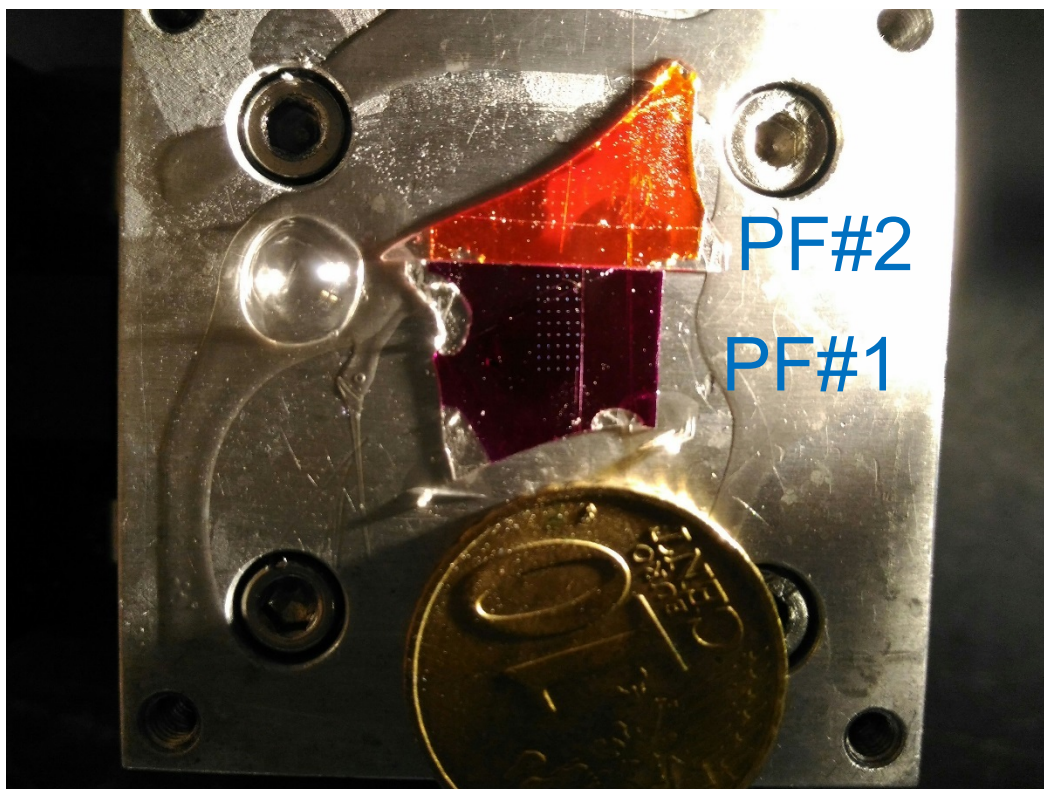
Figure 48. LCN film with arrays of WGM lasers.

5.6 Investigation of lasing properties of WGM micro-lasers

Every WGM mode disk is fabricated on a pedestal that is set to be 10 μm in height. However, due to the surface roughness of the LCN film, the precise interface

86

finding procedure that is needed for fabrication process is difficult to perform. For this reason, usually during the fabrication process interface position would be hard-set below the real interface to ensure that structures are attached to the surface. Therefore, the real height of the pedestals of the rings might vary. Moreover, during fabrication of big arrays of resonators that span on the scale of millimeters, for instance Figure 48, tilt and film thickness variation could reach values exceeding the set height of the pedestals. In this case the fabricated disks are either washed away during development process or fabricated directly on surface that leads of absence of lasing.

Figure 49-a) depicts a pair of WGM disks with fabricated intracavity gap. In Figure 49-b) demonstrated an optical image of pumped WGM lasers. The pump laser spot covers the whole area of the disks. The disks themselves are visible due to fluorescence of the laser dye and red spots indicate lasing of the structures.
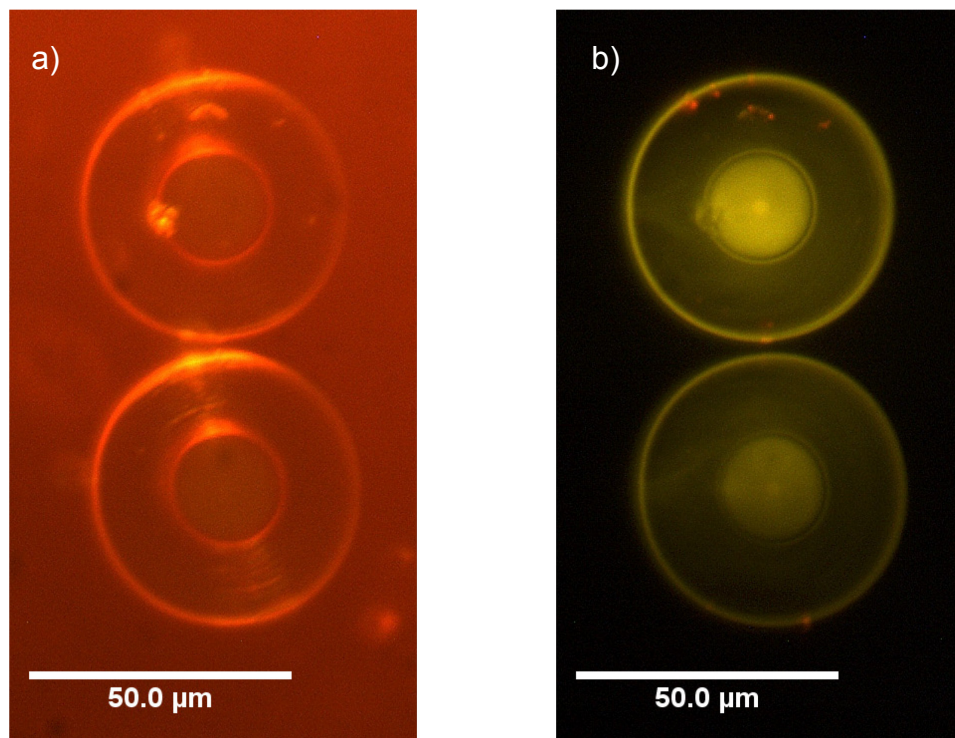
Figure 49. a) Optical image of WGL micro lasers with white lamp b) Lasing of WGM lasers. The pump laser spot covers the whole area of the disks. The disks themselves are visible due to fluorescence of the laser dye and red spots indicate lasing of the structures.

The typical spectrum acquired from the micro disks is shown in Figure 50. The continuous background line corresponds to fluorescence of the PM 597, while all the peaks except the one at λ=532 nm (which matches not completely filtered pump laser) correspond to lasing modes of both disks.
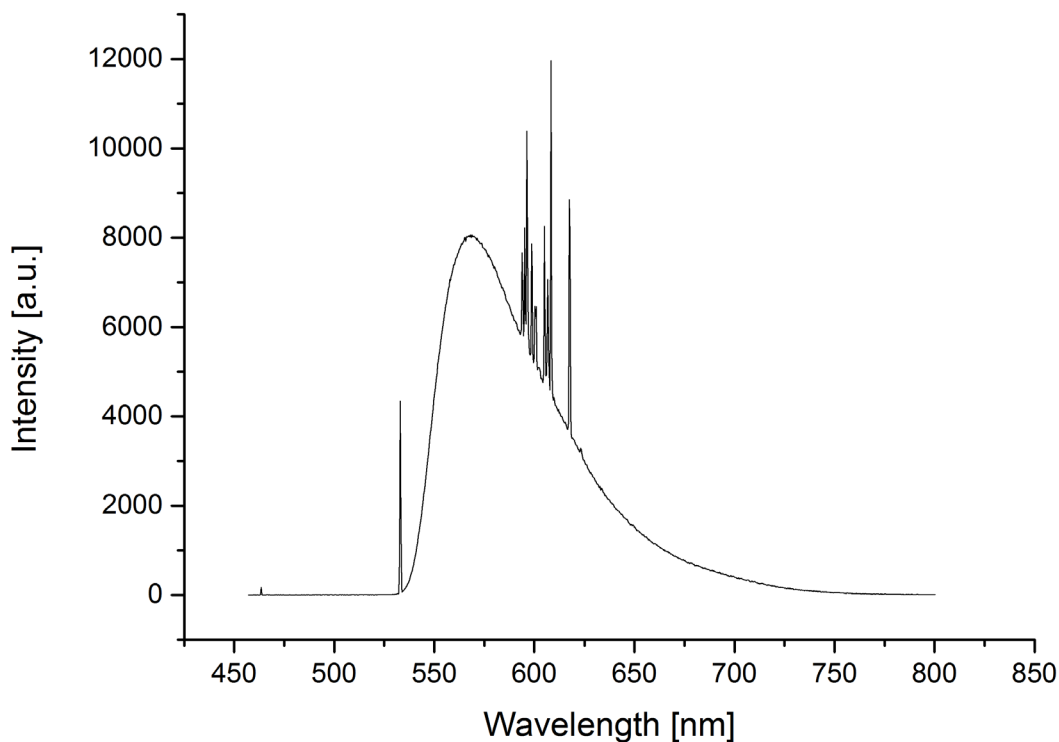
Figure 50. Lasing spectrum of WGM disks.

In case of spatially resolved spectroscopy, a slit of the spectrometer is positioned on the disks and depending on the position it is possible to record lasing spectra (depending on spatial positioning of emission points). Figure 51 shows example of spatially resolved spectrum acquired from a couple of WGM disk lasers. In Figure 51, the *x* axis corresponds to a wavelength, and the *y* axis represents *y* coordinate on the sample, and x coordinate on the sample is set by a slit position and is fixed for the whole spectrum. The two thick horizontal lines visible in Figure 51

correspond to fluorescence of the disks and pedestals and several lasing peaks stand out of the background on the rim of the top disk.

The clear spectral evidence of WGM lasers coupling is extension of lasing modes from each single cavity into super-modes, when two disks are considered to be a single cavity. In this case Vernier effect reduces amount of allowed modes and might even lead to single-mode lasing [129]. Spatially resolved spectroscopy is used to verify existence of supermodes.
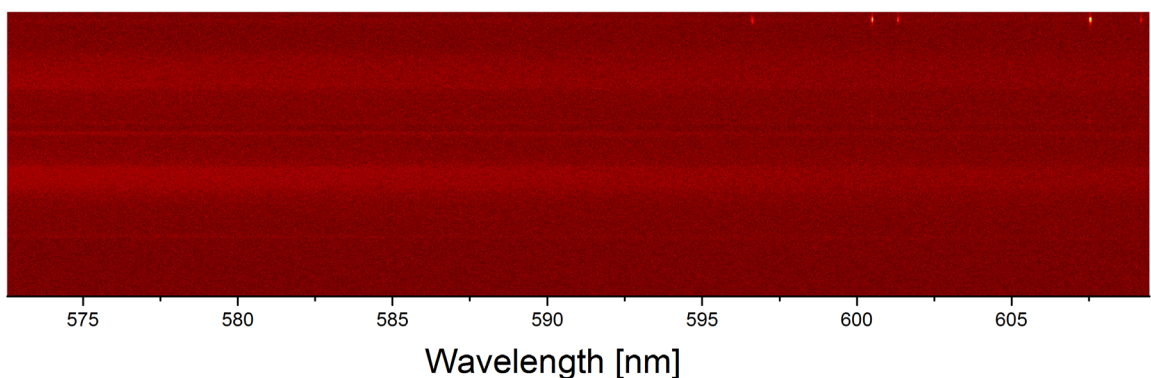
Figure 51. Spatially resolved spectrum of two whispering gallery lasers.

The next test to perform is to verify that LCN film is capable of significant deformation with stimulus intensity that does not damage the micro lasers. For this purpose, we expose our film to laser radiation varying the power flux (in case of pulsed laser we are able to change values of power per pulse and repetition rate separately).

5.6.1 PF#1 deformation investigation

Figure 52a)-c) depict the position of the edge of a film acquired with different power settings of the excitation 532 nm laser. Figure 52-d) depicts the composition of images a-c) to clarify the deformation. Here and after Canny Edge detection algorithm is applied to images followed by forming multichannel color stack, where each color corresponds to one frame (usually, color) to see the effect of the contraction more clearly. The absolute value of deformation in the x direction is

approximately 4 μm, which is largely sufficient for our application. However, this maximal deformation has been achieved with an average power of p=15 mW, low energy per pulse value, but high repetition rate (around 22 kHz). This repetition rate value is relatively high, and it does not meet the requirements necessary for laser emission. Moreover, we considered the edge of the film, where deformation is higher for several reasons. In this view, the strategy of using two different lasers appears more promising.
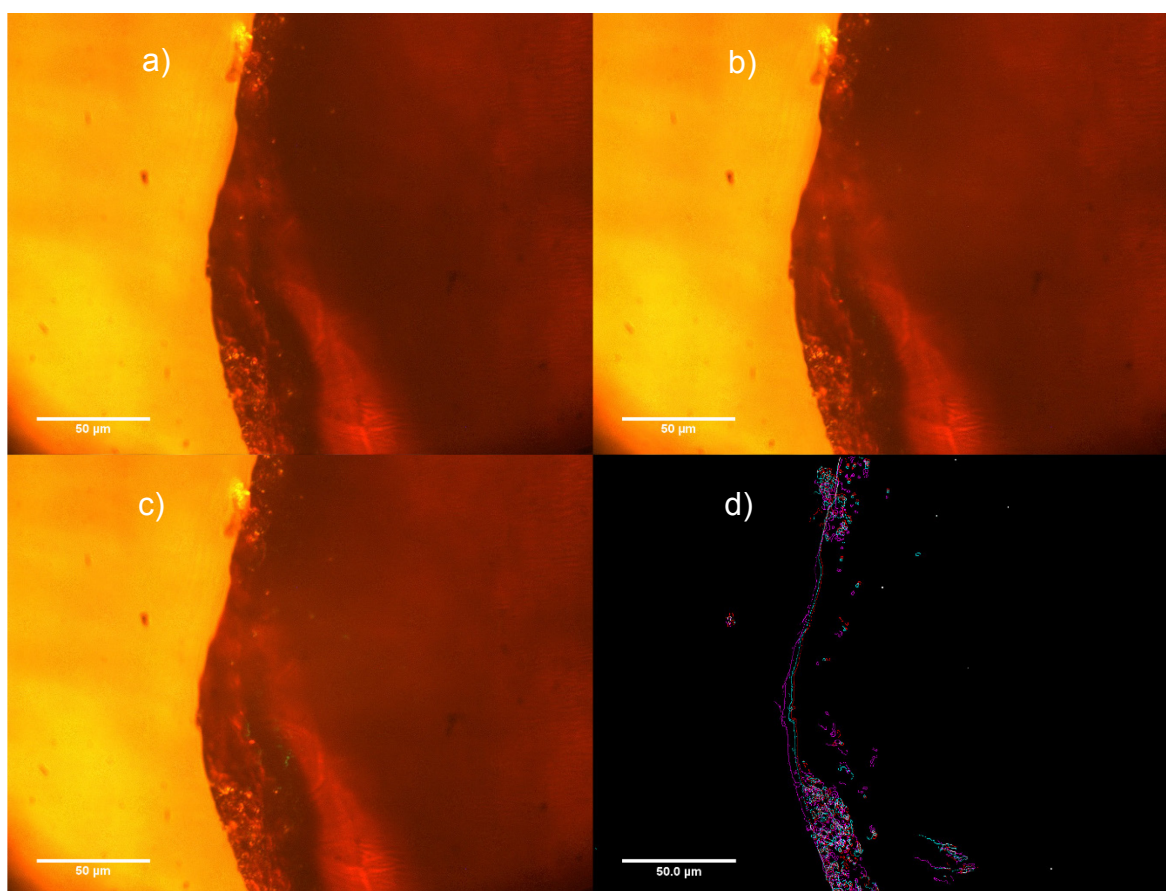
Figure 52. Deformation of PF#1: absence of excitation (a), excitation with 1.45 mW of 532 nm laser, (c) excitation excitation with 15 mW of 532 nm laser, (d) color composite

5.6.2 PF#2 deformation investigation

Current LCN mixture has never been tested with DO3 azo-dye incorporated in matrix, and therefore verification of the movement and deformation is required.

One significant modification is done in order to increase the tuning size range, based on the issues discussed in the Section 5.3: a film is cut in proximity, meaning a distance smaller than characteristic size of the excitation area (laser spot size), to the region of interest. In that case, the unperturbed area of a film does not create stress preventing the contraction and, therefore, the required excitation power is decreased. Ideally, the region where the microdisks are located, should be cut out from all the four sides, which can be easily done manually with a sharp knife and a sharp eye without the need to resort to direct laser writing.

Figure 53 depicts a deformation in the area near a cut of LCN film (wide horizontal line across the image). Red contours correspond to the state of film in the absence of external stimulus, while the green contour marks the position of the film in the presence of excitation (the laser spot is in the right bottom part of the image). The appearing yellow color is a result of green and red channels summation - corresponding to undisturbed area.
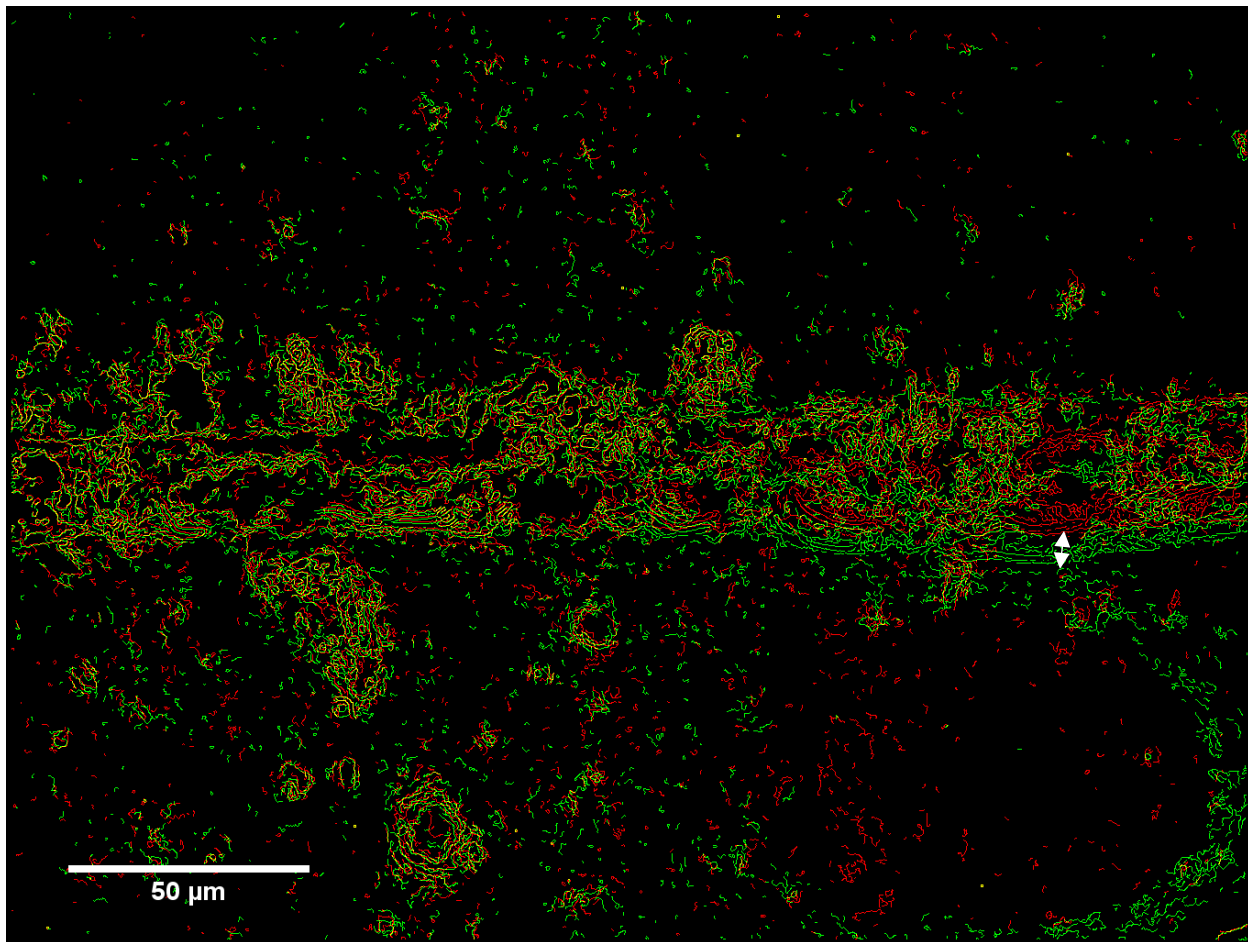
Figure 53. Deformation near a cut of PF#2.

A white arrow in Figure 53 indicates the area of maximal deformation that is approximately equal to 10 µm achieved with laser power of p≈30 mW.

Based on this result we prepared several pairs of WGM lasers close to the edge of film and close to several cuts (Figure 54). It's been discovered that illuminating the PM 597 micro lasers with CW illumination at λ=442 nm (corresponding to absorption minimum of laser dye) still the net effect results in suppression of lasing and photobleaching of the dye. In order to prevent this from happening, the reasonable strategy is to reposition excitation (442 nm) laser spot away from the disks, while still keeping it sufficiently close so as contraction of the film will move the disks.

92
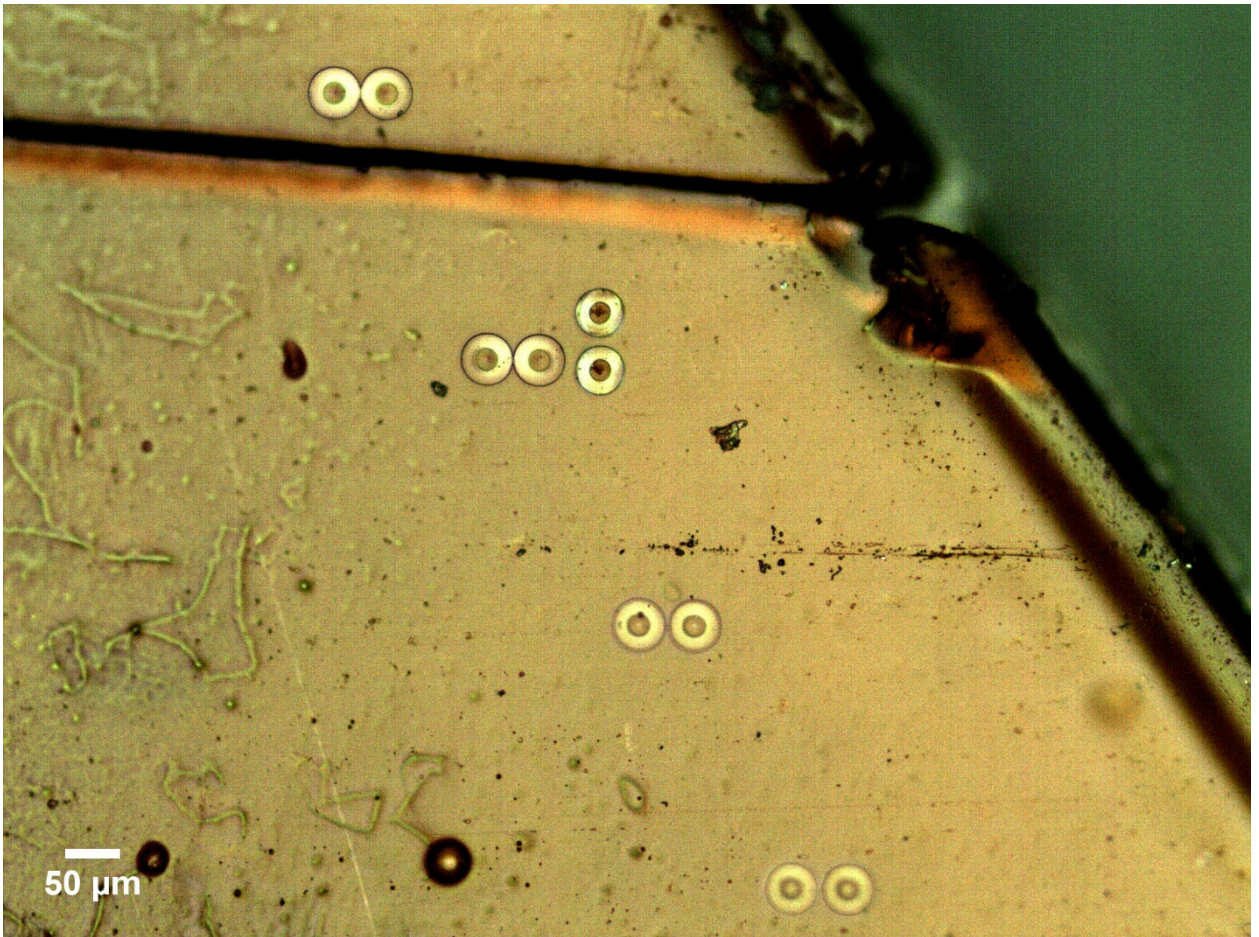
Figure 54. PF#2 with WGM lasers.

A pair with intracavity gap of 3 µm is chosen for demonstration of coupling mechanism (Figure 55). To achieve the change of the gap the excitation laser spot had to be placed on a side of the disks. That completely eliminated lasing from the disks. Nonetheless the demonstration of reversible coupling of the disks achieved with stimulus power p≈31.5 mW. Although higher power is available, this might damage the micro disks lasers. Figure 55 demonstrates the change of the intracavity gap, with a)- excitation 442 nm is *off*, b)- excitation is *on*, c)- color composite.
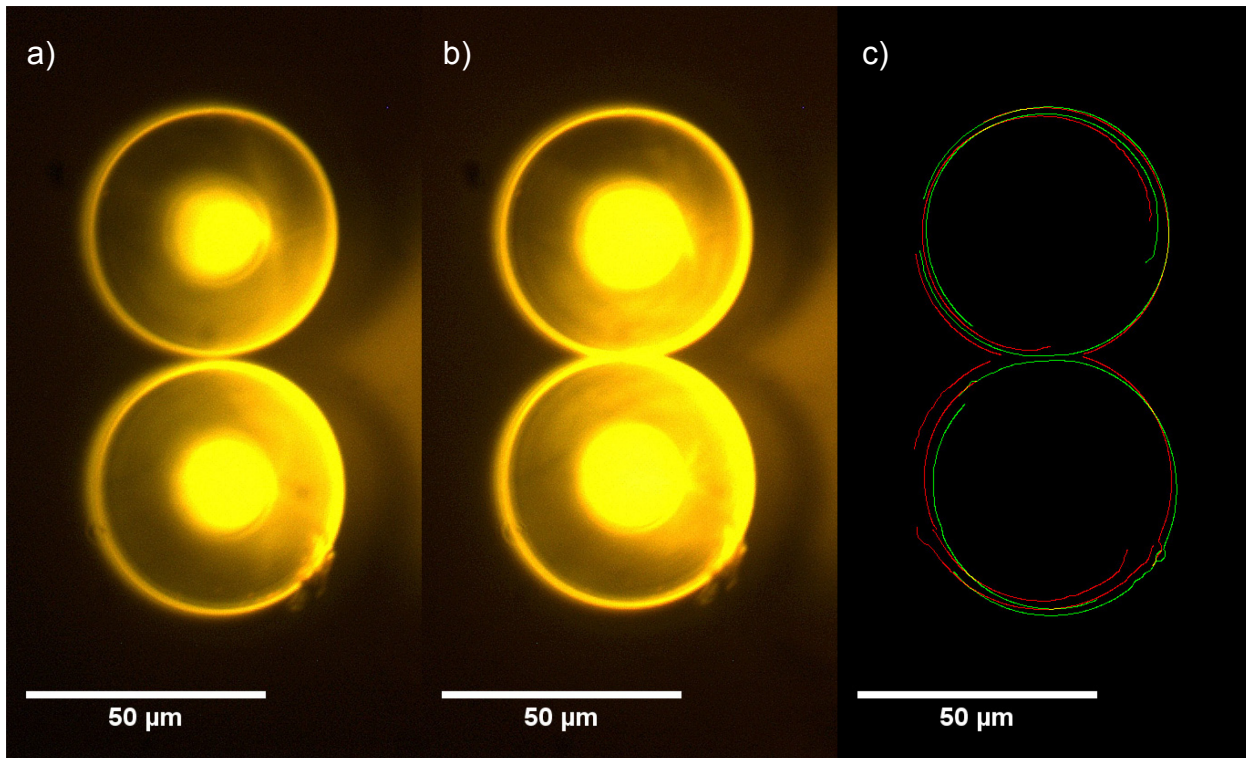
Figure 55. Coupling of two micro disks. a) excitation 442 nm *off*, b) excitation *on*, c) color composite.

As was mentioned above, once the stimulus removed (in our case, the 442 nm laser is turned off), the LCN structures expands nearly to the initial stage increasing the gap, making this process reversible.

5.7 Conclusions and outlook

In this chapter we demonstrated a use of shape-changing liquid crystalline network film applied to tuning intracavity gap of WGM micro disk lasers. Even though some technical difficulties are still to be resolved, the overall principle of optically induced tuning of coupling gap is shown. Applying macroscopic film fabrication procedure combined with conventional direct laser writing of microlasers opens a possibility of large scale fabrication of chip-scale devices, where for example, optical source of excitation can be changed into a heating element to trigger thermal actuation. In case bigger tuning range is required, the composition of the LCN mixture should be tuned respectively. At last, for modification of the current scheme is envisioned, in which, we illuminate the LCN film from the back side of

the chip. In that case, considering transparency of the glass substrate and opaqueness of the LCN film at λ=442 nm, the film would absorb nearly all the laser light leading to the local heating and, therefore, contraction of the film, but would not illuminate the micro lasers and photo bleach the laser dye.

Conclusions

In this thesis we tried to address several important problems in modern photonic research, broadening knowledge in the areas of integrated photonic components and optomechanics. In the first part we developed a novel tool for complex analysis of integrated photonic circuits and components. The technique allows to see the time-response of the studied structures on sub-picosecond scale and even to image the pulse propagation resolving the time-frames on the same scale. We report investigation of direct laser written polymeric photonic components and advances in double layered electron beam lithographically fabricated complex photonic circuits. However, the technique is not limited by choice of the materials and can be widely applied both to modern commercial industrial products during development and optimization processes. The described technique can also be applied in academic research, where, for instance it can serve in the recently developed of waveguide-based machine learning systems.

In the next part of the thesis, introducing a smart material that is capable of changing the its shape in response to external stimuli, we show the material application in fields of photonics and optomechanics. In a separate chapter we demonstrate a novel micro robotic device, which is being several hundred microns in size, can be controlled remotely by a laser beam. As presented micro gripper can catch and release different kinds of particles, it is also capable of autonomous action, when that act of gripping is triggered by a color of a target. We believe that the concept of this structure can be used in different areas of science and technology.

In the last part of the thesis we address a well-known issue of photonic structures tunability. Continuing to search novel approaches of multi-material combination within a single chip we present a principle of optomechanical tuning of photonic components with use of smart polymers. We describe a process that does not require microfabrication facility for smart polymer integration. Although this

demonstration is not complete, the main principle, however, is evident. As a future perspective this process can be scaled up to bigger structures, allowing, for instance, simultaneous tuning of big arrays of coupled resonators.

Acknowledgements

Firstly, I would like to thank my two advisers Diederik and Heinz, who had been supervising me during those three years, for unlimited support they provided me and unprecedent freedom they gave me to find my own path. Separately I would like to thank Sophie Brasselet for creating and coordinating EMJD program EUROPHOTONICS. Without these three people all this project would not be possible.

Secondly, my colleagues and friends who I am happy to learn from. I thank Lorenzo who has been sharing with me his experience and approach to doing things. And I've learnt a lot and hope to learn even more! I am grateful to Sara for being always there and helping me (not only!) in all the possible ways. She has been not only teaching me practical things, but also explaining new concepts with patience. I thank Lorenzo and Sara for being with me and Francesco till the last minutes of this PhD-course. Of course, I thank Francesco – the inexhaustible source of cheerfulness. We had been carrying the weight of doing PhD together every single day of past three years and without him it would have been ways harder. Of course, I cannot forget about Hao, who taught me so many tricks in the lab (and outside of it!). Chih-Hua and Łukasz, thank you for the good company and long discussions that were held on the shore of Ligurian sea.

Thirdly, our chemists are definitely the best in the world – Camilla, Daniele and Flavia, thank you for making chemistry to serve physicists. And of course, the people who create the whole atmosphere of research institute, people who can give a valuable piece of advice and just brighten a day in the lab: Giacomo Mazzamuto (who could have created a new IT Corp, but does not want to leave the apartment in Sesto), Francesco Biccari (who makes smile no matter what), Francesco Riboli (who is capable of explaining very complex things with very simple words), Lorenzo Cortese (Lab 9 still misses you!), Sofia (who would always listen to you) and Maja

(who is always in a rush), Pietro (the one that is always late), Simona (although she is very far from LENS now), Simone Zanotto (who always finds a bright part in an experiment that seemed to fail), Jeroen van den Brink (who stayed here only for three months, but for three valuable months), Fabrizio (who immediately sees the both the problem and the solution), Alice (with her great attitude), Sahrish (who is a great photographer with PhD degree), Francesca Intonti and Costanza Toninelli.

No doubt that the Karlsruhe team deserves a separate acknowledgment. Tobias and Carolin, thank you for taking a good care of me and Jasmin – for making me more organized. Pablo and Diana, thank you for the great days and nights in Karlsruhe. A special thank goes to Amos for fruitful discussions about optics, life and cheese. Especially life.

At last, I am infinitely grateful to my family and my Russian friends, who are almost a family for me. Mom, Dad, grandma Evelina, thank you for believing in me. Separately, Genia, thank you for unlimited support. Sasha, Serioja, Vova, Katia, Olya, Elena, Dasha we all did it together.

At last I would like to thank Pompilio Stropiccioli for encouraging me to take an action and all three snakes that sneaked in the labs during these years.

List of publications

[1]   D. S. Wiersma, S. Nocentini, C. Parmeggiani, D. Martella, and D. Nuzhdin, "Photonic arms, legs, and skin," in *Optical Trapping and Optical Micromanipulation XIV*, 2017, vol. 10347, p. 99.

[2]   D. Martella, S. Nocentini, D. Nuzhdin, C. Parmeggiani, and D. S. Wiersma, "Photonic Microhand with Autonomous Action," *Adv. Mater.*, vol. 1704047, p. 1704047, 2017.

[3]   D. Nuzhdin, L. Pattelli, S. Nocentini and D. Wiersma "Complex spatio-temporal charachterization of integrated photonic components", *2018* In preparation

Contributions

Chapter 2. Construction, characterization of the apparatus, simulations, data analysis are done by the author. Designing of resonator assembly and linewidth measurements are done by Dr. Sara Nocentini and fabrication (DLW) is done both by author and Dr. Sara Nocentini.

Design, preparation, and analysis of the structures prepared with EBL are done by the author. Prepared spin-coated substrates are exposed by Karlsruhe Nano Micro Facility Team (Dr. Lothar Hahn and Dr. Andreas Bacher).

Chapter 4. System concept is developed by the author, design and sample fabrication of Gripper A is done by the author. Design and sample fabrication of Gripper B is done by Dr. Daniele Martella. The rest of the activity is shared between Dr. Sara Nocentini, Dr. Daniele Martella and the author.

Chapter 5. Sample fabrication was done by the author together with MSc Michael Remmel. The rest of the work described in this chapter was done by the author.

List of figures

104

experiment shows that, depending on input frequency, the light takes the short edge (a) or the long edge (b). The experimental results (a,b) are in good agreement with the simulation results (c,d). e, SEM image of the system (Adapted from [16]).

106

References

[1] H. Haus, *Waves and Fields in Optoelectronics*. 1985.

[2] K. Okamoto, *Fundamentals of Optical Waveguides*. 2006.

[3] A. Yariv, "Coupled-Mode theory for guided-wave optics," *IEEE J. Quantum Electron.*, vol. 9, no. 9, pp. 919–933, 1973.

[4] J. Arnaud, "Optical waveguide theory," *Optical and Quantum Electronics*, vol. 12, no. 3. pp. 187–191, 1980.

[5] J. Van Roey, J. van der Donk, and P. E. Lagasse, "Beam-propagation method: analysis and assessment," *J. Opt. Soc. Am.*, vol. 71, no. 7, p. 803, Jul. 1981.

[6] W. S. Lord Rayleigh, "Theory of Sound," in *Theory of Sound*, vol. 1, 1895, p. 235.

[7] A. B. Matsko and V. S. Ilchenko, "Optical resonators with whispering-gallery modes - Part I: Basics," *IEEE J. Sel. Top. Quantum Electron.*, vol. 12, no. 1, pp. 3–14, 2006.

[8] V. S. Ilchenko and A. B. Matsko, "Optical resonators with whispering-gallery modes-part II: applications," *IEEE J. Sel. Top. Quantum Electron.*, vol. 12, no. 1, pp. 15–32, Jan. 2006.

[9] A. A. Savchenkov, V. S. Ilchenko, A. B. Matsko, and L. Maleki, "High-order tunable filters based on a chain of coupled crystalline whispering gallery-mode resonators," *IEEE Photonics Technol. Lett.*, vol. 17, no. 1, pp. 136–138, 2005.

[10] F. Vollmer and S. Arnold, "Whispering-gallery-mode biosensing: label-free detection down to single molecules," *Nat. Methods*, vol. 5, no. 7, pp. 591–596, Jul. 2008.

[11] X. Fan, I. M. White, S. I. Shopova, H. Zhu, J. D. Suter, and Y. Sun, "Sensitive optical biosensors for unlabeled targets: A review," *Anal. Chim. Acta*, vol. 620, no. 1–2, pp. 8–26, Jul. 2008.

[12] K. J. Vahala, "Optical microcavities," *Nature*, vol. 424, no. 6950, pp. 839–846, 2003.

[13] M. Bayer, T. L. Reinecke, F. Weidner, A. Larionov, A. McDonald, and A. Forchel, "Inhibition and enhancement of the spontaneous emission of quantum dots in structured microresonators," *Phys. Rev. Lett.*, vol. 86, no. 14, pp. 3168–3171, 2001.

[14] D. Van Thourhout and J. Roels, "Optomechanical device actuation through the optical gradient force," *Nat. Photonics*, vol. 4, no. 4, pp. 211–217, 2010.

[15] T. J. Kippenberg and K. J. Vahala, "Cavity opto-mechanics.," *Opt. Express*, vol. 15, no. 25, pp. 17172–205, 2007.

[16] M. Hafezi, S. Mittal, J. Fan, A. Migdall, and J. M. Taylor, "Imaging topological edge states in silicon photonics," *Nat. Photonics*, vol. 7, no. 12, pp. 1001–1005, 2013.

[17] S. L. McCall, A. F. J. Levi, R. E. Slusher, S. J. Pearton, and R. A. Logan, "Whispering-gallery mode microdisk lasers," *Appl. Phys. Lett.*, vol. 60, no. 3, pp. 289–291, 1992.

[18] J. Čtyroký, I. Richter, and M. Šiňor, "Dual resonance in a waveguide-coupled ring microresonator," *Opt. Quantum Electron.*, vol. 38, no. 9–11, pp. 781–797, 2006.

[19] G. C. Righini *et al.*, "Whispering Gallery Mode microresonators: Fundamentals and applications," *Riv. del Nuovo Cim.*, vol. 34, no. 7, pp. 435–488, 2011.

[20] W. Kaiser and C. G. B. Garrett, "Two-Photon Excitation in Ca F_2 : Eu $2+$," *Phys. Rev. Lett.*, vol. 7, no. 6, pp. 229–231, Sep. 1961.

[21] M. Drobizhev, N. S. Makarov, S. E. Tillo, T. E. Hughes, and A. Rebane, "Two-photon absorption properties of fluorescent proteins," *Nat. Methods*, vol. 8, no. 5, pp. 393–399, May 2011.

[22] S. Thiele, K. Arzenbacher, T. Gissibl, H. Giessen, and A. M. Herkommer, "3D-printed eagle eye: Compound microlens system for foveated imaging," *Sci. Adv.*, vol. 3, no. 2, p. e1602655, Feb. 2017.

[23] G. Von Freymann *et al.*, "Three-Dimensional Nanostructures for Photonics."

[24] J. Trull *et al.*, "Formation of collimated beams behind the woodpile photonic crystal," *Phys. Rev. A*, vol. 84, no. 33812, 2011.

[25] A. Radke, T. Gissibl, T. Klotzbücher, P. V. Braun, and H. Giessen, "Three-Dimensional Bichiral Plasmonic Crystals Fabricated by Direct Laser Writing and Electroless Silver Plating," *Adv. Mater.*, vol. 23, no. 27, pp. 3018–3021, Jul. 2011.

[26] D. Wu *et al.*, "Femtosecond laser rapid prototyping of nanoshells and suspending

components towards microfluidic devices," *Lab Chip*, vol. 9, no. 16, p. 2391, Aug. 2009.

[27]   A. Ovsianikov, X. Shizhou, M. Farsari, M. Vamvakaki, C. Fotakis, and B. N. Chichkov, "Shrinkage of microstructures produced by two-photon polymerization of Zr-based hybrid photosensitive materials," *Opt. Express*, vol. 17, no. 4, p. 2143, 2009.

[28]   O. Tricinci, T. Terencio, B. Mazzolai, N. M. Pugno, F. Greco, and V. Mattoli, "3D Micropatterned Surface Inspired by *Salvinia molesta* via Direct Laser Lithography," *ACS Appl. Mater. Interfaces*, vol. 7, no. 46, pp. 25560–25567, Nov. 2015.

[29]   C. Kern, M. Kadic, and M. Wegener, "Experimental Evidence for Sign Reversal of the Hall Coefficient in Three-Dimensional Metamaterials," *Phys. Rev. Lett.*, vol. 118, no. 1, p. 16601, Jan. 2017.

[30]   K. Terzaki *et al.*, "3D conducting nanostructures fabricated using direct laser writing," *Opt. Mater. Express*, vol. 1, no. 4, p. 586, Aug. 2011.

[31]   T. Grossmann *et al.*, "Direct laser writing for active and passive high-Q polymer microdisks on silicon.," *Opt. Express*, vol. 19, no. 12, pp. 11451–11456, 2011.

[32]   Y. Zhou *et al.*, "Microstructuring of Graphene Oxide Nanosheets Using Direct Laser Writing," *Adv. Mater.*, vol. 22, no. 1, pp. 67–71, Jan. 2010.

[33]   S. Maruo, O. Nakamura, and S. Kawata, "Three-dimensional microfabrication with two-photon-absorbed photopolymerization," *Opt. Lett.*, vol. 22, no. 2, p. 132, Jan. 1997.

[34]   S. W. Hell and J. Wichmann, "Breaking the diffraction resolution limit by stimulated emission: stimulated-emission-depletion fluorescence microscopy," *Opt. Lett.*, vol. 19, no. 11, p. 780, Jun. 1994.

[35]   J. Fischer, T. Ergin, and M. Wegener, "Three-dimensional polarization-independent visible-frequency carpet invisibility cloak," *Opt. Lett.*, vol. 36, no. 11, p. 2059, 2011.

[36]   F. Formanek, N. Takeyasu, T. Tanaka, K. Chiyoda, A. Ishikawa, and S. Kawata, "Three-dimensional fabrication of metallic nanostructures over large areas by two-photon polymerization," *Opt. Express*, vol. 14, no. 2, p. 800, Jan. 2006.

[37]   H. Zeng, P. Wasylczyk, C. Parmeggiani, D. Martella, M. Burresi, and D. S. Wiersma,

"Light-Fueled Microscopic Walkers," *Adv. Mater.*, vol. 27, no. 26, pp. 3883–3887, 2015.

[38] D. Martella, S. Nocentini, D. Nuzhdin, C. Parmeggiani, and D. S. Wiersma, "Photonic Microhand with Autonomous Action," *Adv. Mater.*, vol. 29, no. 42, p. 1704047, 2017.

[39] S. Kawata, H.-B. Sun, T. Tanaka, and K. Takada, "Finer features for functional microdevices," *Nature*, vol. 412, no. 6848, pp. 697–698, 2001.

[40] Nanoscribe GmbH, "IP Photoresists - Nanoscribe GmbH." .

[41] A. Nishiguchi, A. Mourran, H. Zhang, and M. Möller, "In-Gel Direct Laser Writing for 3D-Designed Hydrogel Composites That Undergo Complex Self-Shaping," *Adv. Sci.*, p. 1700038, Jul. 2017.

[42] H. Zeng *et al.*, "High-resolution 3d direct laser writing for liquid-crystalline elastomer microstructures," *Adv. Mater.*, vol. 26, no. 15, pp. 2319–2322, 2014.

[43] S. Nocentini, D. Martella, C. Parmeggiani, and D. Wiersma, "Photoresist Design for Elastomeric Light Tunable Photonic Devices," *Materials (Basel).*, vol. 9, no. 7, p. 525, Jun. 2016.

[44] P. Rai-Choudhury, *Handbook of Microlithography, Micromachinging, and Microfabrication*, vol. 2. 1997.

[45] T. Grossmann *et al.*, "High-Q conical polymeric microcavities," *Appl. Phys. Lett.*, vol. 96, no. 1, p. 13303, Jan. 2010.

[46] J. W. Lussi *et al.*, "Selective molecular assembly patterning at the nanoscale: a novel platform for producing protein patterns by electron-beam lithography on SiO_2/indium tin oxide-coated glass substrates," *Nanotechnology*, vol. 16, no. 9, pp. 1781–1786, Sep. 2005.

[47] T. Wienhold *et al.*, "All-polymer photonic sensing platform based on whispering-gallery mode microgoblet lasers.," *Lab Chip*, vol. 15, no. 18, pp. 3800–6, 2015.

[48] C. Vieu *et al.*, "Electron beam lithography: resolution limits and applications," *Appl. Surf. Sci.*, vol. 164, no. 1–4, pp. 111–117, Sep. 2000.

[49] R. Duncan, B. Soller, and D. Gifford, "OFDR-based distributed sensing and fault detection for single-and multi-mode avionics fiber-optics," *Jt. Conf. Aging Aircr.*, 2007.

110

[50] M. K. Barnoski, M. D. Rourke, S. M. Jensen, and R. T. Melville, "Optical time domain reflectometer," *Appl. Opt.*, vol. 16, no. 9, pp. 2375–2379, 1977.

[51] U. Glombitza and E. Brinkmeyer, "Coherent Frequency-Domain Reflectometry for Characterization of Singlemode Integrated optical Waveguides," *J. Light. Technol.*, vol. 11, no. 8, pp. 1377–1384, 1993.

[52] C. Ferrari and F. Morichetti, "Disorder in coupled-resonator optical waveguides," *Josa B*, vol. 26, no. 4, p. 858, 2009.

[53] A. Melloni, F. Morichetti, and M. Martinelli, "Linear and nonlinear pulse propagation in coupled resonator slow-wave optical structures," *Opt. Quantum Electron.*, vol. 35, no. 4–5, pp. 365–379, 2003.

[54] W. C. L. Hopman, H. J. W. M. Hoekstra, R. Dekker, L. Zhuang, and R. M. de Ridder, "Far-field scattering microscopy applied to analysis of slow light, power enhancement, and delay times in uniform Bragg waveguide gratings.," *Opt. Express*, vol. 15, no. 4, pp. 1851–70, 2007.

[55] M. L. M. Balistreri *et al.*, "Visualizing the whispering gallery modes in a cylindrical optical microcavity," *Opt. Lett.*, vol. 24, no. 24, pp. 1829–1831, 1999.

[56] M. L. M. Balistreri, H. Gersen, J. P. Korterik, L. Kuipers, and N. F. van Hulst, "Tracking Femtosecond Laser Pulses in Space and Time," *Science (80-.).*, vol. 294, no. 5544, pp. 1080–1082, 2001.

[57] N. Caselli *et al.*, "Ultra-subwavelength phase-sensitive Fano-imaging of localized photonic modes," *Light Sci. Appl.*, vol. 4, no. 9, p. e326, 2015.

[58] R. Bruck *et al.*, "Device-level characterization of the flow of light in integrated photonic circuits using ultrafast photomodulation spectroscopy," *Nat. Photonics*, vol. 9, no. 1, pp. 54–60, 2014.

[59] R. Trebino *et al.*, "Measuring ultrashort laser pulses in the time-frequency domain using frequency-resolved optical gating," *Rev. Sci. Instrum.*, vol. 68, no. 9, p. 3277, Sep. 1997.

[60] J. C. Blake, J. Nieto-Pescador, Z. Li, and L. Gundlach, "Ultraviolet femtosecond Kerr-gated wide-field fluorescence microscopy," *Opt. Lett.*, vol. 41, no. 11, pp. 2462–2465, 2016.

[61] S. Minardi *et al.*, "Three-dimensional light bullets in arrays of waveguides," *Phys. Rev. Lett.*, vol. 105, no. 26, 2010.

[62] C. Dunsby and P. M. W. French, "Techniques for depth-resolved imaging through turbid media including coherence-gated imaging," *J. Phys. D. Appl. Phys.*, vol. 36, no. 14, pp. R207–R227, 2003.

[63] L. Pattelli, R. Savo, M. Burresi, and D. S. Wiersma, "Spatio-temporal visualization of light transport in complex photonic structures," *Light Sci. Appl.*, vol. 5, no. 5, p. e16090, Feb. 2016.

[64] Z. Wang *et al.*, "Efficient second harmonic generation of pulsed laser radiation in BiB3O6 (BIBO) crystal with different phase matching directions," *Opt. Commun.*, vol. 202, no. 1–3, pp. 217–220, Feb. 2002.

[65] L. Pattelli, "International Doctorate in Atomic and Molecular Photonics Imaging light transport at the femtosecond scale : a walk on the wild side of diffusion," University of Florence, 2016.

[66] M. H. P. Moers, R. G. Tack, N. F. Van Hulst, and B. B??lger, "Photon scanning tunneling microscope in combination with a force microscope," *J. Appl. Phys.*, vol. 75, no. 3, pp. 1254–1257, 1994.

[67] D. J. W. Klunder *et al.*, "Detailed analysis of the intracavity phenomena inside a cylindrical microresonator," *J. Light. Technol.*, vol. 20, no. 3, pp. 519–529, 2002.

[68] H. Gersen, E. M. H. P. Van Dijk, J. P. Korterik, N. F. Van Hulst, and L. Kuipers, "Phase mapping of ultrashort pulses in bimodal photonic structures: A window on local group velocity dispersion," *Phys. Rev. E - Stat. Nonlinear, Soft Matter Phys.*, vol. 70, no. 6 2, pp. 1–12, 2004.

[69] Y. Shen *et al.*, "Deep learning with coherent nanophotonic circuits," *Nat. Photonics*, vol. 11, no. 7, pp. 441–446, Jun. 2017.

[70] S. Mittal, J. Fan, S. Faez, A. Migdall, J. M. Taylor, and M. Hafezi, "Topologically robust transport of photons in a synthetic gauge field," *Phys. Rev. Lett.*, vol. 113, no. 8, pp. 1–5, 2014.

[71] S. Mittal, S. Ganeshan, J. Fan, A. Vaezi, and M. Hafezi, "Measurement of topological invariants in a 2D photonic system," *Nat. Photonics*, vol. 10, no. 3, pp. 180–183, 2016.

[72] M. Hafezi and P. Rabl, "Optomechanically induced non-reciprocity in microring resonators," *Opt. Express*, vol. 20, no. 7, p. 7672, Mar. 2012.

[73] M. Hafezi, E. Demler, M. Lukin, and J. Taylor, "Robust optical delay lines via topological protection," *Nat. Phys.*, vol. 7, no. 11, p. 9, 2011.

[74] M. L. Cooper *et al.*, "Statistics of light transport in 235-ring silicon coupled-resonator optical waveguides.," *Opt. Express*, vol. 18, no. 25, pp. 26505–26516, 2010.

[75] A. B. Khanikaev, S. H. Mousavi, W.-K. Tse, M. Kargarian, A. H. MacDonald, and G. Shvets, "Photonic topological insulators.," *Nat. Mater.*, vol. 12, no. 3, pp. 233–9, 2013.

[76] M. Stone, *Quantum Hall Effect*. WORLD SCIENTIFIC, 1992.

[77] R. B. Laughlin, "Anomalous Quantum Hall Effect: An Incompressible Quantum Fluid with Fractionally Charged Excitations," *Phys. Rev. Lett.*, vol. 50, no. 18, pp. 1395–1398, May 1983.

[78] T. Ikeda and T. Ube, "Photomobile polymer materials: From nano to macro," *Mater. Today*, vol. 14, no. 10, pp. 480–487, 2011.

[79] K. Urayama, "Electro-Opto-Mechanical Effects in Swollen Nematic Elastomers," Springer, Berlin, Heidelberg, 2010, pp. 119–145.

[80] L. T. de Haan *et al.*, "Accordion-like Actuators of Multiple 3D Patterned Liquid Crystal Polymer Films," *Adv. Funct. Mater.*, vol. 24, no. 9, pp. 1251–1258, Mar. 2014.

[81] N. Herzer *et al.*, "Printable Optical Sensors Based on H-Bonded Supramolecular Cholesteric Liquid Crystal Networks," *J. Am. Chem. Soc.*, vol. 134, no. 18, pp. 7608–7611, May 2012.

[82] P. Beyer, E. M. Terentjev, and R. Zentel, "Monodomain Liquid Crystal Main Chain Elastomers by Photocrosslinking," *Macromol. Rapid Commun.*, vol. 28, no. 14, pp. 1485–1490, Jul. 2007.

[83] S. V. Ahir, A. R. Tajbakhsh, and E. M. Terentjev, "Self-Assembled Shape-Memory Fibers

of Triblock Liquid-Crystal Polymers," *Adv. Funct. Mater.*, vol. 16, no. 4, pp. 556–560, Mar. 2006.

[84] H. Zeng, "Light Driven Microscopic Robot XXVII Cycle Light Driven Microscopic Robot," 2015.

[85] T. Okamoto, K. Urayama, and T. Takigawa, "Large electromechanical effect of isotropic-genesis polydomain nematic elastomers," *Soft Matter*, vol. 7, no. 22, p. 10585, Nov. 2011.

[86] Y. Hong *et al.*, "Micron-sized main-chain liquid crystalline elastomer actuators with ultralarge amplitude contractions," *J. Am. Chem. Soc.*, vol. 131, no. 41, pp. 15000–15004, Oct. 2009.

[87] J. Küupfer and H. Finkelmann, "Liquid crystal elastomers: Influence of the orientational distribution of the crosslinks on the phase behaviour and reorientation processes," *Macromol. Chem. Phys.*, vol. 195, no. 4, pp. 1353–1367, Apr. 1994.

[88] K. M. Lee *et al.*, "Photodriven, Flexural-Torsional Oscillation of Glassy Azobenzene Liquid Crystal Polymer Networks," *Adv. Funct. Mater.*, vol. 21, no. 15, pp. 2913–2918, Aug. 2011.

[89] T. Ikeda, J. Mamiya, and Y. Yu, "Photomechanics of Liquid-Crystalline Elastomers and Other Polymers," *Angew. Chemie Int. Ed.*, vol. 46, no. 4, pp. 506–528, Jan. 2007.

[90] K. Kumar *et al.*, "A chaotic self-oscillating sunlight-driven polymer actuator," *Nat. Commun.*, vol. 7, p. 11975, Jul. 2016.

[91] S. Palagi *et al.*, "Structured light enables biomimetic swimming and versatile locomotion of photoresponsive soft microrobots," *Nat. Mater.*, vol. 15, no. February, pp. 1–8, 2016.

[92] H. Zeng, O. M. Wani, P. Wasylczyk, and A. Priimagi, "Light-Driven, Caterpillar-Inspired Miniature Inching Robot," *Macromol. Rapid Commun.*, p. 1700224, May 2017.

[93] M. Rogóż, H. Zeng, C. Xuan, D. S. Wiersma, and P. Wasylczyk, "Light-Driven Soft Robot Mimics Caterpillar Locomotion in Natural Scale," *Adv. Opt. Mater.*, vol. 4, no. 11, pp. 1689–1694, Nov. 2016.

[94] H. Zeng, O. M. Wani, P. Wasylczyk, R. Kaczmarek, and A. Priimagi, "Self-Regulating Iris Based on Light-Actuated Liquid Crystal Elastomer," *Adv. Mater.*, vol. 29, no. 30, p.

1701814, Aug. 2017.

[95] D. Martella *et al.*, "Liquid Crystalline Networks toward Regenerative Medicine and Tissue Repair," *Small*, p. 1702677, Oct. 2017.

[96] H. Zeng *et al.*, "Liquid-Crystalline Elastomers: High-Resolution 3D Direct Laser Writing for Liquid-Crystalline Elastomer Microstructures (Adv. Mater. 15/2014)," *Adv. Mater.*, vol. 26, no. 15, pp. 2285–2285, Apr. 2014.

[97] H. M. D. Bandara and S. C. Burdette, "Photoisomerization in different classes of azobenzene," *Chem. Soc. Rev.*, vol. 41, no. 5, pp. 1809–1825, Feb. 2012.

[98] *,† Kenneth D. Harris, † Cees W. M. Bastiaansen, ‡ and Johan Lub, and ‡ Dirk J. Broer†, "Self-Assembled Polymer Films for Controlled Agent-Driven Motion," 2005.

[99] M. E. McConney *et al.*, "Topography from Topology: Photoinduced Surface Features Generated in Liquid Crystal Polymer Networks," *Adv. Mater.*, vol. 25, no. 41, pp. 5880–5885, Nov. 2013.

[100] D. Rus and M. T. Tolley, "Design, fabrication and control of soft robots," *Nature*, vol. 521, no. 7553, pp. 467–475, May 2015.

[101] T. Xu, W. Gao, L.-P. Xu, X. Zhang, and S. Wang, "Fuel-Free Synthetic Micro-/Nanomachines," *Adv. Mater.*, vol. 29, no. 9, p. 1603250, Mar. 2017.

[102] E. Diller and M. Sitti, "Three-dimensional programmable assembly by untethered magnetic robotic micro-grippers," *Adv. Funct. Mater.*, vol. 24, no. 28, pp. 4397–4404, 2014.

[103] Y.-W. Lu and C.-J. Kim, "Microhand for biological applications."

[104] G. N. Mol, K. D. Harris, C. W. M. Bastiaansen, and D. J. Broer, "Thermo-Mechanical Responses of Liquid-Crystal Networks with a Splayed Molecular Organization," *Adv. Funct. Mater.*, vol. 15, no. 7, pp. 1155–1159, Jul. 2005.

[105] D. Martella *et al.*, "Light activated non-reciprocal motion in liquid crystalline networks by designed microactuator architecture," *RSC Adv.*, vol. 7, no. 32, pp. 19940–19947, Mar. 2017.

[106] H. K. Tsang *et al.*, "Optical dispersion, two-photon absorption and self-phase modulation

in silicon waveguides at 1.5 μm wavelength," *Appl. Phys. Lett.*, vol. 80, no. 3, pp. 416–418, Jan. 2002.

[107] S. Nocentini, "Tunable polymeric photonic structures," University of Florence, 2016.

[108] J. Liu, G. Xu, F. Liu, I. Kityk, X. Liu, and Z. Zhen, "Recent advances in polymer electro-optic modulators," *RSC Adv.*, vol. 5, no. 21, pp. 15784–15794, Feb. 2015.

[109] K. Oda, N. Takato, H. Toba, and K. Nosu, "A wide-band guided-wave periodic multi/demultiplexer with a ring resonator for optical FDM transmission systems," *J. Light. Technol.*, vol. 6, no. 6, pp. 1016–1023, Jun. 1988.

[110] V. R. Almeida, C. A. Barrios, R. R. Panepucci, and M. Lipson, "All-optical control of light on a silicon chip," *Nature*, vol. 431, no. 7012, pp. 1081–1084, Oct. 2004.

[111] Q. Xu and M. Lipson, "Carrier-induced optical bistability in silicon ring resonators," *Opt. Lett.*, vol. 31, no. 3, p. 341, Feb. 2006.

[112] A. Guarino, G. Poberaj, D. Rezzonico, R. Degl'Innocenti, and P. Günter, "Electro–optically tunable microring resonators in lithium niobate," *Nat. Photonics*, vol. 1, no. 7, pp. 407–410, Jul. 2007.

[113] A. P. Ovvyan, N. Gruhler, S. Ferrari, and W. H. P. Pernice, "Cascaded Mach–Zehnder interferometer tunable filters," *J. Opt.*, vol. 18, no. 6, p. 64011, Jun. 2016.

[114] D. Armani, B. Min, A. Martin, and K. J. Vahala, "Electrical thermo-optic tuning of ultrahigh-Q microtoroid resonators," *Appl. Phys. Lett.*, vol. 85, no. 22, pp. 5439–5441, Nov. 2004.

[115] W. von Klitzing, R. Long, V. S. Ilchenko, J. Hare, and V. Lefèvre-Seguin, "Tunable whispering gallery modes for spectroscopy and CQED experiments," *New J. Phys.*, vol. 3, no. 1, pp. 14–14, Aug. 2001.

[116] B. Maune, R. Lawson, G. Gunn, A. Scherer, and L. Dalton, "Electrically tunable ring resonators incorporating nematic liquid crystals as cladding layers," *Appl. Phys. Lett.*, vol. 83, no. 23, pp. 4689–4691, 2003.

[117] C.-T. Wang *et al.*, "Optical bistability in a silicon nitride microring resonator with azo dye-

doped liquid crystal as cladding material.," *Opt. Express,* vol. 21, no. 9, pp. 10989–10994, 2013.

[118] C.-H. Ho *et al.*, "Controllable light diffraction in woodpile photonic crystals filled with liquid crystal; Controllable light diffraction in woodpile photonic crystals filled with liquid crystal."

[119] T. Siegle *et al.*, "Photonic molecules with a tunable inter-cavity gap," *Light Sci. Appl.*, vol. 6, no. 3, p. e16224, 2016.

[120] T. Siegle, M. Remmel, S. Krämmer, and H. Kalt, "Split-disk micro-lasers: Tunable whispering gallery mode cavities," *APL Photonics*, vol. 2, no. 9, p. 96103, 2017.

[121] A. M. Flatae *et al.*, "Optically controlled elastic microcavities," *Light Sci. Appl.*, vol. 4, no. 4, p. e282, 2015.

[122] D. Krishnan and H. T. Johnson, "Light-induced deformation in a liquid crystal elastomer photonic crystal," *J. Mech. Phys. Solids*, vol. 62, no. 1, pp. 48–56, 2014.

[123] M. Kondo, Y. Yu, and T. Ikeda, "How does the initial alignment of mesogens affect the photoinduced bending behavior of liquid-crystalline elastomers?," *Angew. Chemie - Int. Ed.*, vol. 45, no. 9, pp. 1378–1382, 2006.

[124] Y. Yu, M. Nakano, A. Shishido, T. Shiono, and T. Ikeda, "Effect of Cross-linking Density on Photoinduced Bending Behavior of Oriented Liquid-Crystalline Network Films Containing Azobenzene," *Chem. Mater.*, vol. 16, no. 9, pp. 1637–1643, 2004.

[125] M. Yamada *et al.*, "Photomobile polymer materials: Towards light-driven plastic motors," *Angew. Chemie - Int. Ed.*, vol. 47, no. 27, pp. 4986–4988, 2008.

[126] H. Zeng, P. Wasylczyk, G. Cerretti, D. Martella, C. Parmeggiani, and D. S. Wiersma, "Alignment engineering in liquid crystalline elastomers: Free-form microstructures with multiple functionalities," *Appl. Phys. Lett.*, vol. 106, no. 11, 2015.

[127] C. Grivas and M. Pollnau, "Organic solid-state integrated amplifiers and lasers," *Laser Photon. Rev.*, vol. 6, no. 4, pp. 419–462, Jul. 2012.

[128] A. Kurian, N. A. George, B. Paul, V. P. N. Nampoori, and C. P. G. Vallabhan, "Studies on

Fluorescence Efficiency and Photodegradation of Rhodamine 6G Doped PMMA Using a Dual Beam Thermal Lens Technique," *Laser Chem.*, vol. 20, no. 4, pp. 99–1, 2002.

[129] M. Li, N. Zhang, K. Wang, J. Li, S. Xiao, and Q. Song, "Inversed Vernier effect based single-mode laser emission in coupled microdisks," *Sci. Rep.*, vol. 5, no. 1, p. 13682, Nov. 2015.